Gate

N
Source

I- CNT

P
Drain

Gate

Special Issue on

CARBON-BASED MATERIALS

SOCIETY FOR MATERIALS CHEMISTRY

Society for Materials Chemistry

Society for Materials Chemistry was mooted in 2007 with following aims and objectives:

(a) to help the advancement, dissemination and application of the knowledge in the field of materials chemistry,

(b) to promote active interaction among all material scientists, bodies, institutions and industries interested in achieving the advancement, dissemination and application of the knowledge of materials chemistry,

(c) to disseminate information in the field of materials chemistry by publication of bulletins, reports, newsletters, journals.

(d) to provide a common platform to young researchers and active scientists by arranging seminars, lectures, workshops, conferences on current research topics in the area of materials chemistry,

(e) to provide financial and other assistance to needy deserving researchers for participation to present their work in symposia, conference, etc.

(f) to provide an incentive by way of cash awards to researchers for best thesis, best paper published in journal/national/international conferences for the advancement of materials chemistry,

(g) to undertake and execute all other acts as mentioned in the constitution of SMC.

Executive Committee

President
Dr. V. K. Jain
UM-DAE Centre for Excellence in Basic Sciences, University of Mumbai,
Kalina Campus, Mumbai-400098
jainvk@cbs.ac.in

Vice-Presidents
Dr. A. K. Tyagi
Bhabha Atomic Research Centre
Trombay, Mumbai, 400 085
aktyagi@barc.gov.in

Prof. G. Mugesh
Indian Institute of Science
Bangalore - 560 012
mugesh@iisc.ac.in

Secretary
Dr. R. K. Vatsa
Bhabha Atomic Research Centre
Trombay, Mumbai, 400 085
rkvatsa@barc.gov.in

Treasurer
Shri R. K. Mishra
Bhabha Atomic Research Centre
Trombay, Mumbai, 400 085
rkmishra@barc.gov.in

Members
Dr. Neeraj Agarwal
UM-DAE Centre for Excellence in Basic Sciences, University of Mumbai,
Kalina Campus, Mumbai-400098

Dr. (Smt.) Aparna A. Banerjee
Bhabha Atomic Research Centre
Trombay, Mumbai-400085

Dr. (Smt.) Vinita Grover Gupta
Bhabha Atomic Research Centre
Trombay, Mumbai-400085

Dr. Rajesh Ganesan
Indira Gandhi Centre for Atomic Research
Kalpakkam-603102

Dr. P.A. Hassan
Bhabha Atomic Research Centre
Trombay, Mumbai-400085

Dr. (Smt.) Daisy Joseph
Bhabha Atomic Research Centre
Trombay, Mumbai-400085

Dr. S. Kannan
Bhabha Atomic Research Centre
Trombay, Mumbai-400085

Shri. R. Manimaran
Bhabha Atomic Research Centre
Trombay, Mumbai-400085

Dr. Ranjan Mittal
Bhabha Atomic Research Centre
Trombay, Mumbai-400085

Dr. SandeepNigam
Bhabha Atomic Research Centre
Trombay, Mumbai, 400 085

Prof. Sri Sivakumar
Indian Institute of Technology
Kanpur, 208016

Dr. Deepak Tyagi
Bhabha Atomic Research Centre
Trombay, Mumbai-400085

Co-opted Members
Prof. S. Basu
CSIR-Institute of Minerals and Materials Technology,Bhubaneswar-751013

Prof. Lalita Ledwani
Department of Chemistry
Manipal University Jaipur
Jaipur-303007

Dr. K. I. Priyadarsini
Bhabha Atomic Research Centre
Trombay, Mumbai, 400 085

Dr. V. Sudarsan
Bhabha Atomic Research Centre
Trombay, Mumbai-400085

Dr.A. K. Tripathi
Bhabha Atomic Research Centre
Trombay, Mumbai-400085

Special Issue on

Carbon-Based Materials
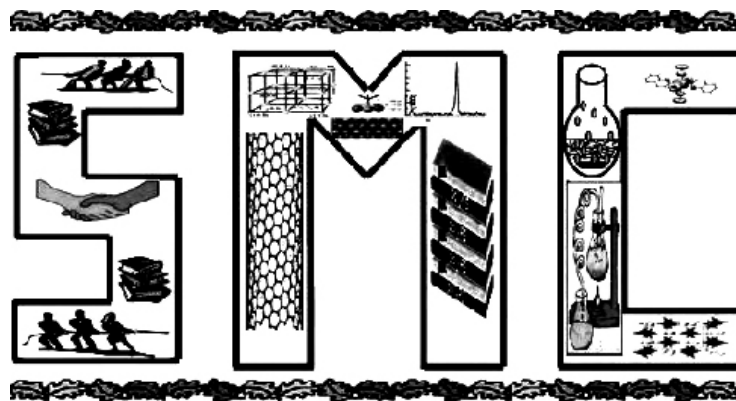
SOCIETY FOR MATERIALS CHEMISTRY

SMC Bulletin

Guest Editor

Dr. Padmnabh Rai
School of Physical Sciences
UM-DAE Centre for Excellence in Basic Sciences
University of Mumbai, Kalina Campus
Santacruz (E), Mumbai-400098
e-mail: padmnabh.rai@cbs.ac.in

Please note that the authors of the paper are alone responsible for the technical contents of papers and references cited therein.
Front cover shows microscopic images of a nitrogen implanted diamond (top left) and a graphene-nanodiamond hybrid films (top middle and right)
along with a schematic of a coaxial gated CNTFET device structure with doped source and drain extension (bottom).

Guest Editorial

Dr. Padmnabh Rai

The allotropes of carbon exist in form of graphite (sp2), carbon nanotube (sp2), graphene (sp2), fullerene (sp2) and diamond (sp3). The current issue is focussed on advanced development in carbon-based materials for their potential applications in green energy, photonics and quantum technologies. Researcher from India and abroad were invited to contribute their article on thematic topic.

The current issue of bulletin includes research and development work on carbon nanotube, graphene and diamond. An energy storage application of carbon nanomaterials is discussed for next generation technology. Growth mechanism of vertically aligned graphene-nanodiamond is discussed. Nanocrystalline diamond shows better electron field emission when implanted with nitrogen ion. Simulation of electroluminescent short-channel carbon nanotube field effect transistor is presented.

It has been my great pleasure to act as a guest editor for special issue on "Carbon-based Materials. My sincere thanks to Prof. V. K. Jain, President, SMC and all the office bearers of executive committee and editorial board of SMC bulletin for giving me the opportunity. I also thank all the authors for their contribution of the current issue of SMC bulletin.

I wish that the articles of the current issue attract broad audience and the readers will find it useful and informative.

From the desks of the President and Secretary

Dr. V. K. Jain
President

Dr. R. K. Vatsa
Hon. Secretary

Dear colleagues,

Warm greetings from Executive Council of Society for Materials Chemistry (SMC).

The Editorial Board of SMC Bulletin is making consistent efforts to bring out special issues on cutting edge research on contemporary subjects. The current issue presents some aspects of R & D work on "Carbon-Based Materials" pursued by different research groups in India and abroad.

The topics covered in this thematic issue include work on energy storage, display application and simulation studies in carbon nanotube, graphene and diamond. A supercapacitance application of carbon nanotube is reviewed by the group from Rice University.There is an enhanced focus on using CNT forests and arrays for flexible and micro-supercapacitors for possible use in cell phones and sensors. Storing hydrogen in solid state materials is a challenge for green energy technology. Metal nanoparticle decorated carbon materials is showing satisfactory result for storing hydrogen. Non-catalytic direct growth of few layered vertical graphene-nano-diamond hybrid structure has been demonstrated by thermally activated hot filament chemical vapor deposition. Nitrogen ion implanted nano-crystalline diamond is showing enhanced electron field emission properties. Electroluminescent property of short-channel (~20 nm) single-walled carbon nanotube field effect transistor is demonstrated by simulation using non-equilibrium Green's function method (NEGF).

We place on record our sincere appreciation to Dr. Padmnabh Rai, Guest Editor, who has taken efforts and an interest to bring out this special issue on 'Carbon-based Materials" in a timely manner. We also thank all the members of SMC for their continued support and cooperation in the growth of the Society.

(Dr. V.K. Jain)
President, SMC

(Dr. R.K. Vatsa)
Hon. Secretary, SMC

CONTENTS

Recent developments of CNT based supercapacitors

Sivaram Arepalli

Department of Materials Science and NanoEngineering, Rice University, 6100 Main Street, Houston, TX 77005
E-mail: Sivaram.arepalli@gmail.com

Abstract

Supercapacitors play an important role in meeting the energy storage requirements for portable as well as rigid energy storage media. Carbon has been an integral part of the conventional electrodes and carbon nanostructures provided enhanced surface area and porosity enabling higher capacities and lifetimes. Over the last decade, considerable research has been done using single wall and multi wall carbon nanotubes for supercapacitor applications. Recent work reported capacitances of the order of 2000 Farads and more than a million cycles using symmetric as well as asymmetric design structures. There is an enhanced focus on using CNT forests and arrays for flexible and micro supercapacitors for possible use in cell phones and sensors. This review will provide the status and future of the CNT based supercapacitors.

Keywords: Carbon nanotube, supercapacitor, energy density, power density, green energy

1. Introduction to energy

In 2004, Nobel Laureate Rick Smalley [1] talked about Terawatt Challenge and stated, "Energy is the number one priority to solve global problems, including clean water and poverty". The ever-increasing demand for energy across the globe has prompted considerable research in the last few decades to improve energy production, storage and transmission. Realizing the continual depletion of fossil fuel energy sources and the detrimental impacts of these sources to the environment focus has been shifted to renewable energy sources such as solar and wind energy in the last two to three decades. Tremendous progress has been achieved in increasing the efficiency, cost effectiveness and reliability of solar energy conversion via solar cells and solar thermal processes. Harnessing wind energy and wave energy is becoming cost competitive to the fossil fuels thereby reducing the dependence on these environmentally harmful sources. These alternative energy sources are renewable and can be sustainable over a long period of time with minimal impact to the environment. Work is in progress to increase the amount of renewable energy compared to the fossil fuel sources. The Figures 1 and 2 depict the current energy consumption in US [2] in 2018 and projected global energy consumption by 2050. The global energy consumption is expected to increase by 50% (600 to 900 Quadrillion BTUs) and the renewals in 2050 will almost double compared to 2018. One Quadrillion BTU aka Quad is equal to 1×10^{18} joules and about 293 terawatt-hours or 33 gigawatt-years. According to US Energy Information Administration (EIA), in 2018, the US electricity generation was 4178 TWh (0.5TW-year) net and 67 TWh (1.6%) from solar. The global energy production

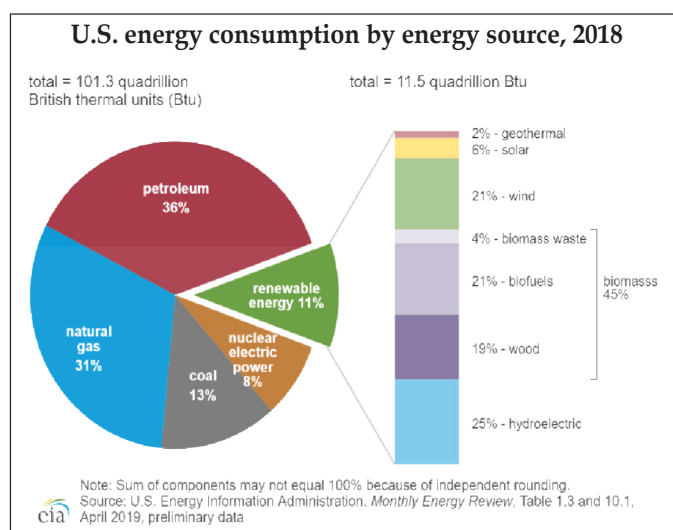in 2018 is about 20 TW-years of which 0.5TWY (2.5%) is from solar (EIA data).

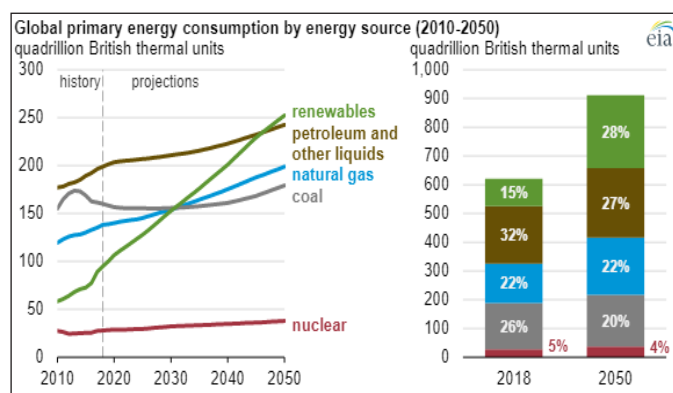**Fig. 1:** *Energy consumption in USA in 2018 (Energy Information Administration [2])*

Fig. 2: *Global energy consumption projected to 2050 (Source: US Energy Information Administration [2])*

According to the ***UN World Energy Outlook Report of 2019,*** "By 2040, low-carbon sources provide more than half of total electricity generation. Wind and solar PV are the star performers, but hydropower (15% of total generation in 2040) and nuclear (8%) retain major shares".

2. Energy storage

The energy from the renewable energy sources such as solar and wind vary with time of the day and the season of the year. It is necessary to store the excess energy during peak energy production cycles and release it during peak demand cycles. A variety of energy storage methods have been used including mechanical (Flywheel, compressed air, pumped hydroelectric, etc.), thermal (Molten salt, ice chest, cryogenic liquids, etc.) and electrochemical (Battery, supercapacitor, fuel cell, etc.). Batteries and supercapacitors have become very common storage media for a majority of portable power devices including cell phones, automobiles and aeroplanes. Normally, batteries provide high energy density (200 Wh/kg) whereas supercapacitors provide high power density (10,000 W/kg) and with quick recycling capability. Elon Musk [3] stated at the Cleantech Forum 2011 in San Francisco about the future of electric vehicles "If I were to make a prediction, I'd think there's a good chance that it is not batteries, but super-capacitors."

3. Supercapacitor

The supercapacitor, also known as ultracapacitor has orders of magnitude larger capacitance (order of several Farads) than a regular capacitor which normally has capacitances of several microfarads. Capacitor stores energy by means of a static charge stored in a medium between two electrodes and its capacitance increases with area and is inversely proportional to distance between the charged electrodes. When an ion conducting electrolyte is used with a porous insulating separator material between

Fig. 3: *The Gouy-Chapman-Stern model of Supercapacitor [5].*

electrodes, it is noted that each electrode develops a Helmholtz layer of opposing charge within a few microns thereby forming a capacitor at each electrode [4]. The thickness of this Helmholtz layer is defined as Electric Double Layer and depends on the surface porosity of the electrodes (normally made of carbon) as well as the size of solvated ions of the electrolyte. The distance between the opposing charges (dictated by the electrode /electrolyte interface) falls to less than a micron (Fig. 3) and thereby providing large capacitance at each electrode [5].

The supercapacitor (Electric Double Layer Capacitor) is therefore in principle a combination of two very thin capacitors and can only operate at low voltages (2 or 3V) but has capacitance values of the order of tens of Farads. Also, the supercaps exhibit very low equivalent series resistance (ESR) enabling them to charge fast (few seconds compared to few hours in case of batteries) and can provide large number of charge-discharge cycles (several million cycles). Inorder to obtain high energy supercapacitors, the adopted strategy should be to increase the capacitance and to increase the operating voltage since the stored energy is proportional to voltage square. The capacitance depends mostly on the electrodes and the energy depends on the electrolyte. Commercial supercapacitors normally use organic electrolytes that can operate at voltages close to 3V compared to aqueous electrolytes at about 2V. Recently, Tomiyasu et al. [6] reported a remarkably high 3.2 V supercapacitor containing a saturated aqueous solution of sodium perchlorate and observed high energy density of 36.3 Wh/kg.

3.1 Pseudo-capacitor

The EDLCs however suffer from low energy density. To rectify these problems, transition metal oxides (RhO_2, MnO_2, TiO_2, …) and transition metal sulphides were tried in the carbon electrodes. It was noted that the electrode - electrolyte interface now undergoes redox reactions enhancing the capacitance 10 to 100 times more than EDLCs. This new type of supercapacitor is called pseudo-capacitor and it behaves like a battery with slow charging rates and limited number of cycles.

3.2 Asymmetric capacitor

A hybrid version of EDLC and pseudocapacitor is an asymmetric capacitor which has EDLC on one electrode (usually carbon coated) and the other with metal oxide coated carbon electrode. Recent studies reported asymmetric capacitors with capacitance of several hundred Farads and with several hundred cycle lifetime for the hybrid supercapacitors. A recent paper by Richard Kaner
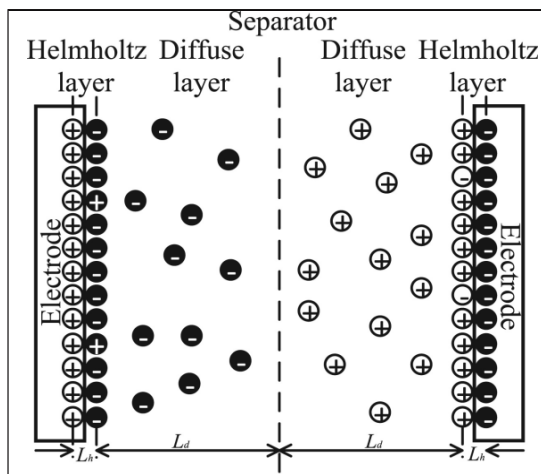
and co-workers [7] provided a review of asymmetric supercapacitors and their version of Ragone's plot (Fig. 4) compares the different electrochemical energy storage

Fig. 4: *Ragone plot illustrating the performances of specific power vs specific energy for different electrical energy-storage technologies. Times shown in the plot are the discharge time, obtained by dividing the energy density by the power density [7].*

media.

Hybrid capacitors have come to be identified as devices in which one electrode stores charge by a battery-type Faradaic process while the other electrode stores charge based on a capacitive mechanism. A general classification of supercapacitors is shown in Fig. 5.

4. Carbon nanotubes

Carbon nanotubes are 1-D nanostructures of carbon and have diameters of the order of a nm and lengths are normally in the range of microns there by becoming ideal structures for large aspect ratio materials. The carbon nanotube (CNT) can be visualized as a graphene sheet rolled into a tube forming single wall (SWCNT) or multiwall carbon nanotube, MWCNT (coaxial tube with different layers) and Fig. 6 shows images [8] of different CNTs. The discovery of CNTs can be attributed to three researchers Endo, Bethune and Iijima even though larger carbon filaments have been reported earlier. The reader is referred to an editorial [9] in the journal "Carbon" for more details about discussion about who discovered CNTs.
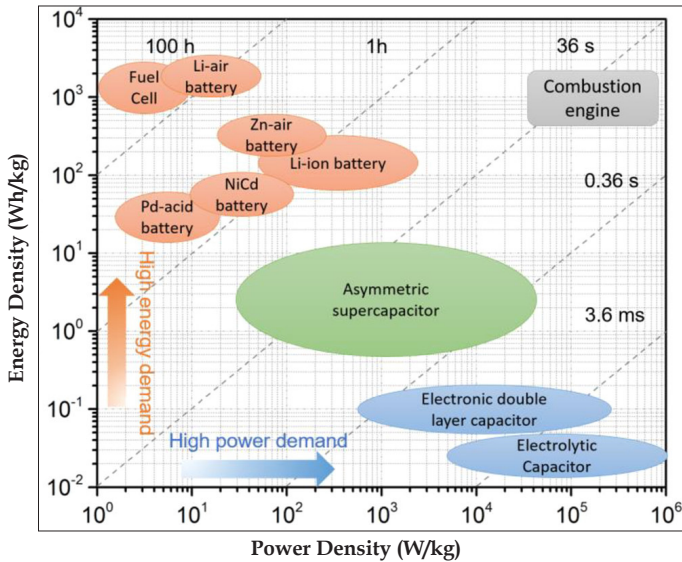
The twist of the graphene sheet while it is being rolled into CNTs dictates the chirality of the CNTs resulting semiconducting and metallic nanotubes. Normally, the synthesized CNTs contain a variety of these semiconducting and metallic CNTs in a statistical ratio of 2:1 and form bundles because of strong van der Walls interactions between individual tubes. There are a vast number of papers and books about the identifying the chirality, de-bundling and separating the individual CNTs by tube type (Semiconducting or metallic). Recent research was focused on growing CNTs of specific chirality for applications such as nanosensors. The reader is referred to a recent report from a biennial conference on CNT nucleation and growth [10] for the status of these issues. In addition, this conference series has identified the appropriate development trend for SWCNT growth for a variety of applications (Fig. 7).

The CNTs have unique mechanical, thermal, electrical and optical properties in addition to morphology giving rise to large surface area (hundreds of cm^2/g) and nanometer size porosity. The following table provides a
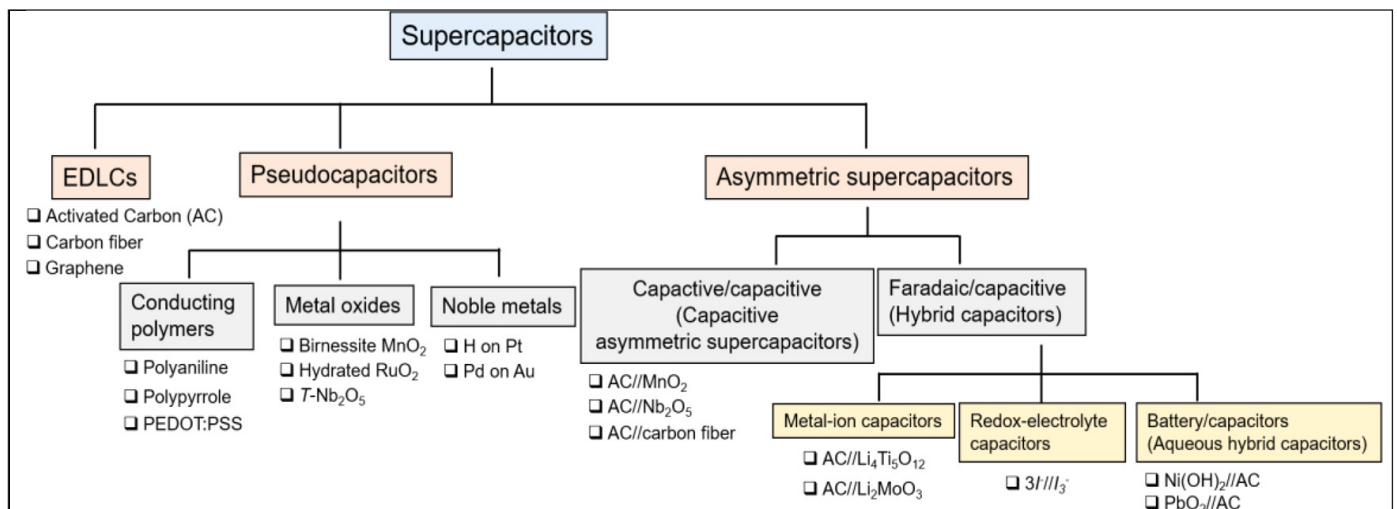

Fig. 5: *Classification of supercapacitors and possible electrode materials [7].*
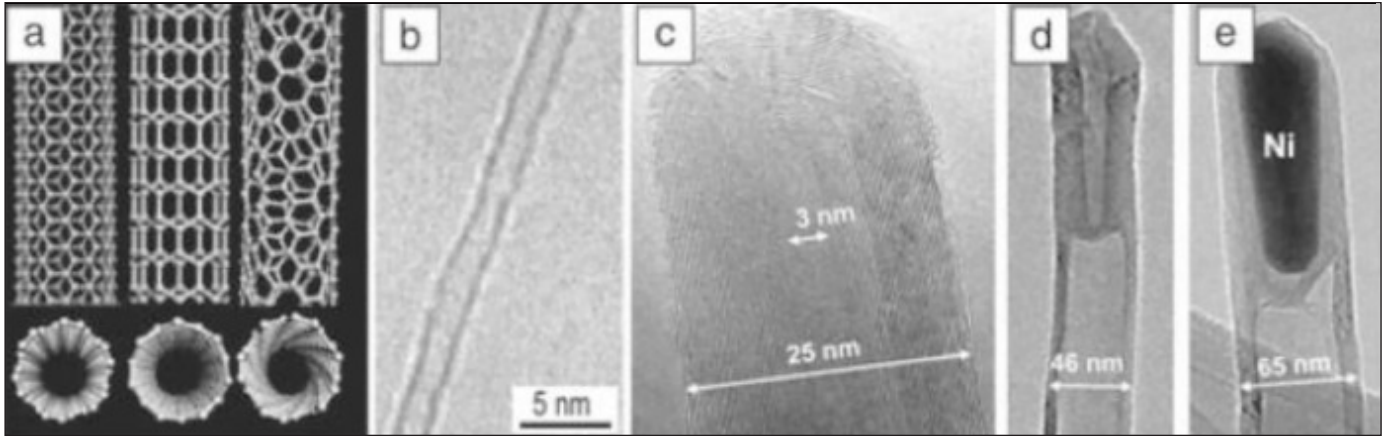
Fig. 6: *A family of CNTs: (a) schematics of armchair, zigzag, and chiral SWCNTs (from left to right); (b) SWCNT; (c-d) MWCNT with no catalyst; and (e) MWCNT with a catalyst particle [8].*
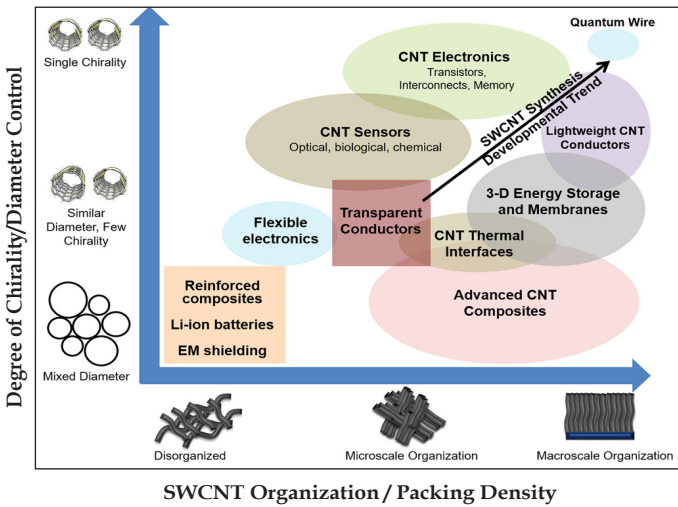

Fig. 7: *Structure−property relationship diagram showing the application space of SWCNTs with respect to tube diameter/helicity and architecture. The horizontal axis shows the organization of the SWCNTs from a random network to highly aligned architectures (vertically aligned, fibers, etc.), while the vertical axis shows the degree of diameter/helicity control from mixed to single helicity. Existing and emerging SWCNT applications are shown in the square and oval boxes, respectively. The diagonal arrow in the graph shows the general direction of developments in synthesis over time [10].*

partial list of these properties [11] for SWCNTs. The values for MWCNTs will be off by a factor of 2 or more.

There is a vast amount of research carried out over the last three decades on these properties and a concentrated effort in the synthesis, purification and processing of CNTs for a variety of applications ranging from aerospace, automobile, electronics to medicine [12]. For some applications it is necessary to have individual SWCNTs of specific tube type (semiconducting or metallic) and chirality. However, for energy storage applications in batteries and supercaps, the requirements are not so stringent, and the CNT material should have large surface area and porosity as well as high electrical conductivity. Majority of energy storage studies were done using bundles of SWCNTs and MWCNTs. Recent research focused on using vertically aligned CNTs (VACNTs) aka CNT forests as 2D mats and 3D structures for energy storage.

5. CNT applications in supercapacitors

During the early years, the advancement of supercapacitors (SCs) was made possible by the porosity and large surface area of activated carbon. The control of porosity in SCs provides specific capacity of ion

Table 1 The major properties of CNTs [11]

S. No.	Property	Computational calculations	Experimental measurements
1	Young's modulus [TPa]	1.5 to 5.0	2.8 to 3.6
2	Tensile strength [GPa]	300	150
3	Electrical conductivity [S/m]	1×10^7	6.6×10^3
4	Thermal conductivity [W/m K]	80–9500	3500
5	Charge mobility [cm^2/V-s]	1.2×10^5	1×10^3
6	Thermal stability in air [°C]	750	420
7	Surface area [m^2/g]	50–1315	619.1

adsorption and the diffusion of ions in and out of the pores during the charge/discharge processes. The discovery and availability of CNTs with much better thermal and electrical conductivities in addition to mechanical strength helped enhancements of capacitance as well as energy density. A recent review [11] provides valuable information on the applications of CNTs in supercapacitors. The table 2 summarizes some of the results.

Table 2 Performance of different bare CNT-based supercapacitors [11]

S. No.	Electrode	Specific capacitance (F/g)	Energy density (Wh/kg)	Power density (kW/kg)
1	SWCNT film	180	7	20
2	Nitric acid treated MWCNTs	102	0.5	–
3	Rolled SWCNT film	35	43.7	197.3
4	Stacked SWCNT array	20–160	17.5–94	43–210
5	Stacked MWCNT array	11–22	2.3–5.4	19.6–35.4

The first comprehensive study [13] of space charge distributions in EDLCs based on polarizable nanoporous electrodes, containing carbon nanotubes (CNTs) as electrode material was done in 2007. It was noted that CNTs help to increase wettability of the normal carbon electrodes resulting in 50% enhancement of capacitance. It has been a great challenge to increase SC's energy density without compromising its power density.

5.1 Combining CNTs with other nanomaterials

It is noted that pure CNTs did provide a large enhancement of the SC performance compared to regular carbon based SCs. Additional improvements are possible by adding other nanomaterials (NMs) such as graphene, graphite oxide, carbon nano-cones, carbon nano-onions and carbon sponge. A recent review [14] focuses on how to improve the performance of SCs by using a combination of materials with CNTs. One scenario will use CNTs utilized as the scaffolds and metal oxides are deposited in situ. Another scenario suggests using nanocomposites (Fig. 5) with CNTs and conducting materials including polymers such as polyaniline (PANI). Chen and co-workers reported [15] a study of comparing disordered CNTs and vertically aligned CNTs (VACNTs) for SCs. They studied high-performance supercapacitor based on polyaniline/vertical-aligned carbon nanotubes (PANI/VA-CNTs) nanocomposite electrodes where the vertical-aligned-structure is formed by the electrochemical-induction (0.75 V). The supercapacitor displayed large specific capacitance of 403.3 F/g, which is 6 times higher than disordered CNTs in $HClO_4$ electrolyte. Additionally, the supercapacitor can also present high specific capacitance (314.6 F/g), excellent cycling stability (90.2% retention after 3000 cycles at 4 A/g) and high energy density (98.1 Wh/kg) in $EMIBF_4$ organic electrolyte. They claimed that the key to high-performance lies in the vertical-aligned-structure
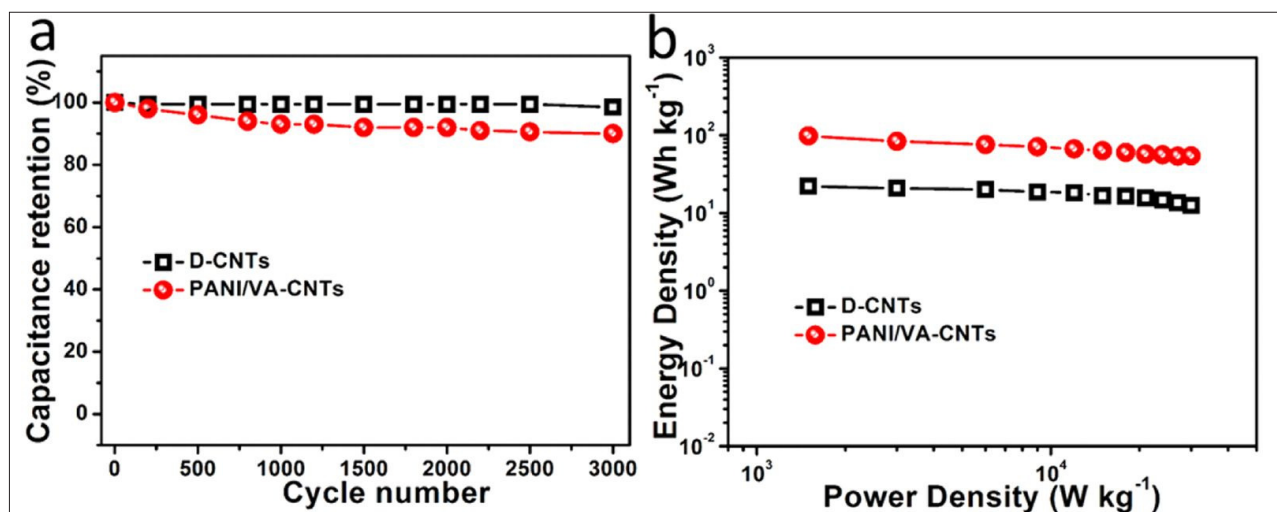

Fig. 8: *(a) Cycle testing of supercapacitors under a voltage of 3 V at a current density of 4 A g−1. (b) Energy density versus power density of supercapacitors [15].*

providing for faster ion diffusion and high electrochemical capacitance of polyaniline for better ion accommodation.

It was concluded that composite materials can improve the performance of supercapacitor electrodes much better than a single material ever could. It is also possible to design 3D structures using a combination of materials to provide the needed surface area, accessibility to nano size pores and quick ion adsorption and desorption. One recent study reported using CNT scaffolds, graphene nanosheets and PANI. Jin and co-workers [16] constructed a three-dimension (3D) conductive network by CNTs and graphene nanosheets on the polyester fabric via a "dipping-drying" process and electrophoretic deposition method, which significantly increased the electron transportation rate and reduced the electrolyte ion diffusion path. The resulting composite fabric provided a promising substrate for flexible supercapacitor's textile-based electrode preparation.

In 2018, Zhou et. al. [17] reported a 3D structure with the addition of graphitic nanofibers (GNFs) to CNTs to improve the SC performance. The CNT/GNF-based symmetric device showed a maximum specific energy of 72.2 Wh/kg at a power density of 686.0 W/kg. The supercapacitor showed a very good cycling stability of 96% after 10 000 charge/discharge cycles. According to them, "the GNFs have open edges and large interlayer spacing which will ensure ion transportation at high rates and plays

the role of an ion reservoir, while the incorporated CNTs are believed to provide greater area for the ions to adhere to and fast channels for charge transport". The performance enhancement is shown in Fig. 9.

Zhang and co-workers [18] developed an asymmetric supercapacitor (ASC) with 3D cobalt sulfide encapsulated carbon nanotube/carbon nanofiber (Co_9S_8@CNT/CNF) composite, which showed a capacitance of ~1580 F/g at a current density of 1 A/g. They report a maximum energy density of 58 Wh/kg at a power density of 1000W/kg and even after 10,000 cycles, the ASC still retains 93% of the initial capacitance at a current density of 5 A/g. They claim that the aligned CNT/CNF nanochannels increase the ion transfer speed and shorten the ion transfer distance, thereby boosting both power density and energy density.

5.2 CNTs for flexible supercapacitor

A recent review on CNT based fibers for energy storage focuses on the possibility of flexible and wearable energy storage [19]. The flexible energy storage devices assembled from carbon nanotube fiber-based electrodes has the advantages of being bendable, lightweight, and invisible encapsulation, which will be the foundation of the wearable smart textiles and promotes the rapid development of flexible energy storage devices.

The relatively low specific capacitance and yield have been the most drawbacks of carbon nanotube
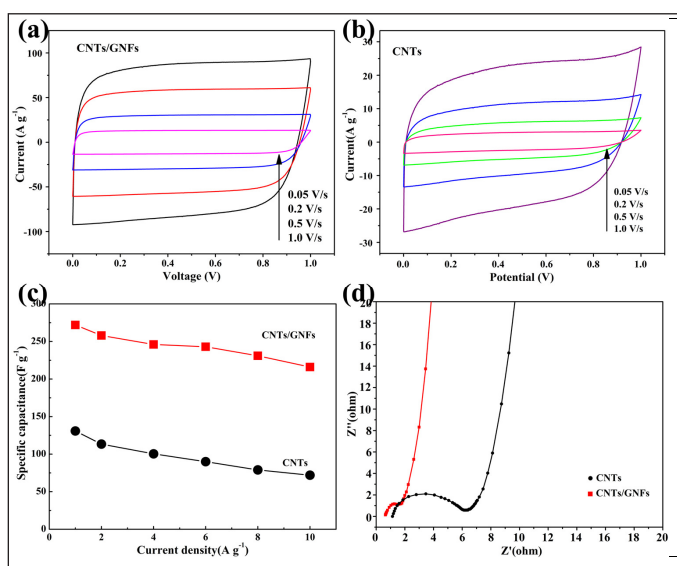
Fig. 9: *Electrochemical properties of the CNTs/GNFs- and CNTs-based supercapacitors in 6 mol/L KOH electrolyte. CV curves of (a) CNT/GNFs and (b) CNTs under various scan rates. (c) The specific capacitance of CNTs/GNFs and CNTs calculated at various current densities. (d) EIS measurements of CNTs/GNFs and CNTs based EDL supercapacitors [17].*
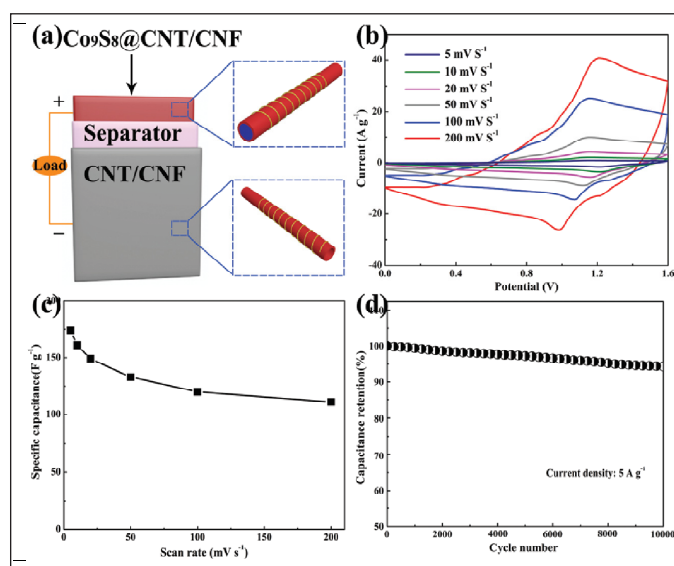
Fig. 10: *Electrochemical characterizations of the Co_9S_8@CNT/CNF// CNT/CNF ASC. (a) Schematic illustration of the ASC device. (b) CV curves of the ASC at various scan rates from 5 to 200 mV/s measured between 0 and 1.6 V. (c) Plot of the specific capacitance as a function of scan rates. (d) Cycling performance of the ASC device at a current density of 5 A/g [18].*
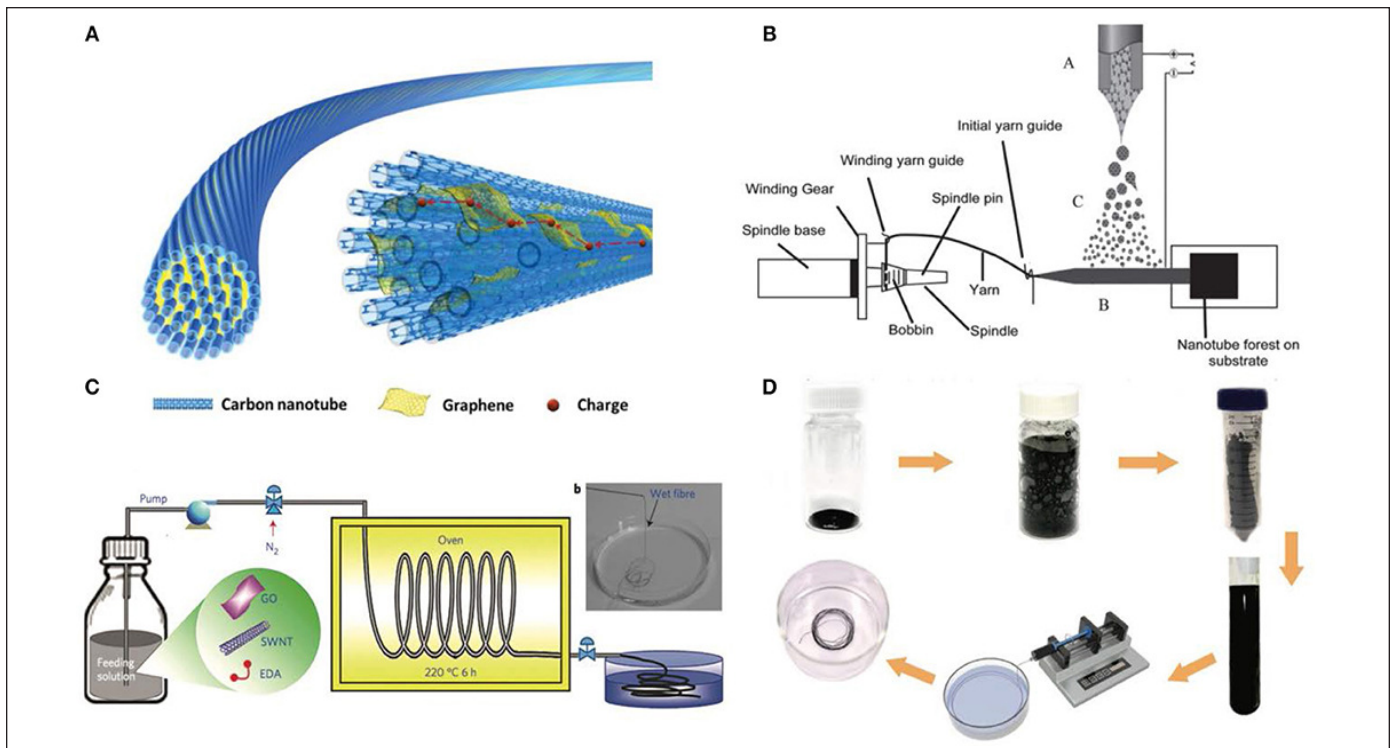
Fig. 11: Schematic illustration of (a) solid-spun carbon nanotube fiber with internal graphene sheets, (b) Co-spinning of CNT/graphene hybrid fiber with solid-spun and electro spinning methods, (c) Hydrothermal procedures of rGO/SWCNT composite fiber, (d) Super-acid exfoliated graphene sheets co-spun with CNTs [19].
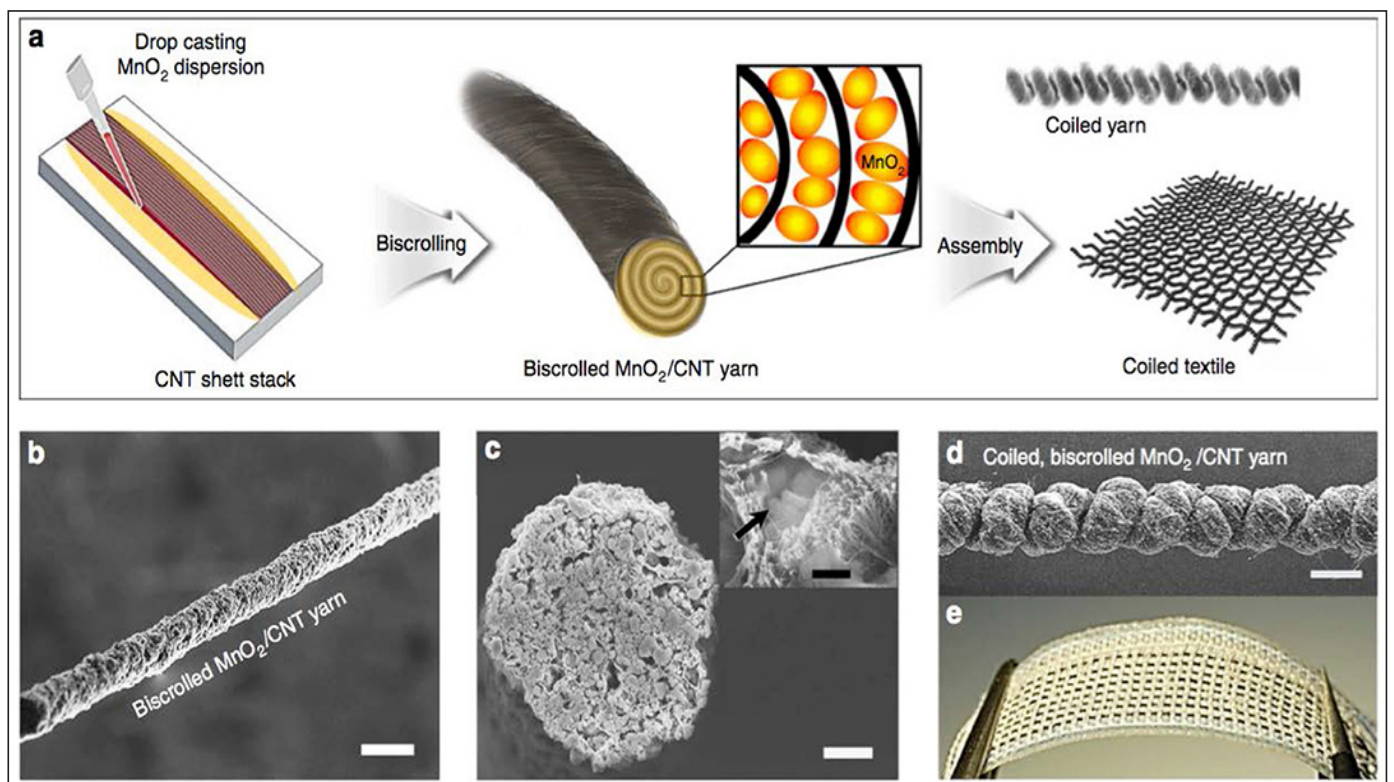
Fig. 12: *Schematic showing (a) Preparation and structure of biscrolled CNT/MnO$_2$ hybrid fiber, SEM morphologies of (b, c) as spun biscrolled hybrid fiber and (d, e) two-ply coiled yarn integrated in a fabric [18].*

based fibers, but it is theoretically possible to overcome these by using appropriate nano-structured materials and improving the fiber fabrication methods. Some of the CNT fiber fabrication methods used to study SCs is shown in Fig. 11.

There were a few articles on co-spinning CNTs with other materials to prepare a fiber based SC. Ray Baughman and co-workers [20] developed a novel method that bi-scrolled CNT sheets with drop casting of MnO_2 dispersion into a fiber (shown in Fig. 12). The strategy of biscrolling can dramatically expand the loading mass of active nanoparticles as high as 99 wt% without any influences on the mechanical properties of fiber. The bi-scrolled MnO_2/CNT fiber was able to achieve an areal specific capacitance of 889 mF/cm^2 (or 155 F/cm^3) and possessed an energy density of 35.8 μWh/cm^2 (or 5.41 mWh/cm^3).

Jeffrey Glass and co-workers [21] reported highly stretchable supercapacitors based on crumpled CNT-forests that are transferred onto pre-strained elastomer substrates. The crumpled CNT has demonstrated superior electrochemical performance under large uniaxial or biaxial strains (Fig. 13). Little variation in CV, charge–discharge, and specific capacitance was observed even when the electrodes are stretched to a uniaxial strain of 300% or biaxial strain of 300% × 300%. Moreover, the electrode performance can be maintained over thousands of stretching–relaxing cycles. The stretchable SCs that are assembled by stacking two crumpled CNT-forest electrodes and separated by a thin layer of PVA–KCl gel as the electrolyte and separator are able
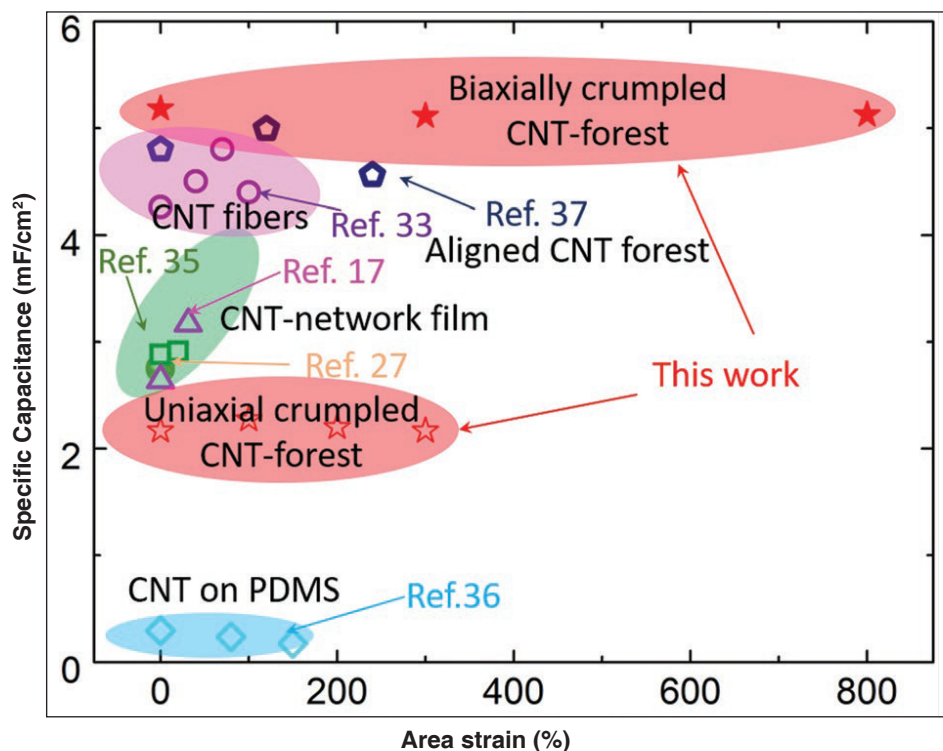
Fig. 13: Performance comparison of the stretchable, all-solid-state, crumpled-CNT-forest supercapacitors with other CNT supercapacitors reported in literature. The capacitances of this work are measured by charge–discharge at a rate of 50 mV s−1 [21].
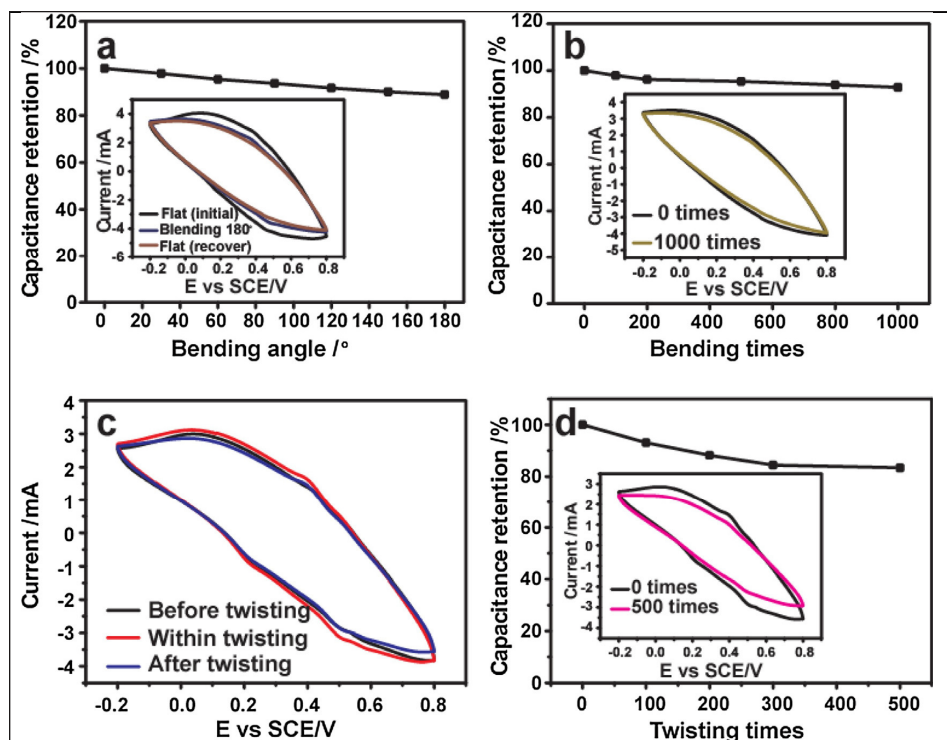
Fig. 14: Capacitance retentions and CV curves of the PANI/CNTs/G/PETC electrode under different (a and its inset) bending angles and (b and its inset) bending times. (c) CV curves of the PANI/CNTs/G/PETC electrode under the twisting condition. (d and its inset) Capacitance retentions and their corresponding CV curves of the PANI/CNTs/G/PETC electrode under various twisting times [16].

to sustain a stretchability of 800% and possess a specific capacitance of 5 mF/cm² (≈1.25 F/cm³) at the scan rate of 50 mV/s. According to the authors, these stretchable supercapacitors can also be modified to hybrid SCs by adding metal oxide nanoparticles.

Another recent article [16] reports the stability of composite electrodes for bending and stretching for hundreds of cycles. The results (Fig. 14) show excellent resiliency and paves the way for future wearable electronic applications.

5.3 Computational work on CNT applications of SCs

Computational work on supercapacitors has a long history. Most of the earlier work focused on EDLC aspects of the supercapacitor. Analytical techniques as well as atomistic computations have been used to provide a theoretical basis for understanding the dependence of capacitance on the electrode and electrolyte. In recent years molecular modelling has contributed greatly to the understanding of charge storage mechanisms and dynamics in EDLCs. Calculations based on "Molecular Dynamics" seemed to provide a better understanding of the SCs. In majority of the cases, the computations did not match the experimental measurements. However, these calculations did provide an overview of the critical role of the morphology as well as reactions of the electrodes with electrolytes.

In 2010, Shim et al. [22] employed the Molecular Dynamics (MD) technique to study the double-layer capacitive effect for electrified CNTs with different diameters, as shown in Fig. 15. The MD simulations indicated that the ions do not flow through the CNT when the diameter of CNT is small (Fig. 16).

Compared with the outer surface, the narrow region of the inner surface leads to the reduction in capacitance with the decrease in radius at sub-nanometer scale. This phenomenon is due to the decreasing accessibility of the inner region for electrolyte ions, leading to the reduction in the number of adsorbed ions and effective active surface area. The obtained curve of capacitance versus diameter is consistent with the experimental results.

In 2013, Younghee Lee [23] and coworkers published a paper on a theoretical model based on transmission line combined with pore size distribution. The model successfully explained how pores length, and pore radius of active materials and electrolyte conductivity can affect capacitance and dynamic performance of different capacitors. The powerfulness of the model was confirmed by comparing with experimental results of a micro-supercapacitor consisted of vertically aligned multiwalled carbon nanotubes (v-MWCNTs), which revealed a linear current increase up to 600 V/s scan rate demonstrating an ultrafast dynamic behavior, superior to randomly entangled single walled carbon nanotube device, which is clearly explained by the theoretical model.

In 2014, Burt et. al. [24] presented the status of molecular modelling of EDLC. They reviewed and compared different computational methods. According to them the Monte Carlo (MC) and molecular dynamics
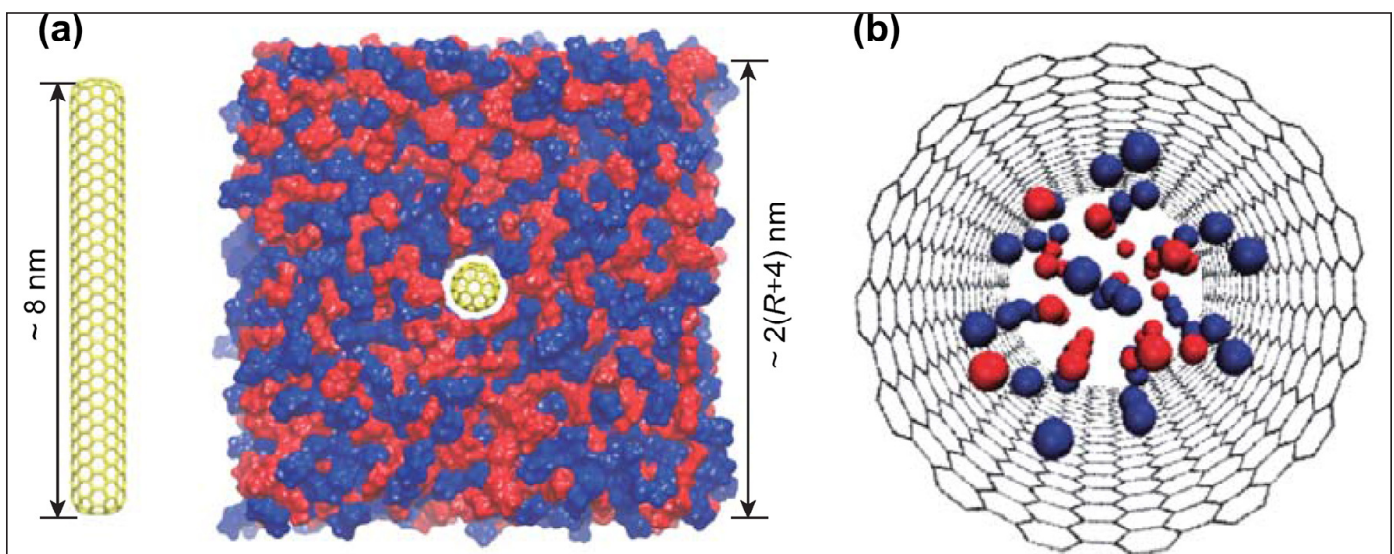

Fig. 15: *Two surfaces of CNTs in CNT anodes of a supercapacitor with a room temperature ionic liquid (RTIL) as electrolyte. (a) The outer surface of CNTs. (b) The inner surface of CNTs. Red and blue dots represent the center-of-mass positions of EMI⁺ and BF4⁻ ions of the RTIL electrolyte, respectively [22].*
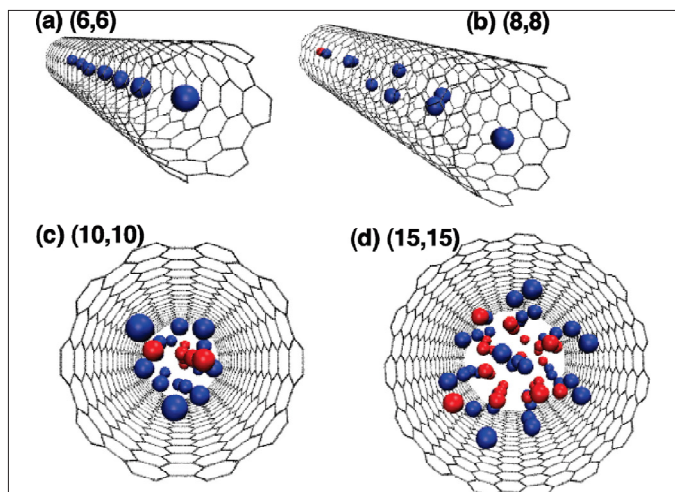
Fig. 16: *Snapshots of internal room temperature ionic liquid (RTIL) ions associated with the radial distributions inside the CNT anodes. Red and blue dots represent the center-of-mass positions of EMI⁺ and BF4⁻ ions, respectively [22].*

(MD) are the two most favored molecular simulation techniques used. They state that the MC simulations are limited to calculating equilibrium properties whereas MD simulations can calculate dynamic properties (such as ionic diffusion) of a molecular system and therefore is more useful for EDLC computations.

In 2018, Bo et. al. [25], reported the design of SC electrodes using MD simulations. According to them, "Molecular dynamics (MD) simulations could provide theoretical guidelines for the optimal design of electrodes and the improvement of capacitive performances, e.g., energy density and power density. The enhancement of power density can be achieved by the intensified ion dynamics and shortened ion pathway. Rational control of the electrode morphology helps improve the ion dynamics by decreasing the ion diffusion pathway. Tuning the surface properties (e.g., the affinity between the electrode and the ions) can affect the ion packing phenomena". The simulations included various aspects of the electrodes (including surface area, porosity and polarizability) and electrolytes (including viscosity and solvated ion sizes). The calculations helped to optimize EDLCs as a whole system and compare new electrode materials as well as electrolyte combinations. The typical features of porous materials enable the long diffusion pathway and relatively low power density. When the dimension of electrode materials becomes close to several nanometers, some exotic electrochemical behaviors emerge for diverse nanomaterials. Their nanoconfined space leads to their complex charging mode with the combination of ion exchange, counterion adsorption and co-ion

desorption.

6 Conclusions

In summary, CNTs have become indispensable in the development of supercapacitors. Most of the earlier research was carried out using SWCNTs and MWCNTs. Using CNT forests in the electrodes helped to improve the accessible surface area, porosity and ion diffusion resulting in enhanced SCs. Combining the CNTs with other nanomaterials such as graphene and metal oxides to form nanocomposites, provided additional capacitance as well as larger energy densities. The CNT forests and fibers helped to advance the upcoming field of wearable energy storage media. On the computational side, the EDLC calculations have progressed considerably during the last decade. However, computations of complex electrode structures, such as three-dimensional hierarchical porous networks are lacking. It becomes more challenging to include the redox reactions of pseudocapacitors. Experimentally, the push is towards achieving increased energy density while maintaining high power density and with high charge-discharge cycles. The role of CNTs in this burgeoning field is unambiguous and it is critical to have reliable inexpensive industrial scale supply of CNTs to meet the 21st century challenges of energy storage.

Acknowledgement:

References

1. R. E. Smalley, MRS Bulletin 3*0 (2005)* 412.

2. https://www.eia.gov/ and https://www.eia.gov/todayinenergy/detail.php?id=41433.

3. Elon Musk, https://techcrunch.com/2011/03/25/elon-musk-says-super-capacitors-not-batteries-will-be-breakthrough-for-evs/ and Clean Tech Summit 2011 - IPO Spotlight with Elon Musk, https://www.youtube.com/watch?v=hTBZGWEzR_E.

4. B. E. Conway, Electrochemical Supercapacitors: Scientific Fundamentals and Technological Applications, (Plenum Publishers, New York; 1999).

5. L. Zhang, X. Hu, Z. Wang, F. Sun and D. G. Dorrell, Renewable and Sustainable Energy Reviews 81 (2018) 1868.

6. H. Tomiyasu, H. Shikata, K. Takao, N. Asanuma, S. Taruta and Y.-Y. Park, Scientific Reports (2017) 4504850.

7. Y. Shao, M. F. El-Kady, J. Sun, Y. Li, Q. Zhang, M. Zhu, H.

Wang, B. Dunn and R. B. Kaner, Chemical Reviews 118 (2018) 9233.

8. Y. Gogotsi, Mater Res Innovations 7 (2003) 192.

9. M. Monthioux and V. L. Kuznetsov, Carbon 44 (2006) 1621.

10. R. Rao, C. L. Pint, A. E. Islam, R. S. Weatherup, S. Hofmann, E. R. Meshot, F. Wu, C. Zhou, N. D. Placidus, B. Amama, J. Carpena-Nuñez, W. Shi, D. L. Plata, E. S. Penev, B. I. Yakobson, P. B. Balbuena, C. Bichara, D. N. Futaba, S. Noda, H. Shin, K. S. Kim, B. Simard, F. Mirri, M. Pasquali, F. Fornasiero, E. I. Kauppinen, M. Arnold, B. A. Cola, P. Nikolaev, S. Arepalli, H. Cheng, D. N. Zakharov, E. A. Stach, J. Zhang, F. Wei, M. Terrones, D. B. Geohegan, B. Maruyama, S. Maruyama, Y. Li, W. Adams and A. J. Hart, ACS Nano 12 (2018) 11756.

11. S. Kumar, M. Nehra, D. Kedia, N. Dilbaghi, K. Tankeshwar and K. Kim, Progress in Energy and Combustion Science 64 (2018) 219.

12. M. Meyyappan, Carbon Nanotubes: Science and Applications, CRC Press (2004); S. Arepalli and P. Moloney, MRS Bulletin 40 (2015) 804; J. Simon, E. Flahaut and M. Golzio, Materials 12 (2019) 624.

13. D. Tashima, K. Kurosawatsu, M. Uota, T. Karashima, M. Otsubo, C. Honda and Y. M. Sung, Thin Solid Films 515 (2017) 4234.

14. Z. Li, K. Xu and Y. Pan, Nanotechnology Review 8 (2019) 35.

15. G. Wu, P. Tan, D. Wang, Z. Li, L. Peng, Y. Hu, C. Wang, W. Zhu, S. Chen and W. Chen, Scientific Reports 7 (2017) 43676.

16. L. Jin, F. Shao, C. Jin, J. Zhang, P. Liu, M. Guo and S. Bian, Electrochemica Acta 249 (2017) 387.

17. Y. Zhou, P. Jin, Y. Zhou and Y. Zhu, Scientific Reports 8 (2018) 9005.

18. Y. Zhou, Y. Zhu, B. Xuc and X. Zhang, Chem. Commun. 55 (2019) 4083.

19. Z. Lu, R. Raad, F. Safaei, J. Xi, Z. Liu and J. Foroughi, Frontiers in Materials 6 (2019) 138.

20. C. Choi, K. M. Kim, K. J. Kim, X. Lepró, G. M. Spinks, R. H. Baughman and S. J. Kim, Nature Communications 7 (2016) 3811.

21. C. Cao, Y. Zhou, S. Ubnoske, J. Zang, Y. Cao, P. Henry, C. B. Parker and J. T. Glass, Advanced Energy Materials 9 (2019) 1900618.

22. Y. Shim and H.J. Kim, ACS Nano 4 (2010) 2345.

23. A. Ghosh, V. T. Le, J. J. Bae and Y. H. Lee, Scientific Reports 3 (2013) 2939.

24. R. Burt, G. Birkett and X. S. Zhao, Phys. Chem. Chem. Phys. 16 (2014) 6519.

25. Z. Bo, C. Li, H. Yang, K. Ostrikov, J. Yan and K. Cen, Nano-Micro Lett. 10 (33) (2018); https://doi.org/10.1007/s40820-018-0188-2.
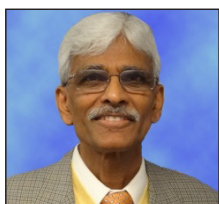
Dr. Arepalli *is with Department of Materials Science and NanoEngineering, Rice University in Houston since 2016. He was the Vice President of Graduate Education at the National Institute of Aerospace, Hampton, VA from 2013 to 15. Prior to that, he was a Professor under the World Class University program in the Department of Energy Science at Sungkyunkwan University (SKKU) in Suwon, South Korea. He was the Chief Scientist of the Applied Nanotechnology Program and Reentry Plasma Diagnostics Program at NASA-Johnson Space Center and worked for 22 years before moving to Korea in 2009. Dr. Arepalli received his Ph.D. in Physics from the Indian Institute of Technology (IIT) Kanpur in 1979. He did postdoctoral work at U Penn and Cornell University. His current interests include synthesis and processing of Nanomaterials (including CNT, BNNT and graphene) for energy applications such as fuel cells, solar cells, batteries and supercapacitors. He also focuses on experimental and computational research for material development for subsonic to hypersonic flows in addition to aerospace structures, environmental sensors and bioimplants.*

Hydrogen storage in carbon nanomaterials

Gopal Sanyal[1] and Brahmananda Chakraborty[2,3*]
[1]Mechanical Metallurgy Divison, [2]High Pressure &Synchroton Radiation Physics Division, Bhabha Atomic Research Centre, Trombay, Mumbai-400085, India
[3]Homi Bhabha National Institute, Mumbai-400085, India
*Corresponding author Email: brahma@barc.gov.in

Abstract

On-board hydrogen (H_2) storage is a quite time-appropriate research topic attracting heavy attention throughout the globe for last a few decades for resorting to greener energy alternatives aiming maximization of specific storage capacity for higher fuel efficiency. Though pure carbon nanomaterials are able to demonstrate moderate H_2 storage capability at low temperature and high-pressure conditions those are not suitable for practical scenario. However, decoration with suitable metal nanoparticles might raise H_2 storage potential of carbon nanomaterials even at ambiance to a great extent, satisfying requirement of Department of Energy (DoE), USA. This review presents the current perspective covering theoretical and experimental studies in that direction.

Keywords: Hydrogen storage, Carbon Nanomaterials, Decorated Carbon Nanomaterials, Binding energy, Release temperature

1. Introduction

Since the last few decades, it became necessary to find suitable substitute to conventional fossil fuels towards a cleaner environment. Among all alternative fuels, hydrogen is a promising energy carrier with zero emission while burnt with oxygen. Usage of hydrogen (H_2), as a fuel, involves release of only water and not any greenhouse gas like carbon di-oxide (CO_2) to environment. Hence, in the current depleting fossil fuel scenario since last a few decades, huge money is being spent for achieving enormous abundance of H_2 through advancement of its production technologies [1]. Simultaneously, it is also critical to establish suitable storage routes, as being extremely lightweight, H_2 is difficult to store in gaseous form at large quantum [2]. Compressed and liquid-state H_2 storage technologies are quite matured mostly for static applications and rocket propulsion systems [3]. However, for mobile applications, in order to fuel a car with H_2 instead of gasoline, they are not that advantageous till date for need of robust storage containment adding huge weight into the storage device and vast energy for cooling and maintaining cryogenic condition of the contained H_2 [4]. By contrast, solid-state H_2 storage devices are preferred for their ability to capture and retain H_2 efficiently through adsorption at or near ambient conditions without any vital need of containment's structural integrity [5]. Solid state storage may become a viable technology provided the storage medium can adsorb a large amount ($\Box$6.5 wt %) of hydrogen and can release them easily as recommended by Department of Energy, USA (DoE) [6]. H_2 storage by adsorption within solid substance may happen through either chemical or physical means. An illustration showing various H_2 storage methods has been shown in Fig. 1. The conventional H_2 storage materials used over last few decades are mentioned below with merits and demerits.

- **Metal alloys** with compositions: A_2B (e.g., Mg_2Ni), AB (e.g., TiFe), AB_2 (e.g., $ZrMn_2$) and AB_5 (e.g., $LaNi_5$) were subject to much experimental and theoretical research for development of solid state H_2 storage devices. Although those alloys seem to be quite viable for H_2 storage, their wt% is not promising [7].

- **Metal hydrides** are excellent choice for on-board H_2 storage. But their desorption temperature is very high [8]. Thus, availability of stored H_2 from them is an energy intensive step. Also, recharging them with H_2 for reuse involves incorporation of huge energy in the form of heat. Hence, they are still not favourable choice for on-board H_2 storage.

- **Zeolite** suffers from less specific storage capacity and thus not a suitable choice for mobile purpose [9] despite highly reversible H_2 sorption kinetics and storage attributes.

- **Ammonia borane**, though a promising storage candidate, has the same set of drawbacks as metal hydrides [10].

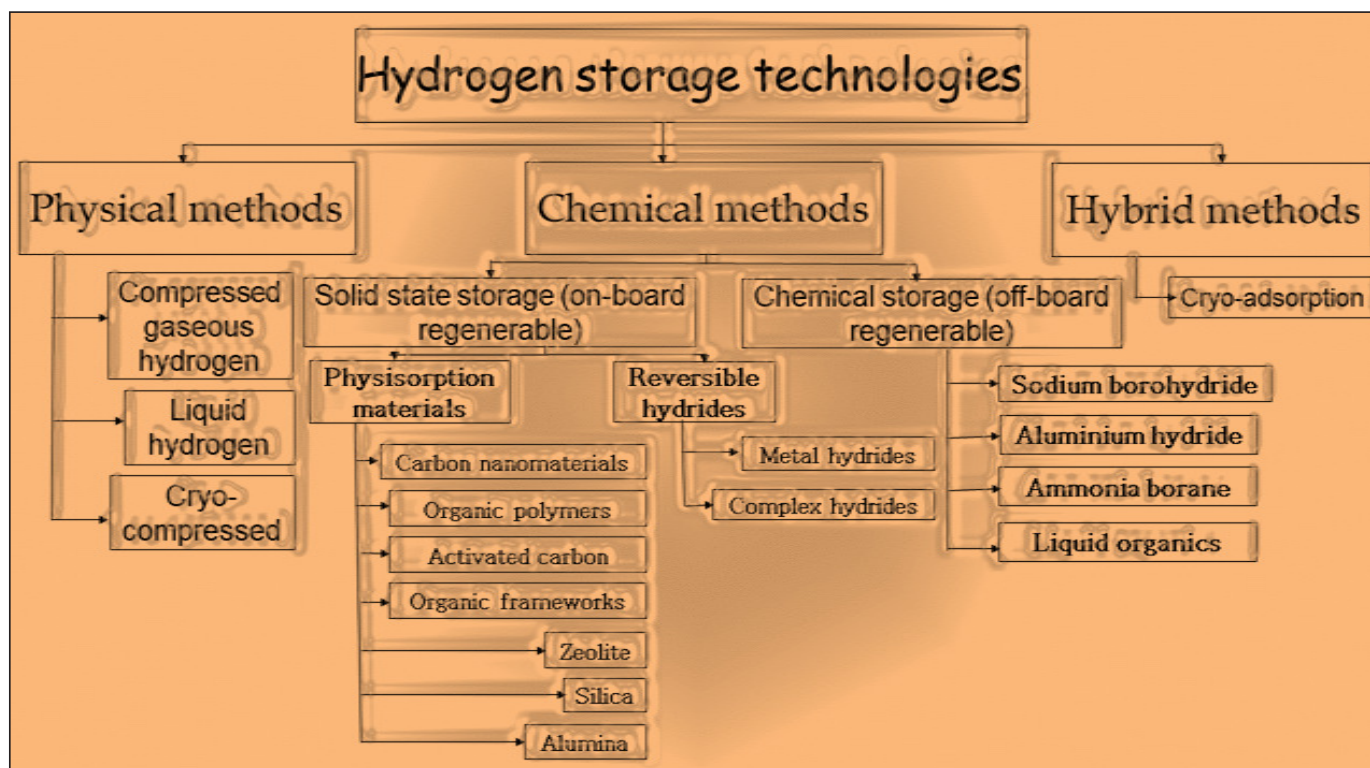- Aluminium, though is very much promising as a H_2

Fig. 1: Different hydrogen storage methods

source, is still too costly for recycling due to expensive electro-winning process [11].

- Organinc frameworks or popularly known as coordination polymers are synthetic crystalline materials which are somewhat analogous to zeolites. Organic linker molecules form the building blocks of organic frameworks, coordinatively binding to inorganic clusters to form a porous framework structure. Despite good H_2 storage capacity at low temperature, even after enough research progress, they suffer with unacceptably low storage capacity at ambiance [12-13].

- Organic polymers can circumvent above limitations in future for their lightweight advantage, but it is still in early developmental stage [14].

With discovery of nanomaterials and emergence of nanotechnology, remarkable improvement in development of material has been achieved at every sphere of life [15]. In nutshell, remarkable rise in surface to volume ratio in nanostructured materials leads to unusual properties by virtue of more and more open structures. These are thus helpful in better utilization than conventional crystalline counterparts. With discovery of graphene, fullerene and carbon nanotubes, it was realized that suitable engineering of carbon nanostructures might lead to enhancement of properties of carbon. The carbon-based nanomaterials have

received outstanding consideration as potential H_2 storage materials for their low cost, good recycling characteristics, easy accessibility, low densities, reasonably good chemical stability, wide diversities of bulk and pore structures, and amenability to synthesize variants or post-synthetically engineer traits using an extensive range of manufacturing, activation and carbonization routes [16]. In general, at any subzero temperature, room temperature and above, up to 400°C or so, thermal stability of pristine and functionalized CNMs are quite good, and there is no significant concern. Though in general, room temperature H_2 storage capacity of pure carbon nanomaterials (CNM) is poor, decoration with metal nanoparticles through chemical functionalization might improve their storage capacity to great extent for ambiance, satisfying DoE's requirements. As physisorption is the key mechanism behind hydrogen storage with CNMs, and they are appreciably stable, theoretically they can serve infinitely large number of absorption-desorption cycles without any apparent depreciation.

In this review, theoretical studies regarding H_2 storage in carbon nanomaterials will be considered first in section 2. Primarily, important aspects regarding mechanism of H_2 capture and retention by pure and functionalized CNMs will be highlighted. The next subsections will follow to impart insights of theoretical simulation for evaluation of binding energy, desorption temperature etc. which

determine efficacy of a particular CNM as a H_2 storage substance. Selected research works regarding theoretical calculation of H_2 storage performance will be discussed in detail for both pure and functionalized CNMs. In section 3, experimental studies regarding H_2 storage in carbon nanomaterials will be covered mentioning synthesis methods and tools for characterization. Both pure and functionalized CNM cases will be considered separately in the following subsections. Pertinent conclusions and future scopes of studies in this direction will be described in section 4.

2. Hydrogen storage in carbon nanomaterials: theoretical studies

Theoretical simulations lead an important job in predicting the interaction mechanism of H_2 molecules with the nanomaterials as well as with functionalized atoms or groups for functionalized Nanomaterials. Simulation techniques can bestow vital information like adsorption energy, preferred adsorption configuration, charge transfer etc. which are difficult or impossible to obtain from experiment. With the invention of large memory, high speed supercomputers, extensive computer simulations are now very much feasible. Also, so many well-established computer codes, both commercial and open access (e. g. VASP [17], quantum espresso [18], WIEN2K [19]) are now available to compute theoretical data for H_2 storage. So, the availability of supercomputers and trusted software packages make it possible to produce H_2 storage database for a large number of systems and suggest the experimentalist the potential systems to attempt in experiments.

2.1 Mechanism of hydrogen capture and retention

2.1.1 Interaction of hydrogen with pure carbon and 'carbon in presence of heteroatoms'

When H_2 in atomic form (H) combines with CNMs with covalent bonding, it is called chemisorption. Being very strong bond, binding energy for chemisroption is quite high (~1 ev) [20]. Thus, much energy is needed to release chemisorbed H_2 from carbon. On the other hand, adsorption of molecular H_2 by CNM is termed as physisorption and being van der Waals type interaction it involves very less binding energy (~0.1 ev) [21] at room temperature. Hence, capture and retention of appreciable amount of H_2 by carbon is thermodynamically possible only at high pressure and low temperature condition. Between these two extremes, decoration of carbon with hetero atoms (specially transition and alkali metal elements) leads to a moderate binding energy situation (0.3-0.5 ev), known

as Kubas interaction [22] where the chemical bond in H_2 molecule interacts with transition metal (TM)s leading to relatively strong adsorption of molecular H_2 for charge donation from highest occupied orbital of the ligand (H_2) to the empty metal orbitals and a subsequent back-donation from filled *d* orbitals into the lowest unoccupied orbital of the ligand. Adopting such a method, it is possible for CNM +TMs to retain appreciable H_2 even at room temperature with ease in release. Precisely, binding interactions must fall within an optimum range in order to maximize reversible storage at or close to room temperature. They can neither be too high nor too low, and the optimum range defines the thermodynamic constraints of the sorbent system. At or near room temperature, the desirable range for the binding energy of hydrogen, regardless of modality, is between 0.1 and 0.6 eV/H_2 (10 and 60 kJ/mol). This range was determined from an analysis based on entropic arguments that the reference entropy values for H_2 are between 0.1and 10MPa, and temperature ranging −20 to 85°C. At−20°C, the enthalpy of adsorption ranges 21 to 32 kJ/molH_2 and at 85°C, the enthalpy increases to 51–71 kJ/molH_2. On this basis, one can determine that the ideal binding affinity falls in the range between 20and 70 kJ/molH_2, leading to a conservative upper range of 58 kJ/molH_2 (0.6 eV/H_2).

2.2 Importance of theoretical simulations for hydrogen storage

Theoretical simulations can present nice picture on charge transfer and orbital interactions which may not be possible or is difficult to get from experimental measurements. From the simulations data, it is easy to conclude whether specific H_2 is having chemisorptions, physisorption, or Kubas [22-23] types of interactions. The structural stability and desorption temperature can also be predicted from theoretical simulations. Keeping above in mind, the role of theoretical simulations for determining hydrogen storage parameters and the limitation of simulation methods, the following sub-sections will highlight overview of quantum simulations, important parameters obtained from theoretical data, importance of dispersion corrections and sensitivity of theoretical data.

2.3 Overview of quantum simulations

Quantum simulation is very useful in terms of providing physical insight of the system as well as producing data that can be compared with experimental data. Quantum simulations need numerical solution to Schrodinger's equation for the system in question containing too many electrons and ions. Thus, the need of sophisticated numerical techniques and approximations

have given birth to a variety of quantum simulation methods, e.g., Density functional theory (DFT) [24-26], Quantum Monte Carlo [27-29], Hatree-Fock [30-31], Multi-reference Configuration Interaction [32], Coupled cluster [33-34], etc. Each of the methods has their own merits and demerits. In the following, we will discuss the role of DFT method in context of H_2 storage.

2.4 Density functional theory

Density functional theory (DFT) is one of the fast and powerful quantum simulation methods that are widely used in many branches of engineering and science. It is based on two theorems given by Hohenberg and Kohn [35] in 1964 and followed by few equations formulated by Kohn and Sham [36].

The ground state density can be obtained from the solution of Koh-Sham equation given by

$$\left[-\frac{\hbar^2}{2m_e}\nabla + \hat{V}_{eff}(\vec{r}) \right]\psi_i(\vec{r}) = \varepsilon_i\psi_i(\vec{r}) \qquad ....(1)$$

with

$$\hat{V}_{eff}(\vec{r}) = \hat{V}_H + \hat{V}_{xc} + \hat{V}_{ext} \qquad ....(2)$$

and $\hat{V}_{xc}$ and $\hat{V}_H$ are given by

$$\hat{V}_{xc} = \frac{\delta E_{xc}[\rho]}{\delta n}, \hat{V}_H = \frac{e^2}{4\pi\varepsilon_0}\int\frac{\rho(\vec{r}')}{|\vec{r}-\vec{r}'|}d\vec{r}' \qquad ....(3)$$

where, $\hat{V}_H$, $\hat{V}_{xc}$ and $\hat{V}_{ext}$ are the Hartree, Exchange-Correlation and external potentials respectively.

From above, it is clear that the only unknown term is the exchange correlation functional. The above equation can be solved by a self-consistent method. Hence, the accuracy of DFT data depends on how superior the exchange correlation functional can be formulated. LDA (Local density approximation) [37] and GGA (Generalized gradient approximation) [38] are two widely used exchange-correlation functional.

2.5 Properties from theoretical simulations

Theoretical simulations can provide very clear and beautiful picture concerning adsorption energy, adsorption configuration, orbital interactions and charge transfer which are difficult to get from experiments.

2.5.1 Adsorption site

It is vital for H_2 storage simulations to find the adsorption configuration with minimum energy. Geometry optimization might take longer for presence of weak Van der waal's forces. Additional consideration of spin polarization is necessary for systems containing transition metal with magnetic signature. Accuracy of configuration depends also on setting parameters such as energy cut off for the plane wave as well as K-points for sampling the Brilloiun zone. Hence, convergence needs to be tested with respect to energy cut off for the plane wave as well as number of K-points. The distance of the H_2 molecule with the nearest atom of the host or the dopant might impart idea regarding bond strength. Lower distance (bond length) signifies stronger adsorption. To investigate adsorption properties of hydrogen molecules on metal-doped zeolite template carbon (ZTC), more than 10 adsorption configurations have been simulated by Han et al. [39]. It is found that H_2 molecules tend to symmetrically locate around Sc, Ti or V atoms doped on C39H15 surface [40]. Therefore, while building the initial model of H_2 adsorption configuration, the H_2 molecules are uniformly loaded around the doped metal atoms in almost symmetric positions, with a gradually raised loading number of H_2 molecules. First-principles geometric optimization has been individually performed for each additional H_2 molecule to obtain all the relaxed and stable adsorption structures. Representative adsorption configurations after geometry optimization of three and six H_2 molecules at A1-A10 sites of Sc-C39H15 are shown with the top (left) and side (right) views in Fig. 2.

2.5.2 Adsorption energy

For practical H_2 storage device, H_2 adsorption energy must fall within a window. DoE has prescribed that the binding energy of H_2 must fall within the range 0.2-0.7 eV for practical implementation of H_2 as fuel. The adsorption energy of H_2 on the host can be computed from the expression

$$E_{ads} = E_{Host+H_2} - E_{Host} - E_{H_2} \qquad (4)$$

Where E_{Host+H_2} is the energy of the host (nanostructure+dopant) plus H_2, E_{Host} is the energy of the host and E_{H_2} is the energy of an isolated H_2 molecule. As per convention, negative value of adsorption energy indicates that binding is energetically favorable. All three energies in the above equation should be computed with same simulation condition as the computed energy may vary with setting parameters. Adsorption energy is very much sensitive to choice of basis set. The adsorption energy may also be different for different adsorption sites. Ganji et al. [41] demonstrated that adsorption energy values and bond lengths obtained are sensitive to choice of basis sets, e.g. SVP, TZVP or TZVPP. The results generated through dispersion corrected approaches display excellent agreement between the theory and experiment, especially
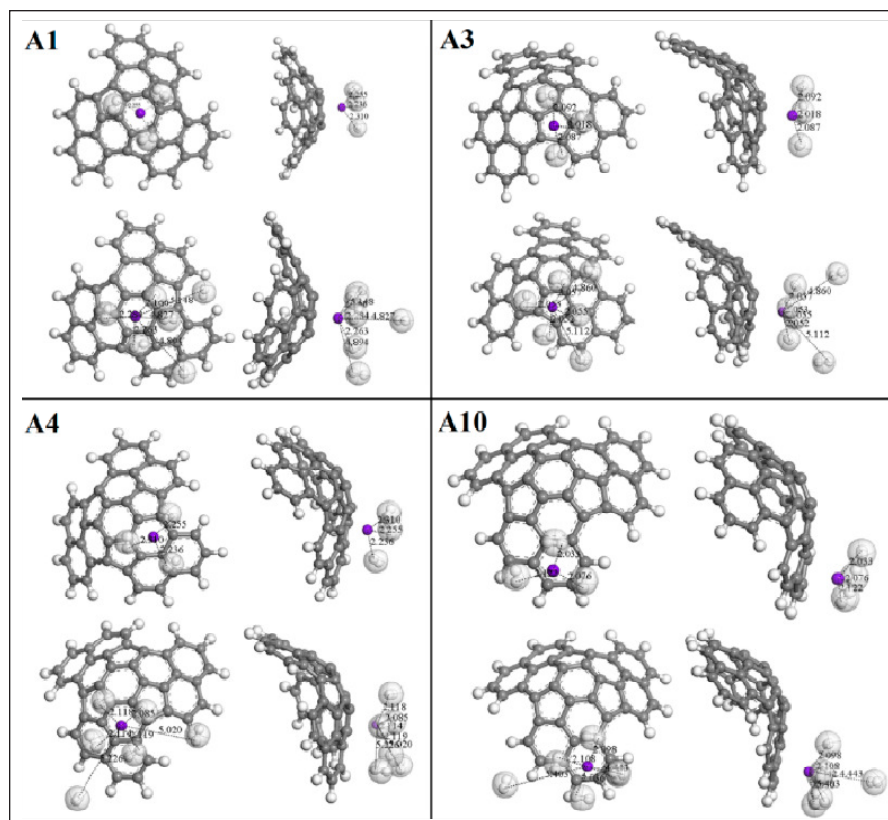
Fig. 2: Adsorption configurations of three (above panels) and six (below panels) H₂ molecules on A1, A3, A4, A10 sites respectively in Sc-doped-ZTC (Sc-C39H15). The top and side views are respectively shown by the left and right parts in each schematic unit, and the grey, white and violet balls identify carbon, hydrogen and scandium atom. (From Han et al. 2019 [39], With permission.)

for the large basis set. Meanwhile, the moderate basis set (TZVP) gives a reasonably good result compromising computational cost and accuracy in quantum chemistry methods (Table 1).

Table 1 Adsorption energy and bond length of low energy configuration systems in H₂-coronene system (Ref.: Ganji et al. 2015 [41], with permission.)

Basis set	C-H bond length (Å)	E_{ads} (kJ mol^{-1})
SVP	3.394	+2.11
TZVP	3.294	+1.97
TZVPP	3.295	+1.91
vdW-SVP	3.301	-4.73
vdW-TZVP	3.288	-4.97
vdW-TZVPP	3.289	-5.013

2.5.3 Charge transfer and orbital interactions

The amount of charge getting transferred between the bonded species can be quantified from simulation data. From charge transfer data, idea regarding bonding mechanism can be obtained. The bonding between H and host material is strong for the chemisorption, weak for physisorption and intermediate for the Kubas type of interaction. Higher charge transfer indicates stronger bonding. For pure CNMs, the adsorption mode is physisorption and charge transfer is negligible. For chemisorption, the H₂ atoms get dissociated charge transfer is huge. Both physisorption and chemisorption are thus not suitable for practical implementation of H₂ storage. For metal doped carbon nanomaterials, there is charge transfer from metal's *d* orbital to H's *s* orbital followed by back donation through Kubas interaction. In this case the binding energy comes in the range 0.2-0.7 eV as prescribed by DoE and is most suitable for practical implementation of H₂ storage at ambient condition. Hence, type of interaction operating can be determined from charge transfer data. To find the quantum of charge transfer, one need to take care regarding number of valence electrons taken for the simulation. Bader charge analysis [42] and Mulliken's charge analysis [43] are two powerful techniques to find the amount of charge transfer during orbital interactions. To visualize the spatial variation of charge density, the pictorial plot of charge density can be obtained using visualizing softwares like XCRYSDEN [44], VESTA [45] etc. The orbital interactions and hybridization can be obtained qualitatively from the plot of partial density of states which describe the contribution of Density of states from each orbital of each atom. There should be consistency between the charge transfer from Bader charge analysis, partial density of states, and charge density plot. Wong et al. [46] compared hydrogen adsorption capability of graphene decorated with different metals. In the charge density difference isosurfaces, yellow indicates regions of charge gain and blue indicates regions of charge loss (Fig. 3). The Al atoms, a light metal, show greater charge loss and a smaller region of remaining charge density than the heavy metal Ni atoms. This might be one reason for heavier metal atoms possessing stronger hydrogen binding
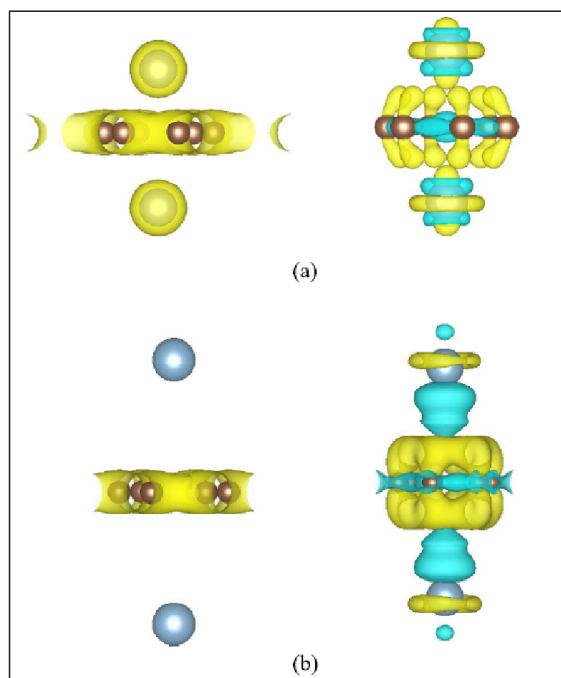
Fig. 3: Isosurfaces of charge density and charge density difference for (a) Ni and (b) Al adatoms adsorbed on graphene. (From Wong, J., et al. 2014 [46], with permission.)

energy as they have greater charge which can interact with hydrogen molecules.

2.6 Importance of dispersion corrections for hydrogen storage

As H_2 adsorption involves weak Van der Waals interactions, one must include dispersion corrections in simulations as the standard DFT with GGA exchange correlation functional can't handle 'long term electron correlation' effects. The dispersion correction increases the binding energy of H_2 molecules slightly. There exist various schemes for incorporating the dispersion corrections in DFT such as Grimme's DFT-D2 [47], Grimme's DFT-D3, vdW –DF [48-50], optPBE-vdW etc. The binding energy of H_2 molecules will differ little bit for various dispersion schemes.

2.7 Sensitivity of theoretical data

The data obtained from DFT simulations depend on the exchange correlation functional, simulations parameters, dispersion correction schemes and simulation software. So, one need to be careful regarding choice of simulation parameters. As the binding energy is computed from difference of energy, simulations should be considered with identical setting parameters otherwise it may give erroneous result. Energy cut-off and *k*-point grid are important parameters to be taken care of for accuracy.

2.8 Theoretical studies aiming hydrogen storage in pure CNMs

Most theoretical research experience regarding H_2 storage in pure CNM encompasses CNT, fullerene, graphene, graphyne, pentagraphene etc. as the storage material. A few notable theoretical observations are discussed below.

Lee et al. [51] demonstrated through DFT calculation that H atoms can be stored predominantly through the tube wall by annihilating the C-C midbond. They also found that up to certain H content, the nanotube's wall is stable. By reviewing Lee et al.'s work, Froudakis [52] commented that maximum H_2 storage capacity is mainly governed by the steric interaction among H_2 molecules and between H_2 and the tube wall. Consequently, sorption capacity increases linearly with tube diameter (Fig. 4). But, too much H_2 storage will cause large repulsion energies and ultimately break down the tube wall.

Using first-principles DFT calculations, Yoon et al. [53] explore systematically the capacity of charged carbon fullerenes C_n ($20 \leq n \leq 82$) as H_2 storage media. The theorized
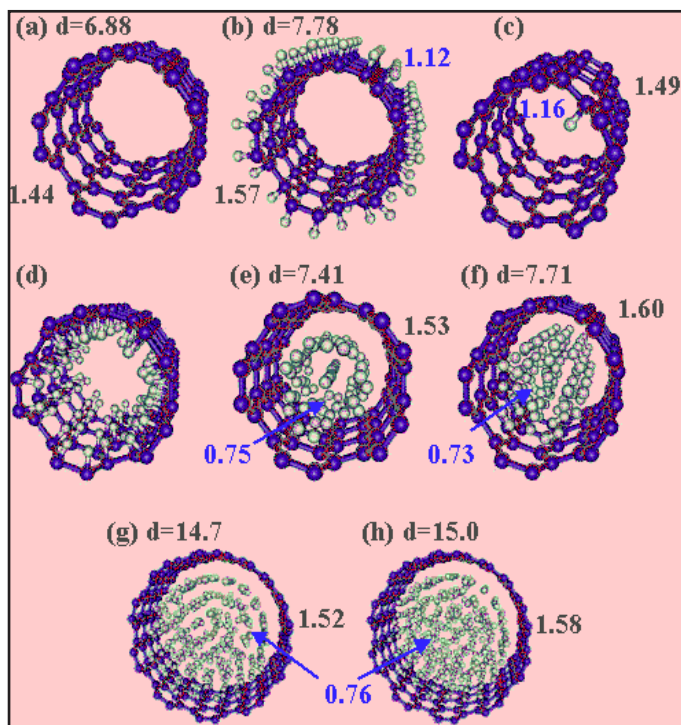
Fig. 4: Chemical adsorption of H in SWNTs: (a) the (5, 5) SWNT before the storage; (b) hydrogens adsorbed on the outside of the tube wall; (c) adsorption of a single hydrogen atom on the inside of the wall; (d) the initial geometry; (e) the fully relaxed version of geometry (d); (f) molecular hydrogen inside the (5, 5) SWNT; (g) H_2 inside the (10, 0) SWNT with an allocation of two H per C atom and with 2.4 H per C atom (f). Bond lengths are in Å. (From Froudakis, 2002 [52], with permission.)
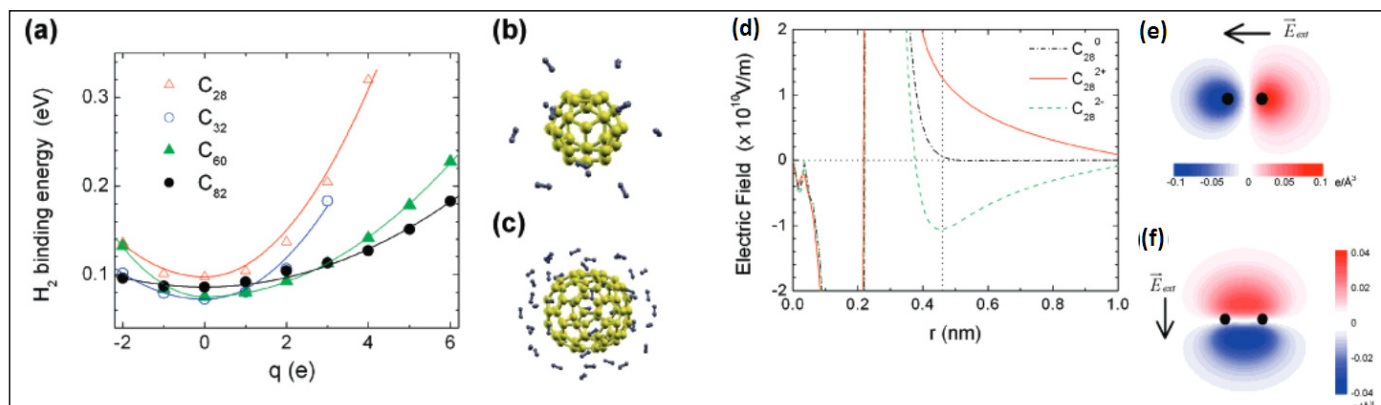
Fig. 5: *(a) Binding energy of molecular hydrogen on charged or neutral fullerenes. The DFT calculations (data points) are compared with semiclassical calculations (solid lines), and for both cases the binding energy increases quadratically with the net charge. (b, c) Structurally optimized hydrogen-fullerene complexes of (b) $12H_2$-C_{28}^{3+} and (c) $43H_2$-C_{82}^{6+}, with a hydrogen uptake of 6.67 wt % and 8.04 wt %, respectively. (d) Electric fields associated with neutral and charged fullerenes, C_{28}^q (q=-2, 0, +2), at the center of a hydrogen molecule located on top of a hexagonal ring. (b, c) Charge density variations of a hydrogen molecule induced by an electric field of $2\times10^{10}$ V/m applied (b) parallel and (c) perpendicular to the molecule axis, respectively. (From Yoon et al., 2007 [53], With permission.)*

Table 2 An account of noteworthy theoretical works for assessing H_2 storage in pure CNMs [55-62]

Carbon nanomaterial type	Storage condition		Hydrogen storage capacity (wt %)	Remarks	Reference
	Temperature	Pressure			
Fullerene	300 K	Ambient	>8	Fullerene nanocage	[55]
Graphite	300 K	70 MPa	8	Fullerene-intercalated graphite	[56]
Graphene	Ambient	Ambient	Up to 8	Graphene multilayer	[57]
Carbon nanotube	77 K	4 MPa	7.1	SWCNT	[58]
	Ambient	50 atm	~1	SWCNT	[59]
	200 K	100 atm	0.9-1.4	SWCNT	[59]
Nanoporous carbon material	77 K	3.8 MPa	6	Quasi-periodic icosahedral	[610]
Carbon nanoscroll	293 K	10 MPa	1.21		[61]

enhanced binding is delocalized in nature, surrounding the whole surface of a charged fullerene. The enhanced binding is attributed to the polarization of the H_2 molecules by the high electric field generated near the surface. At full H_2 coverage, these charged fullerenes can gain storage capacities of up to 8.0 wt % (Fig. 5).

Tozzini et al. [54] proposed a multilayer graphene-based device. There the storage and release of hydrogen are obtained by controlling the corrugation of individual layers of graphene. Their DFT calculation quantifies the tunability of the hydrogen-graphene binding energies by changing the sheet's out-of-plane deformation up to 0.2 Å. The binding energy is found to be varied by more than 2 eV, with the convex regions allocating the energetically favored hydrogen binding sites. The corrugation of the graphene sheet and the controlled inversion of its curvature yield fast storage and release of hydrogen, indicating a maximum storage of 8 wt% H_2 (Fig. 6).
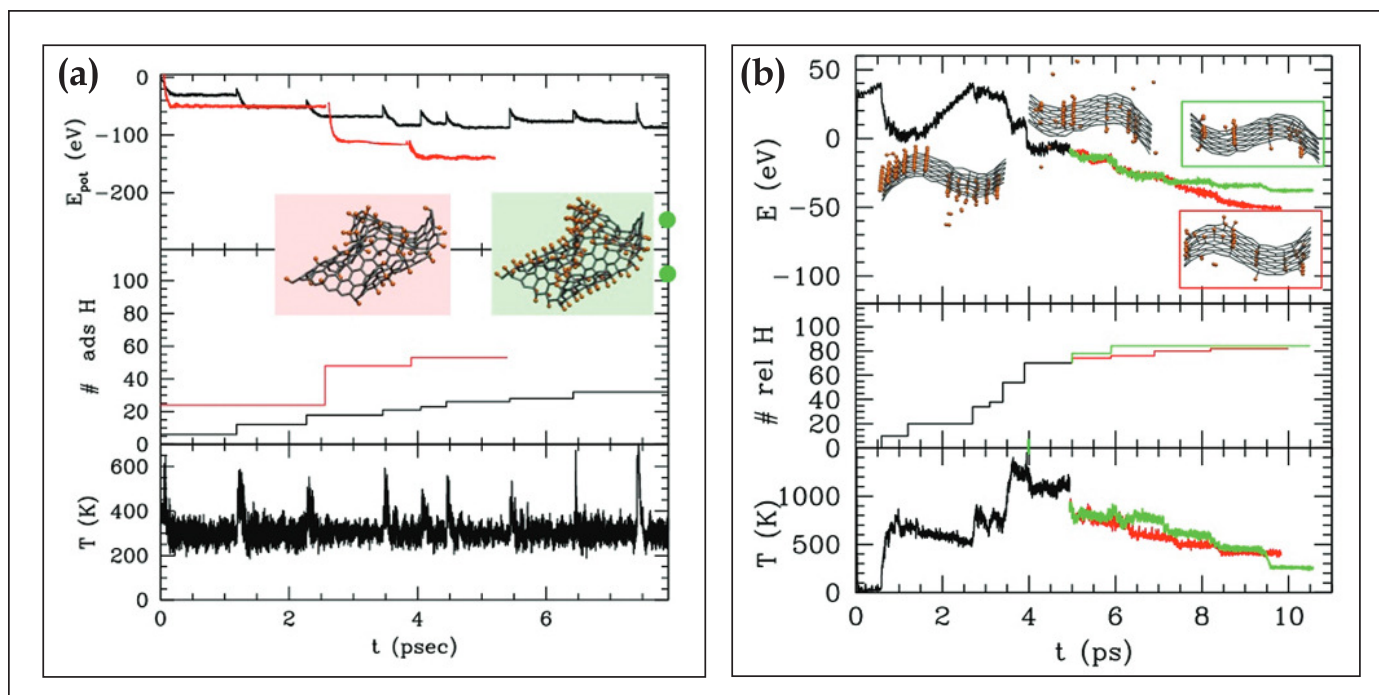
Fig. 6: *(a) Simulations of hydrogen adsorption. Top: potential energy changes due to chemisorption. Centre: number of chemi- sorbed H atoms. Red: protocol (i), black: protocol (ii). Bottom: temperature variation during the simulations of protocol (i). Green dots indicate the potential energy and adsorbed H for full loading. Snapshots from the simulations are reported, corresponding to the partially loaded (pink background) and fully loaded (green back- ground) configurations. and (b) Simulations of hydrogen release. The temperature (bottom), potential energy (top), and number of released H atoms are reported. Black: inversion phase, temperature not controlled. Red: thermalization with recovery to starting configuration. Green: thermalization keeping the curvature inverted. The corresponding two final configurations are reported in red and green boxes. Snapshots of the starting and half-period conformations are also reported. (From Tozzini et al., 2011 [54], with permission.)*

Besides the above, a number of storage mechanisms have been hypothesized by theorist over the globe. A brief compendium of theoretical research for assessing H_2 storage by various CNMs has been presented in Table 2 [55-61]. However, validation of such theoretical hypotheses is often not feasible for lack of comparable pragmatic scenario. It is noteworthy to mention specially an interesting conjectural observation reported by Gao et al. [62] about ultrahigh hydrogen storage capacity of holey graphyne where the C–C 2D network is alternately connected between benzene rings and sp bonds leading to a more open structure.

2.9 Theoretical studies aiming hydrogen storage in functionalized CNMs

Efforts in assessing potential of functionalized carbon Nanomaterials for H2 storage are quite vast, although not entirely exhaustive. The results are quite promising for room temperature H_2 storage by CNMs. A few important such works are discussed below.

Gangan et al. [63] predicted by DFT simulations that a Ytrrium atom attached on graphyne surface can adsorb up to a maximum of 9 molecular hydrogens (H_2), with a uniform binding energy of ~0.3 eV/H_2 and an average desorption temperature of around 400 K, leading to 10 wt% of H_2 storage. They also identified two possible adsorption sites for Yttrium on graphyne: one hexagonal and another triangular, capable of adjoining 9 and 5 H_2 molecules respectively (Fig. 7). Authors have checked the stability of the system at room temperature by ab-initio Molccular Dynamics simulations. Interestingly, they have computed the diffusion energy barrier for the clustering of Y atoms. It was found that there exist substantial energy barrier which prevents movement of metal atom.

Chakraborty et al [64] have also reported hydrogen storage capability of Y doped single walled carbon nanotubes. They presented the structural stability, H_2 adsorption capability and H_2 desorption kinetics of Y-decorated single walled carbon nanotube (Fig. 8) through first principle simulations. It was found that A single Y atom attached on SWCNT is shown to physisorb up to six H_2 molecules. The interaction of H_2 with metal atom is through Kubas type of interactions.

Zirconium is the next to Yttrium in the periodic table. Yadav et al. [65] explored the hydrogen storage capability of Zr doped graphene. The advantage of graphene is that
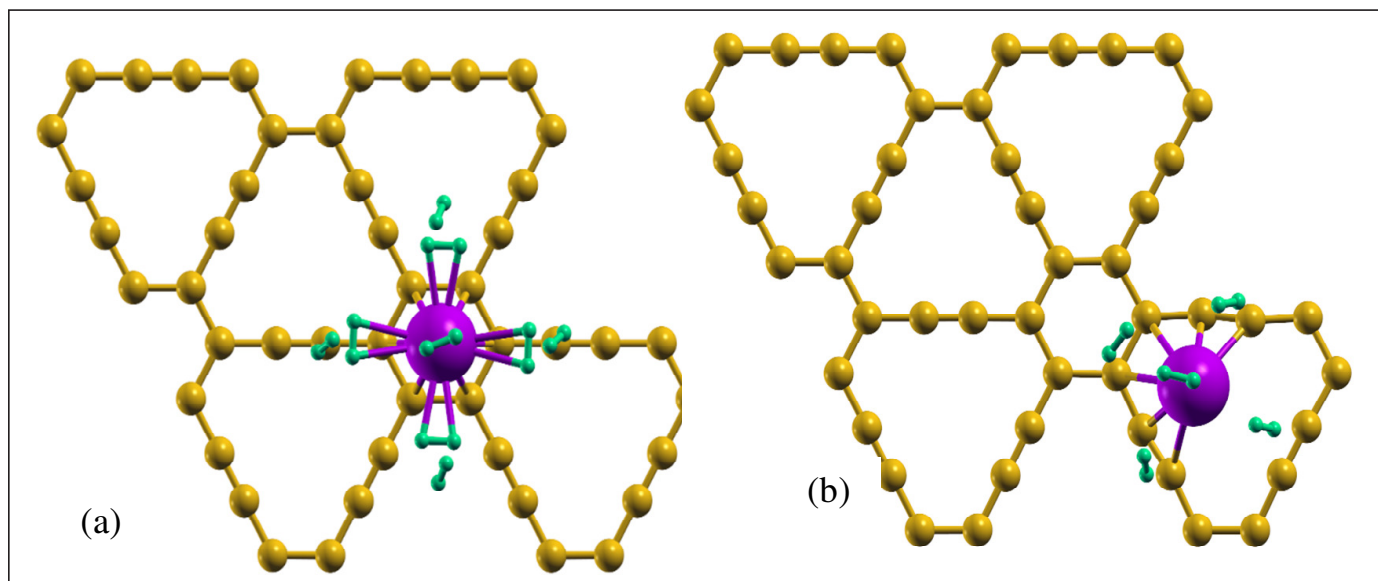
Fig. 7: Two possible adsorption site of Y on graphyne (a) Hexagonal site with metal binding energy of -3.15 eV; the configuration of 9 H2 molecules it can adsorb and (b) Triangular site with metal binding energy of -4.05 eV; the configuration of 5 H2 molecules it can adsorb. (From Gangan et al., 2019 [63], With permission.)
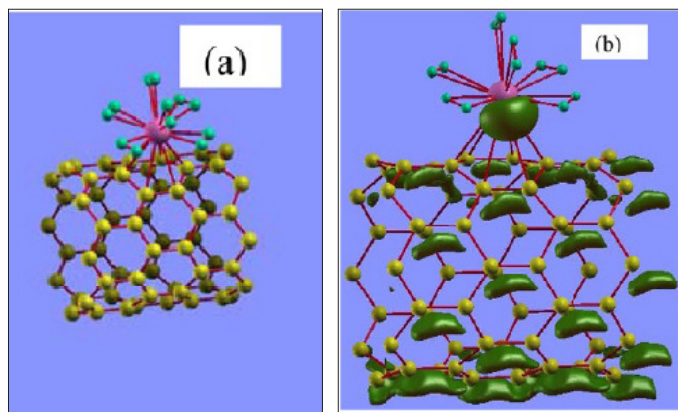

Fig. 8: *(a) Final relaxed structure of SWCNT+Y+6H$_2$ complex, (b) Isosurface for charge density difference between SWCNT+Y+6H$_2$ system; iso-value −0.5e. (From Chakraborty et al., 2012 [64], with permission.)*

being 2D layer metal can be loaded on both the surfaces. It was found that single Zr can store 9H$_2$ molecules leading to a theoretical H$_2$ uptake of 11 wt%, much higher than DoE's requirement of 6.5 wt% (Fig. 9) [65]. It was observed that graphene+Zr is magnetic whereas its magnetic moment reduces after adsorption of successive H$_2$ molecules. Interestingly, they found that the binding energy as well desorption temperature of individual H$_2$ depends on the magnetic moment of the system. Authors [65] have presented an empirical relation between magnetic moment and desorption temperature of H$_2$ for this system. For a system with a large magnetic moment, the charge transfer to the H$_2$ molecule is higher, leading to higher desorption temperature (T$_D$). Controlling the magnetic character of the

system through doping may be an effective way to bring T$_D$ in to the desired window.

Apart from above, there are many more theoretical studies reported available for predicting H$_2$ storage of CNMs in presence of heteroatoms. A brief account of a few such works is summarized in Table 3 [62, 66-75]. To fortify with a few recent interesting studies, Deniz et al. [76] showed through grand canonical Monte Carlo (GCMC) simulations that the total gravimetric adsorption capacity of Li-doped fullerene pillared graphene nanocomposites (Li-FPGNs) with doping ratio of Li:C=15:100 could reach 9.1 wt% at 77 K and 1 bar, which corresponds to about two times rise in the hydrogen storage performance of pristine FPGNs.

2.10 Challenges and issues in theoretical studies

One of the significant issues for H$_2$ storage for metal-doped carbon nanomaterial is the metal-metal cluster. From computation of metals' diffusion energy barrier, one can get idea on possible metal loading pattern in order to avoid metal-metal clustering. Secondly, oxygen interference is a great practical problem and considering that within the model is a difficult challenge [77]. Hence, there are issues and challenges for predicting H$_2$ storage capacity in terms of wt% from theoretical simulations. Simulation results are sensitive to the replication methods and setting parameters. For example, as mentioned earlier, LDA exchange correlation [46] overbinds the H$_2$ molecules whereas GGA exchange correlation [47] underbinds the H$_2$ molecules. So, one need to be cautious regarding choice
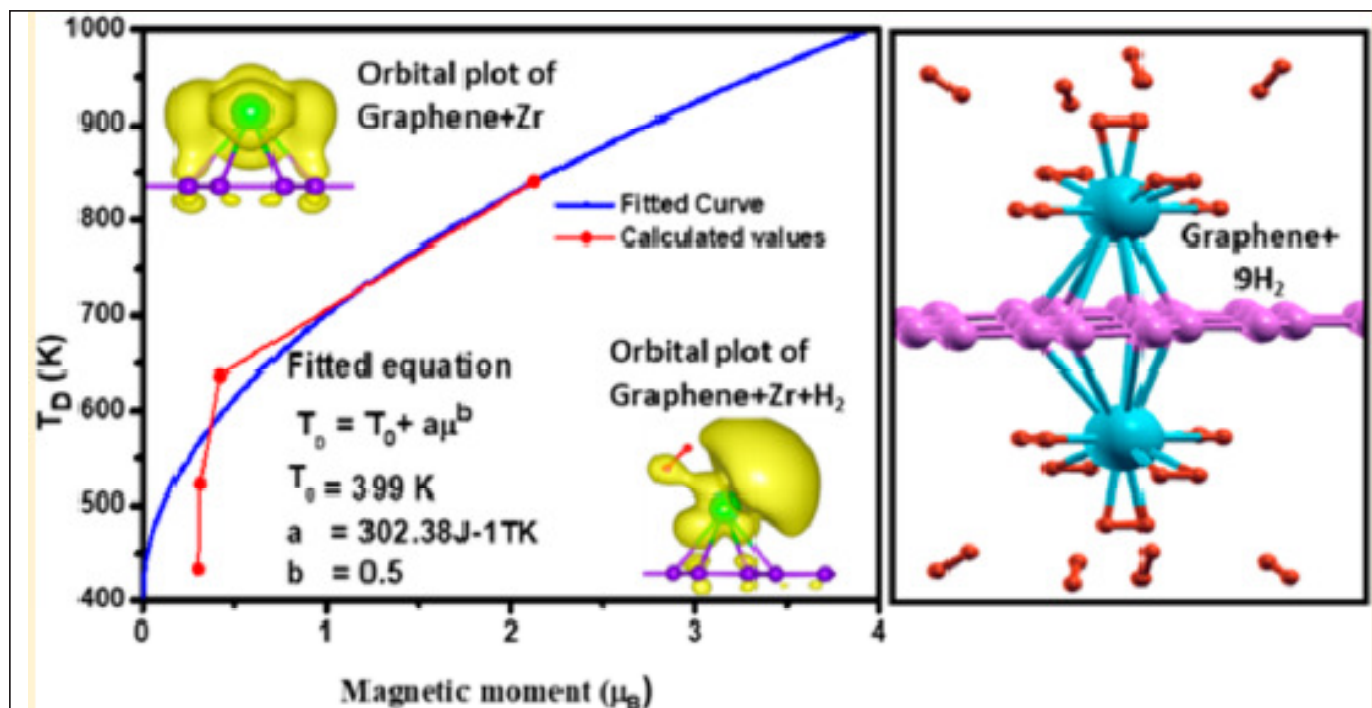
Fig. 9: Theoretical DFT study of zirconium-doped graphene, capable of storing 11 wt% H_2 (From Yadav et al., 2017 [65], with permission.)

Table 3 A few noteworthy theoretical works regarding H_2 storage on functionalized CNMs [62, 66-75]

Carbon nanomaterial type	Storage condition			Hydrogen storage capacity (wt %)	Remarks	Reference
	Temperature	Pressure	Decorating element			
Fullerene	Ambient	Ambient	Ca	>8.4		[66]
	Ambient	Ambient	Ti	7.5		[67]
Graphene	77 K	10 bar and above	Li	>5	Pillared graphene oxide	[68]
	Ambient	Ambient	Ca	~5	Zigzag graphene nanoribbon	[69]
	Ambient	20 bar	Li	6.5	Pillared graphene sheet	[70]
	Ambient	Ambient	Li	12.8		[71]
	Ambient	Ambient	Al	13.79		[72]
Carbon nanotube	300 K	10 MPa	Li	1.27	Single walled	[73]
	Ambient	Ambient	Si	2.5	Single walled	[74]
Graphyne	Ambient	-	Ca	7		[75]
Carbon nanoscroll	293 K	10 MPa	Li	3.78		[62]

Fig. 10: TEM image of (a) pure graphene, (b) graphene functionalized with HNO_3, (c) graphene decorated with Pt and (d) graphene decorated with Pd (From Huang et al., 2011 [88], With permission.)
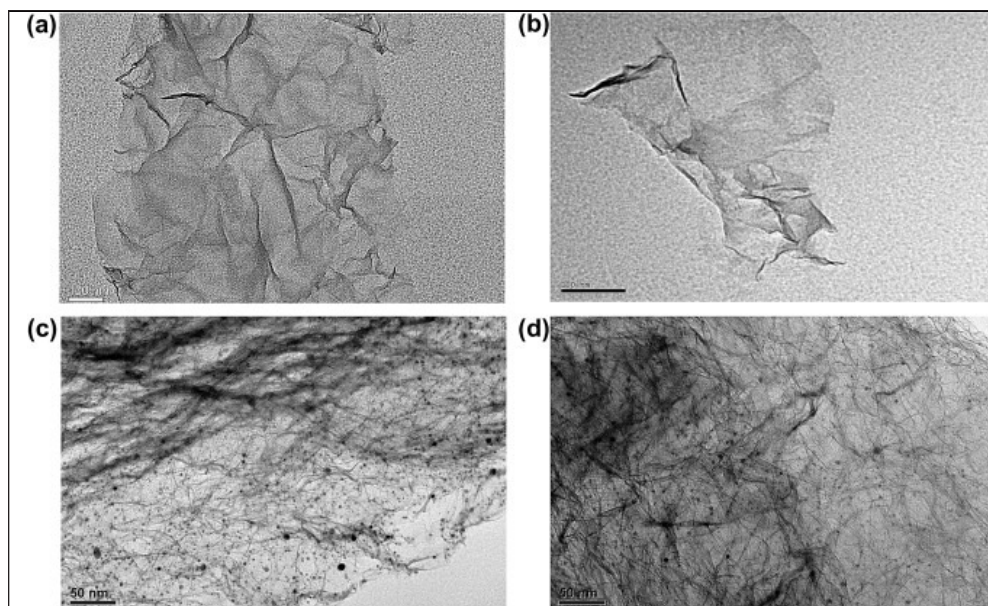
in pure or decorated form, its characterization and finally hydrogen adsorption and measurement of stored hydrogen. Synthesis of graphene involves exfoliation of graphite through either mechanical or chemical route. CNT is generally synthesized adopting chemical vapour deposition (CVD) technique. Functionalization of CNM involves a wet chemical method where first carbon arms are activated by reacting with oxidizing chemicals. The activated sites act as receptor of heteroatoms. In the next step, transition metal (TM) atoms are conjugated with the active sites of the oxygenated
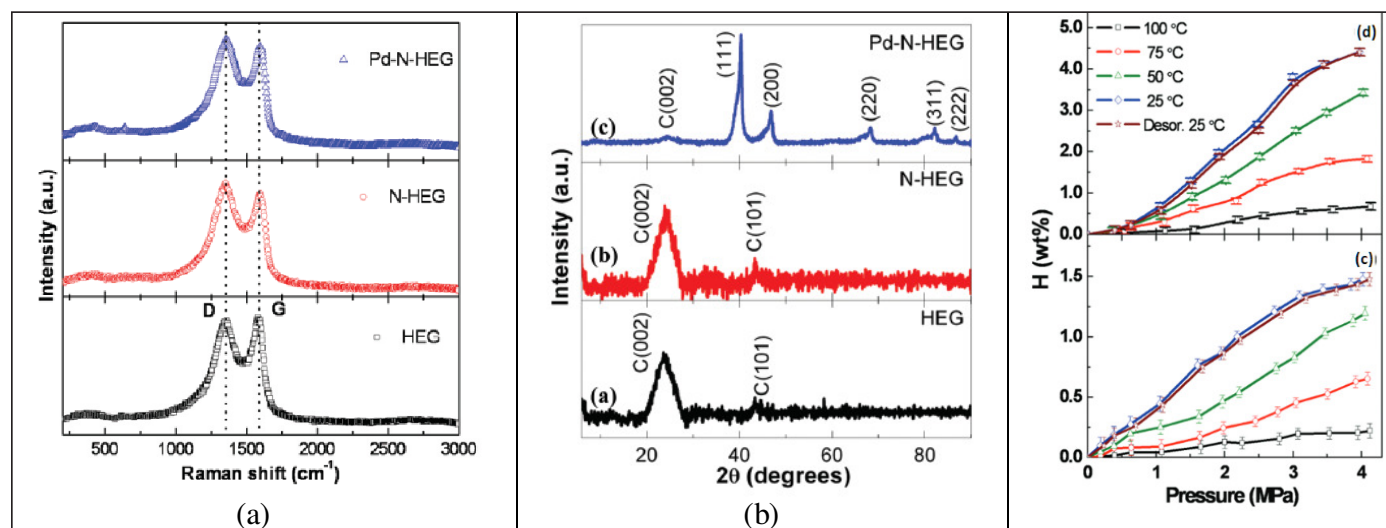

Fig. 11: (a) Raman spectra of pure and nitrogen and palladium decorated hydrogen exfoliated graphene (HEG): rise in intensity of D band suggesting accumulation of strain due to exfoliation. (b) XRD: extra peaks on top curve showing incorporation of Pd nanoparticles. Pressure− composition isotherms of (c) N-HEG and (d) Pd- N-HEG in the temperature range 25−100° C and 0.1 − 4 MPa pressure. (From Parambhath et al., 2012 [89], with permission.)

of the simulation methods and the resulting prediction from simulation details. For adsorption of H_2 molecules on carbon nanostructures, weak Van der Waals interactions are there. So, one should carefully take into account of those interactions while computing binding energy of H_2 molecules on carbonaceous substance.

3. Hydrogen storage in carbon nanomaterials: experimental studies

Experimental hydrogen storage studies involve preparation of CNM (e.g. graphene or CNT) either

CNM using suitable chemical, composing of the TM. Finally, a reduction reaction is performed using an appropriate reducing agent to eliminate oxygen [78-82]. This is followed by purification and drying to obtain TM-decorated CNM. In case of CNT, functionalization can also be performed during its synthesis by CVD [83-87]. Characterization involves microscopic observation through TEM [88], Raman spectroscopy [89], XRD [89] etc. (Fig.s 10-11), for determination and visualization of structure. After pressurized hydrogenation, the adsorbed hydrogen quantity is measured through volumetric and
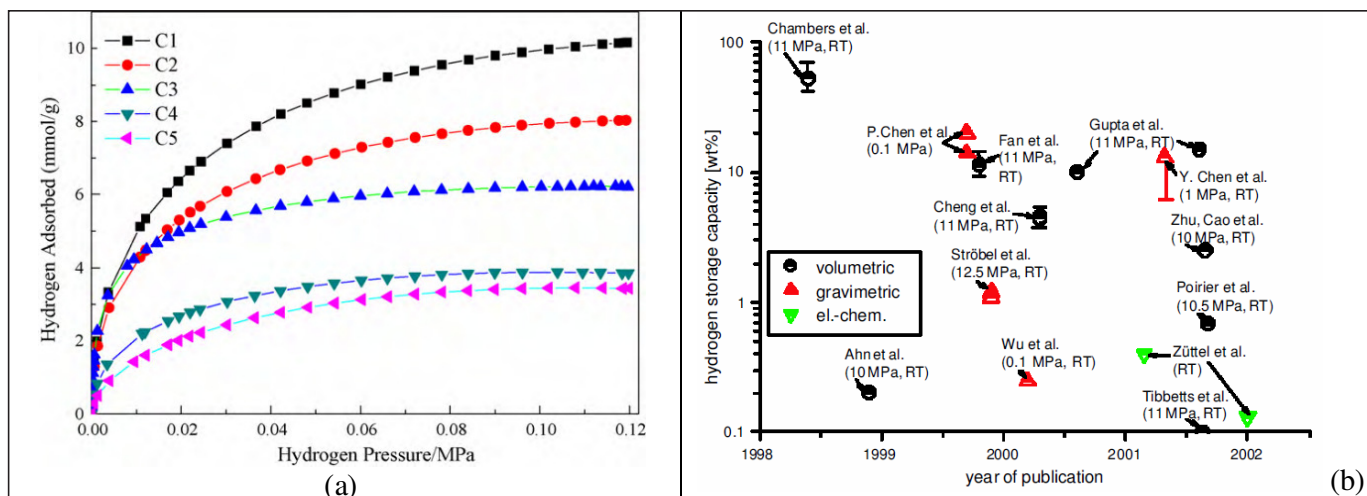
Fig. 12: (a) Adsorption isotherm of hydrogen at 77 K on different carbons:C1-C5 denote carbon samples treated with KOH, K_2CO_3, NaOH, H_3PO_4 and $ZnCl_2$ respectively for activation. (From Sun et al., 2010, With permission.), (b) Year-on-year experimental scatter in hydrogen storage for single walled carbon nanotubes (From Hirscher et al., 2003 [91], With permission.)
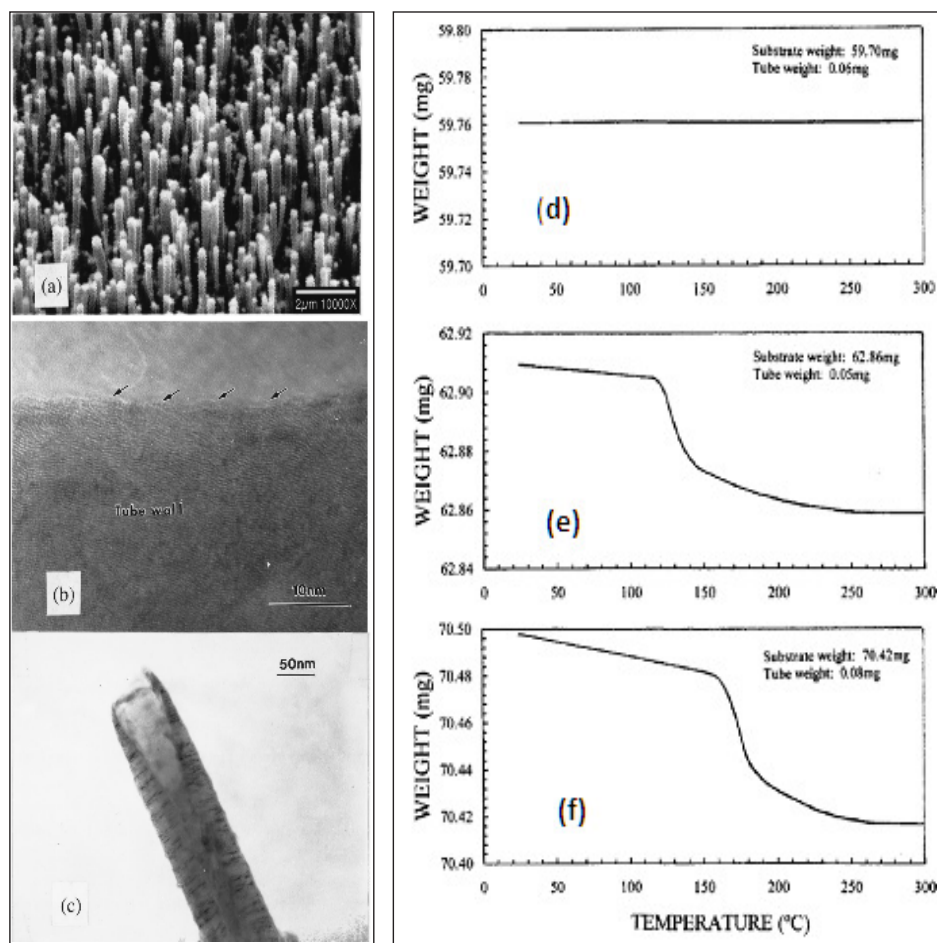

Fig. 13: (a) SEM picture of the CNTs synthesized by plasma-assisted CVD; (b) TEM picture of the tube wall structure, which indicates that there are open-ended layers; (c) catalyst removed CNTs. and TGA spectra of the hydrogen release in aligned carbon nanotubes: (e) as-prepared sample without hydrogen uptake; (f) as-prepared sample stored at room temperature under 2 atm hydrogen; (g) catalyst-free samples stored at room temperature under 10 atm. (From Chen et al., 2001 [92], with permission.)

gravimetric methods [90] (Fig. 12a). For issues related with purity, clustering, agglomeration of decorating nanoparticles and oxygen interference, experimentally observed results seldom match with theoretical predictions (Fig. 12b) [91].

3.1 Experimental studies aiming hydrogen storage in pure CNMs

Chen et al. [92] synthesized aligned (CNTs) with diameters of 50–100 nm, by plasma-assisted hot filament chemical vapor deposition. Using quadruple mass spectroscopy and thermogravimetric analysis they found a H_2 storage capacity of 5–7 wt% reproducibly at room temperature under modest pressure of ~10 atm. Heating the samples to 300 °C and removal of the catalyst tips may increase the H_2 storage capacity up to 13 wt% and decrease the pressure required for storage (Fig. 13).

Lueking et al. [93] exhibited that selective exfoliation of a carbon nanofiber is a means by which H_2 interaction with the carbon structure can be controlled. This
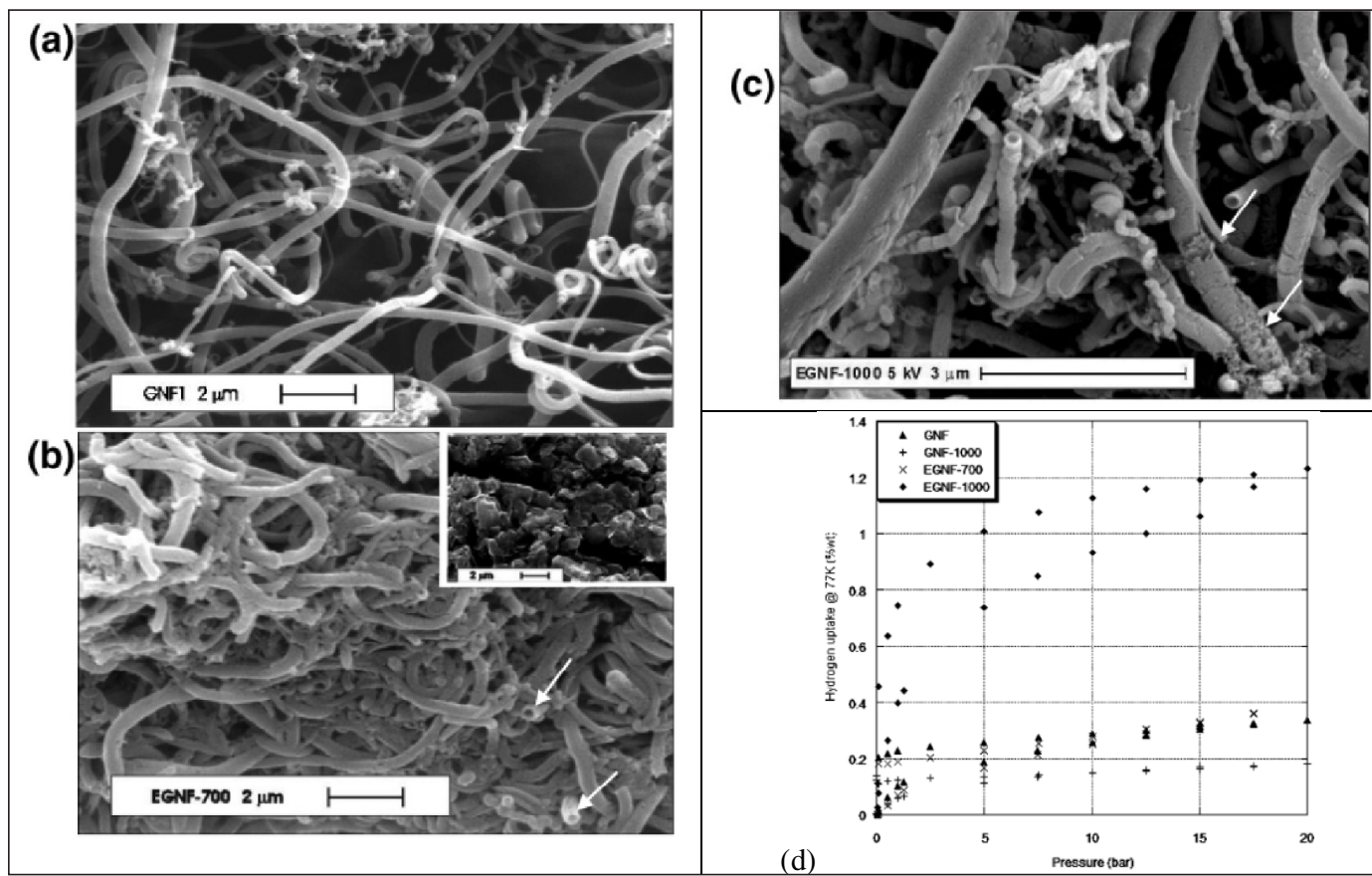
Fig. 14: *SEM micrographs indicate the changes in surface structure upon various stages in the exfoliation process. (a) GNF1 has relatively smooth surfaces; (b) EGNF-700 shows roughened surfaces, variations in fibre termination (arrows), and the appearance of disk-like carbon structures indicating partial destruction of the GNFs; (c) EGNF-1000 shows roughened surfaces, surface defects (arrows), and expanded regions. (d) H_2 uptake for the various GNFs at 77 K and up to 20 bar (From Lueking et al., 2005 [93], with permission.)*

in turn results in control of binding energy to tune the operative adsorption temperature (Fig. 14). Rise in exfoliation temperature and time resulted in huge lattice expansion causing many folds increase in surface area and a consequent uplift in H_2 uptake.

In another elegant work regarding fabrication of graphene-based materials having hierarchical nanopore, Guo et al. [94] developed suitable oxidative heat treatment of exfoliated graphene oxide. It is conceived from their work that escape of oxygen functional groups through formation of CO_2 leaves pores of assorted varieties (Fig. 15). This leads to wave-like structure between individual graphene layers causing enhanced H_2 storage (4 wt %).

Table 4 [95-118] is a compilation of a few more notable experimental results to show H_2 storage performance of various physical CNMs of known purity. Recently, in an elegant report, Jokar [119] showed that acidic vapor has no deleterious effect on stability of the structure of CNT formed by a special CVD method involving Co-Mo/MgO catalyst, and nanoporous activated carbon. Additionally,

highest capacity of H_2 adsorption was detected for nitric acid-modified carbon. It appears that experimental findings regarding H_2 storage performance are often less reliable for lack of reproducibility, as judged by many researchers [120-121]. The chief reason behind such diverse observation is variation of sample quality in terms of purity across different laboratories and variety of processing routes for preparation and characterization of the samples. Practical achievable H_2 adsorption for pure CNM is often less than 1 wt% at ambiance. With lower temperature and higher pressure however, better results could be achieved [103, 106, 109, 111], sometimes even exceeding the theoretical prediction [113].

3.2 Experimental studies aiming hydrogen storage in functionalized CNMs

Reyhani et al. [122] studied H_2 storage performance of MWCNT decorated with Ca, Co, Fe, Ni, and Pd. H_2 molecules are adsorbed on the defect sites and transported to the spaces between adjacent carbon via diffusion through both defect sites and opened tips into the layers.
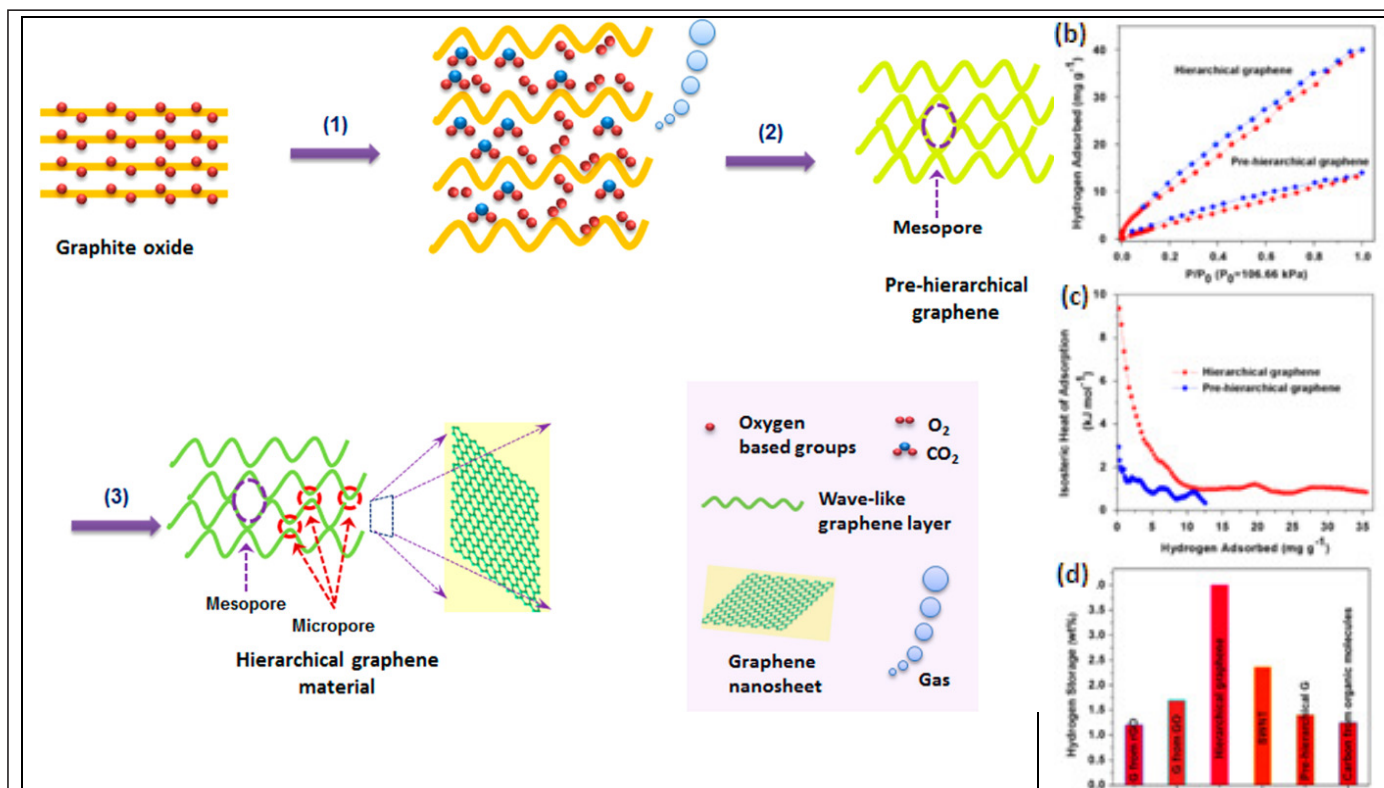
Fig. 15: *(a) Scheme for the formation process of the hierarchical graphene-based material. (b) Hydrogen adsorption and desorption isotherms of the hierarchical graphene and pre-hierarchical graphene. Hydrogen adsorption and desorption isotherms of the hierarchical graphene and pre-hierarchial graphene, (c) Isosteric heat of hydrogen sorption. and (d) Physisorption hydrogen storage capacity comparison between the hierarchical graphene and various carbon materials. (From Guo et al., 2013 [94], with permission).*
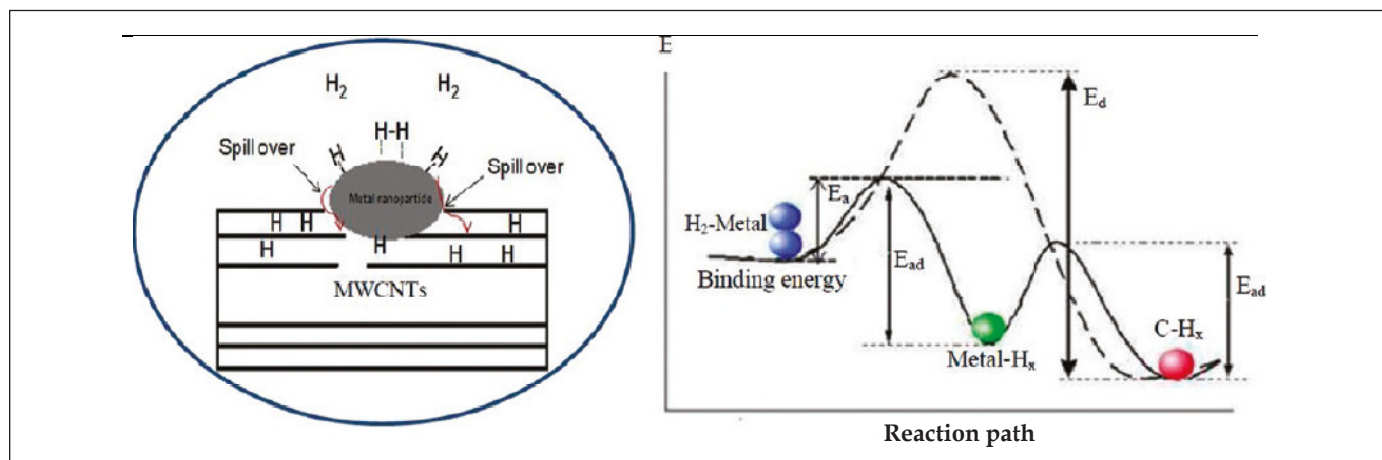
Fig. 16: *Mechanism of hydrogen adsorption in a metal decorated multiwalled carbon nanotube through molecular hydrogen dissociation into atoms at metal surface and M-C-H_x complex formation (From Reyhani et al., 2011 [122], with permission.)*

Improvement in storage capacity through decoration is through either Kubas interaction or dissociation of H_2 molecules on the metal particles, i.e., spillover. Pd is found to be most effective catalyst for H_2 storage process. Dissociation of H_2 occurs on the Pd particle, and H_2 atoms are entered into the spaces between adjacent carbon layers. They create loosely bonds of CH_x species and Pd-C-H_x complex which can be decomposed easily at lower temperatures as compared to C-H chemical bonds (Fig. 16).

Wang et al. [123] concluded upon detailed analysis of H_2 isotherms and isosteric heat of adsorption, that doping with an appropriate amount of Ni–B nanoalloys can cause dissociative chemisorption of H_2 molecules by spillover to achieve hydrogen storage capacity (> 4 wt %). This can be three times higher than its pristine counterpart (Fig. 17).

Table 4 A versions of remarkable experimental works for measuring H₂ storage in pure CNMs [95-119]

Carbon nanomaterial type	Storage condition		Hydrogen storage capacity (wt %)	Remarks	**Reference**
	Temperature	**Pressure**			
Graphite	773 K	3.5 MPa	1.6		[95]
	77 K	20 bar	1.2	Exfoliated graphite	[96]
Graphene	300 K	1 MPa	7.4		[97]
Activated carbon	293 K	3 MPa	0.39–0.53		[98]
Activated carbon fiber	298 K	10 MPa	2.29		[99]
Carbon nanotube	Ambient	0.067 MPa	3.5–4.5	High purity single walled	[100]
	Ambient	4.8 MPa	1.2	Purified SW	[101]
	Ambient	0.9 MPa	0	Ball-milled SW	[102]
	80 K	~7 MPa	8.25	High purity SW	[103]
	295 K	0.1 MPa	0.93	Impure SW	[104]
	~300–700 K	Ambient	0.25	Purified MW	[105]
	300 K	1.0 MPa	13.8	Acid treated MW	[106]
	298 K	3.6 MPa	0.03	Low purity MER MW	[107]
	298 K	10 MPa	0.68	Random orientation MW	[108]
Nanoporous carbon material	Ambient	207 bar	8.13	Valid for a pore density of 1 cm³/g and size of 0.9 Å	[109]
Carbon nanofiber	77–300 K	1.5 MPa	1–1.8	Purified GNF herringbone	[110]
	77 K	12 MPa	12.38	CNF	[111]
	93 K	10 MPa	1	CNF	[112]
	298 K	3.6 MPa	<0.1	Vapor grown	[107]
Ordered mesoporous carbon	298 K	30 MPa	2.14		[113]
Templated carbon	298 K	10 MPa	1.43		[114]
Carbon xerogel	298 K	20	1.0		[115]
Carbon sphere	298 K	9	0.25-0.43		[116]
Carbon nanosheet	298 K	0.11	0.1-0.26		[117]
Carbon cloth	298 K	90 bar	0.5		[118]

Table 5 Hydrogen storage performance of functionalized CNMs experimentally observed by researchers worldwide [89, 91, 125-141]

| Carbon nanomaterial type	Storage condition			Hydrogen storage capacity (wt %)	Remarks	Reference
	Temperature	Pressure	Decorating element			
Graphene	77 K	Ambient	Zirconia	1.2	Reduced GO	[125]
	298 K	4 MPa	Pt and N	4.4		[89]
	298 K	100 bar	P	2.2		[126]
	298 K	3 MPa	Pt	1.4		[127]
	298 K	30 bar	Pd3Co	4.6	boron doped	[128]
Carbon nanotube	473–673 K	0.1 MPa	Li	20		[129]
	<313 K	0.1 MPa	K	21	Wet H_2	[130]
	473–663	0.1 MPa	Li	0.7–4.2	10–40% pure	[131]
	Ambient	0.067 MPa	Ti-Al-V	6	Sonicated	[132]
	Ambient	0.08 MPa	Fe	<0.005	Purified	[91]
	298 K	15.85 atm	Ni	0.812	multiwalled	[133]
		12.64 atm	Cu	2.59		
		15.45atm	Agglomerated Fe	0.909		
	298 K	32 bar	Pd, N	1.25	Graphene Nanoplatelets	[134]
	283-335 K	Ambient	Ca	1.05	Multiwalled	[135]
			Co	1.51		
			Fe	0.75		
			Ni	0.4		
			Pd	7		
	Ambient	80 bar	B	<2		[136]
	Moderate	Ambient	K	4.47		[137]
Carbon nanofiber	298	50 bar	Ni	0.56	decorated CNF grown on ACF substrate	[138]
Porous carbon	298 K	100 bar	P	1.2		[139]
Graphitic carbon nitride	298 K	4 MPa	Pd	2.6		[140]
Superactived carbon	298 K	10 MPa	Pt	1.46		[141]
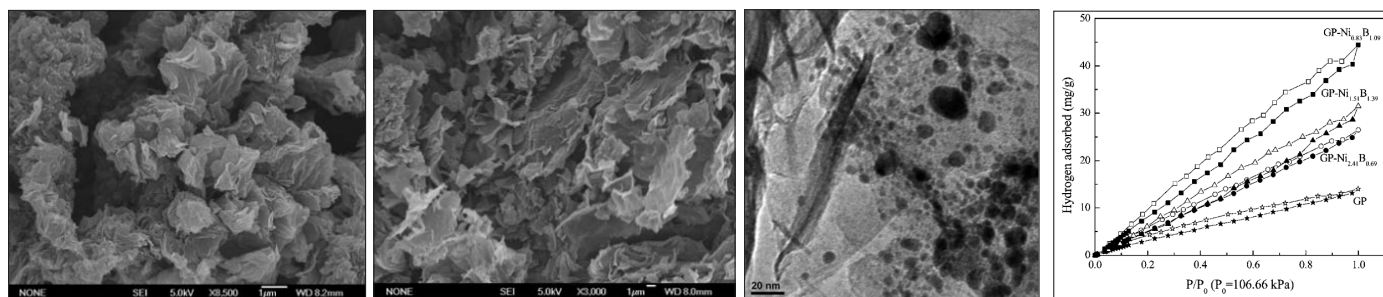
***Fig. 17:** SEM images of GP (a) pristine graphene (GP) and (b) GP-Ni$_{0.83}$B$_{1.09}$, (c) TEM image of GP-Ni$_{0.83}$B$_{1.09}$, and (d) H$_2$ adsorption and desorption isotherms of GP, GP-Ni$_{2.41}$B$_{0.69}$, GP-Ni$_{1.51}$B$_{1.39}$ and GP-Ni$_{0.83}$B$_{1.09}$ at 77 K (adsorption data are shown as closed shapes, desorption data as open shapes). (From Wang et al., 2011 [123], with permission.)*
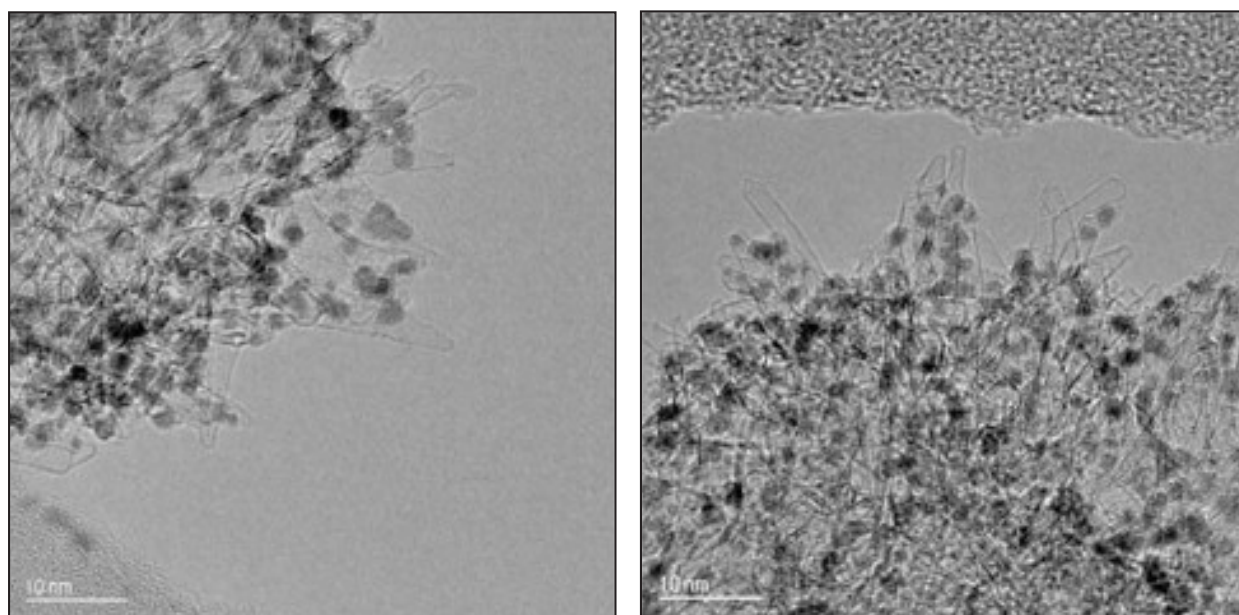
(a)
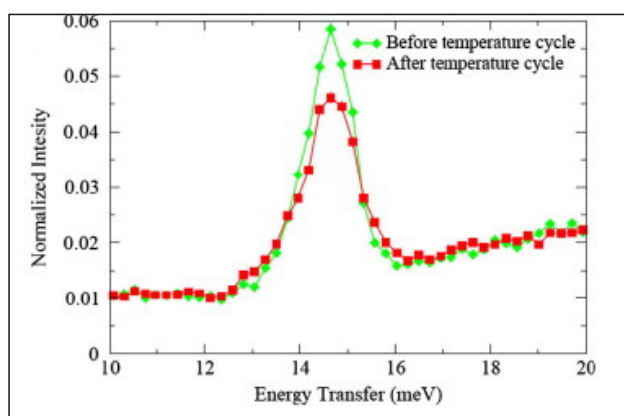
(b)
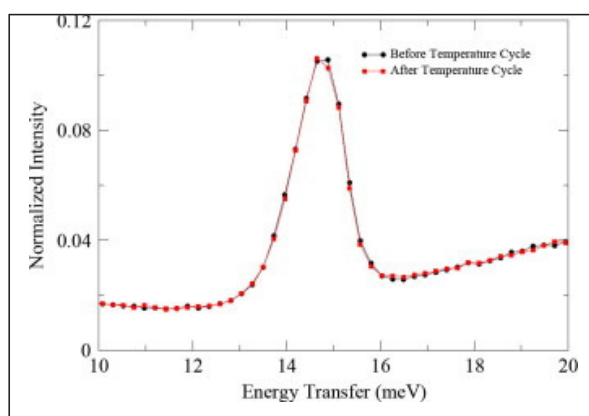
(c)

***Fig. 18:** (a) TEM images of oxidized, Pt-decorated single wall carbon nanohorns. (b) Experimental INS data of 1% mass fraction H2 on Pt-SWCNHs before (solid circles) and after (solid squares) cycling the temperature of the closed system to 295 K. (c) Experimental INS data of 1% mass fraction H$_2$ on Pt-SWCNHs before (black circles) and after (red squares) cycling the temperature of the closed system to 150 K. All measurements were taken at 4 K. (From Liu et al., 2012 [124], with permission.)*

A novel inelastic neutron scattering based hydrogen quantification method has been developed by Liu et al [124] to find advantage over traditional Sievert type measurement. The developed method involves temperature-cycling. Measurements on single-wall carbon nanohorns (SWCNHs) decorated with 2–3 nm Pt nanoparticles showed 0.17% mass fraction of metal-assisted H_2 storage (at ≈0.5 MPa) at room temperature. When measured using Sievert's apparatus, a hydrogen adsorption of ≈0.08% mass fraction at 5 MPa at room temperature is achieved. The obtained excess storage ranging 0.3-0.5 wt % is believed to be attributed to metal-assisted H_2 spillover (Fig. 18).

A few more important observational efforts are tabulated (Table 5) [89, 91, 125-141] concerning experimental studies for evaluating actual H_2 storage capacity of various decorated CNMs. Compared to graphene and other minor derivatives such as CNF, porous carbon etc., decorated CNT appears to demonstrate superior H_2 storage performance in a few instances [130-131, 133, 139]. However, that trend is not reproducible by all observers [92, 135-136, 138] due to various issues described in section 3.1.

3.3 Challenges and issues in experimental studies

Tonnage scale commercial production of carbonaceous nanomaterials is till date unachieved for difficulty in scaling up of laboratory findings. With progress of technology, it is anticipated to be realized in coming time. Once that is done, demand of such material for various applications including H_2 storage is bound to grow. Industrial use of nanomaterials faces many obstacles as there is no suitable regulatory framework and guidance on safety requirements; specific provisions have yet to be established worldwide. Moreover, regulations related to the right of intellectual properties as well as the absence of an appropriate framework for patent registration are issues delaying the process of products' industrial application. However, utilization of high-quality nanomaterials is now growing and coming to the industrial arena rendering them as the next generation attractive resources with promising applications. Especially, as on today's date, industrial scale synthesis of CNMs carries in environmental hazards in terms of generation and proliferation of many kinds of toxicity into atmosphere. In addition to that, for chemically functionalized CNMs with transition metal (TM) decoration, structural stability in TM dispersions remains a large challenge, as metal atoms tend to aggregate because of strong metal cohesion forces. As can be realized from above, suitable doping is inevitable for efficient storage at ambiance, more technical progress in necessary for

overcoming obstacles like oxidation or oxygen interference, clustering etc. of the decorating substance.

4. Conclusions and future direction

Carbonaceous nanomaterials constitute an important category of candidates for solid-state H_2 storage for on-board application. Although storage performance of pure CNMs are practically not that promising at near-ambient conditions, theoretically it has been proved reproducibly that functionalized CNMs are capable of storing greater quantum of H_2 satisfying DoE requirements even at ambient condition. However, actual technical barrier of properly decorating CNMs with transition metal nanoparticles is not yet greatly successful for want of suitably optimized methods. Secondly, experimental scattering till date prevails for practical limitations and thus development of such substance is still ongoing. In future, with technological improvement, this can be one of the possible options for switching to greener energy alternatives.

References

1. J. D. Holladay, J. Hu, D. L. King and Y. Wang, Catalysis Today 139 (2009) 244.

2. D. Mori and K. Hirose, International Journal of Hydrogen Energy 34 (2009) 4569.

3. M. S. Sadaghiani and M. Mehrpooya, International Journal of Hydrogen Energy 42 (2017) 6033.

4. M. Felderhoff, C. Weidenthaler, R. von Helmolt and U. Eberle, Physical Chemistry Chemical Physics 9 (2007) 2643.

5. J. Graetz, Chemical Society Reviews 38 (2009) 73.

6. https://www.energy.gov/eere/fuelcells/doe-technical-targets-onboard-hydrogen-storage-light-duty-vehicles

7. G. Sandrock, Journal of alloys and compounds 293 (1999) 877.

8. B. Sakintuna, F. Lamari-Darkrim and M. Hirscher, International Journal of Hydrogen Energy 32 (2007) 1121.

9. J. Weitkamp, M. Fritz and S. Ernst, Proceedings from the ninth international zeolite conference Butterworth-Heinemann (1993) 11.

10. B. Peng and J. Chen, Energy & Environmental Science 1 (2008) 479.

11. E. I. Shkolnikov, A. Z. Zhuk and M. S. Vlaskin, Renewable and Sustainable Energy Reviews 15 (2011) 4611.

12. N. L. Rosi, J. Eckert, M. Eddaoudi, D.T. Vodak, J. Kim, M. O'Keeffe and O. M. Yaghi, Science 300 (2003) 1127.

13. S. S. Han, H. Furukawa, O. M. Yaghi and W. A. Goddard III, Journal of the American Chemical Society 130 (2008) 11580.

14. D. Ramimoghadam, E. M. Gray and C. J. Webb, International Journal of Hydrogen Energy 41 (2016) 16944.

15. M. Benelmekki, Nanomaterials: The Original Product of Nanotechnology Morgan & Claypool Publishers (2019).

16. T. D. Burchell ed., Carbon materials for advanced technologies Elsevier (1999).

17. J. Hafner, Journal of computational chemistry 29 (2008) 2044.

18. P. Giannozzi, S. Baroni, N. Bonini, M. Calandra, R. Car, C. Cavazzoni, D. Ceresoli, G. L. Chiarotti, M. Cococcioni, I. Dabo and A. Dal Corso, Journal of physics: Condensed matter 21 (2009) 395502.

19. P. Blaha, K. Schwarz, G.K. Madsen, D. Kvasnicka and J. Luitz, InstitutFürPhysikalische und TheoretischeChemie Wien Austria (2001).

20. P. A. Cahill and C. M. Rohlfing, Tetrahedron 52 (1996) 5247.

21. D. Henwood and J. D. Carey, Physical Review B 75 (2007) 245413.

22. G. J. Kubas, Journal of Organometallic Chemistry 635 (2001) 37.

23. G. J. Kubas, Journal of Organometallic Chemistry 694 (2009) 2648.

24. R. M. Martin and R. M. Martin, Electronic Structure: Basic Theory and Practical Methods Cambridge University Press (2004).

25. K. Capelle, Brazilian Journal of Physics 36 (2006) 1318.

26. N. Argaman and G. Makov, American Journal of Physics 68 (2000) 69.

27. W. M. C. Foulkes, L. Mitas, R. J. Needs and G. Rajagopal, Reviews of Modern Physics 73 (2001) 33.

28. B. L. Hammond, W. A. Lester and P. J. Reynolds, Monte Carlo methods in ab initio quantum chemistry World Scientific 1 (1994).

29. J. Kolorenč and L. Mitas, Reports on Progress in Physics 74 (2011) 026502.

30. I. Mayer, Simple theorems, proofs, and derivations in quantum chemistry Springer Science & Business Media (2013).

31. J. Thijssen, Computational Physics Cambridge University Press (2007).

32. C. D. Sherrill and H. F. Schaefer III, Advances in quantum chemistry 34 (1999) 143.

33. I. Shavitt and R. J. Bartlett. Many-body methods in chemistry and physics: MBPT and coupled-cluster theory Cambridge University Press (2009).

34. B. Jeziorski and H. J. Monkhorst, Physical Review A 24 (1981) 1668.

35. P. Hohenberg and W. Kohn, Physical review 136 (1964) B864.

36. W. Kohn and L. J. Sham, Physical review 140 (1965) A1133.

37. D. M. Ceperley and B. J. Alder, Physical Review Letters 45 (1980) 566.

38. J. P. Perdew, K. Burke and M. Ernzerhof, Physical Review Letters 77 (1996) 3865.

39. B. Han, P. H. Lv, W. F. Sun and S. W. Song, Crystals 9 (2019) 397.

40. H. Nishihara, Q.H. Yang, P.X. Hou, M. Unno, S. Yamauchi, R. Saito, J.I. Paredes, A. Martínez-Alonso, J.M. Tascón, Y. Sato and M. Terauchi, Carbon 47 (2009) 1220.

41. M. D. Ganji, S. M. Hosseini-Khah and Z. Amini-Tabar, Physical Chemistry Chemical Physics 17 (2015) 2504.

42. G. Henkelman, A. Arnaldsson and H. Jónsson, Computational Materials Science 36 (2006) 354.

43. R. S. Mulliken, Journal of Chemical Physics 23 (1955) 1833.

44. A. Kokalj, Journal of applied crystallography 44 (1999) 176.

45. K. Momma and F. Izumi, Journal of applied crystallography 44 (2011) 1272.

46. J. Wong, S. Yadav, J. Tam and C. Veer Singh, Journal of Applied Physics 115 (2014) 224301.

47. S. Grimme, Journal of computational chemistry 27 (2006) 1787.

48. K. Lee, É. D. Murray, L. Kong, B. I. Lundqvist and D. C. Langreth, Physical Review B 82 (2010) 081101.

49. J. Klimeš, D. R. Bowler and A. Michaelides, Condensed Matter 22 (2009) 022201.

50. J. Klimeš, D. R. Bowler and A. Michaelides, Physical Review B 83 (2011) 195131.

51. S. M. Lee, K. H. An, Y. H. Lee, G. Seifert and T. Frauenheim, Journal of the American Chemical Society 123 (2001) 5059.

52. G. E. Froudakis, Journal of physics: condensed matter 14 (2002) R453.

53. M. Yoon, S. Yang, E. Wang and Z. Zhang, Nano Letters 7 (2007) 2578.

54. V. Tozzini and V. Pellegrini, The Journal of Physical Chemistry C 115 (2011) 25523.

55. O. V. Pupysheva, A. A. Farajian and B. I. Yakobson, Nano Letters 8 (2007) 767.

56. A. Kuc, L. Zhechkov, S. Patchkovskii, G. Seifert and T. Heine, Nano letters 7 (2007) 1.

57. Y. Lin, F. Ding and B. I. Yakobson, Physical Review B 78 (2008) 041402.

58. Q. Wang and J. K. Johnson, Physical Chemistry B 103 (1999) 4809.

59. M. Rzepka, P. Lamp and M. A. De la Casa-Lillo, The Journal of Physical Chemistry B 102 (1998) 10894.

60. P. Kowalczyk, R. Hołyst, M. Terrones and H. Terrones, Physical Chemistry Chemical Physics 9 (2007) 1786.

61. G. Mpourmpakis, E. Tylianakis and G. E. Froudakis, Nano letters 7 (2007) 1893.

62. Gao, Yan, Huanian Zhang, Hongzhe Pan, Qingfang Li, and Jijun Zhao. "Ultrahigh hydrogen storage capacity of holey graphyne." Nanotechnology 32, no. 21 (2021): 215402.

63. A. Gangan, B. Chakraborty, L. M. Ramaniah and S. Banerjee, International Journal of Hydrogen Energy 44 (2019) 16735.

64. B. Chakraborty, P. Modak and S. Banerjee, The Journal of Physical Chemistry C 116 (2012) 22502.

65. A. Yadav, B. Chakraborty, A. Gangan, N. Patel, M. R. Press

and L. M. Ramaniah, The Journal of Physical Chemistry C 121 (2017) 16721.

66. M. Yoon, S. Yang, C. Hicke, E. Wang, D. Geohegan and Z. Zhang, Physical review letters 100 (2008) 206806.

67. T. Yildirim and S. Ciraci, Physical review letters 94 (2005) 175501.

68. E. Tylianakis, G. M. Psofogiannakis and G. E. Froudakis, The Journal of Physical Chemistry Letters 1 (2010) 2459.

69. H. Lee, J. Ihm, M. L. Cohen and S. G. Louie, Nano Letters 10 (2010) 793.

70. W. Q. Deng, X. Xu and W. A. Goddard, Physical Review Letters 92 (2004) 166103.

71. C. Ataca, E. Aktürk, S. Ciraci and H. Ustunel, Applied Physics Letters 93 (2008) 043123.

72. Z. M. Ao and F. M. Peeters, Physical Review B 81 (2010) 205406.

73. J. H. Cho and C. R. Park, Catalysis Today 120 (2007) 407.

74. J. H. Cho, S. J. Yang, K. Lee and C. R. Park, International Journal of Hydrogen Energy 36 (2011) 12286.

75. H. J. Hwang, Y. Kwon and H. Lee, The Journal of Physical Chemistry C 116 (2012) 20220.

76. Deniz, Celal Utku, Humeyra Mert, and Cengiz Baykasoglu. "Li-doped fullerene pillared graphene nanocomposites for enhancing hydrogen storage: A computational study." Computational Materials Science 186 (2021): 110023.

77. A. Sigal, M. Villarreal, M. I. Rojas and E. P. M. Leiva, International Journal of Hydrogen Energy 39 (2014) 5899.

78. T. Das, S. Banerjee and V. Sudarsan, AIP Conference Proceedings 1665 (2015) 050106.

79. T. K. Das, S. Banerjee, M. Pandey, B.Vishwanadh, R. J. Kshirsagar and V. Sudarsan, International Journal of Hydrogen Energy 42 (2017) 8032.

80. S. K. Das, S. C. Sahu, A. Ghosh, S. Basu, B. Chakraborty and B. K. Jena, Carbon 149 (2019) 307.

81. J. Prakash, B. M. Tripathi, K. Dasgupta, J. K. Chakravartty, M. R. Pai, A. Kumar and S. R. Bharadwaj, Current Nanomaterials 1 (2016) 124.

82. S. Banerjee, K. Dasgupta, A. Kumar, P. Ruz, B. Vishwanadh, J. B. Joshi and V. Sudarsan, International Journal of Hydrogen Energy 40 (2015) 3268.

83. S. V. Sawant, , S. Banerjee, A. W. Patwardhan, J. B. Joshi and K. Dasgupta, International Journal of Hydrogen Energy 44 (2019) 18193.

84. A. Sharma, K. Dasgupta, A. Patwardhan and J. Joshi, Chemical Engineering Science 170 (2017) 756.

85. A. Sharma, A. Patwardhan, K. Dasgupta and J. B. Joshi, Chemical Engineering Science 207 (2019) 1341.

86. D. Bera, S.C. Kuiry, M. McCutchen, A. Kruize, H. Heinrich, M. Meyyappan and S. Seal, Chemical physics letters 386 (2004) 364.

87. G. L. Tian, M. Q. Zhao, D. Yu, X. Y. Kong, J. Q. Huang, Q. Zhang and F. Wei, Small 10 (2014) 2251.

88. C. C. Huang, N. W. Pu, C. A. Wang, J. C. Huang, Y. Sung and M. D. Ger, Separation and Purification Technology 82 (2011) 210.

89. V. B. Parambhath, R. Nagar and S. Ramaprabhu, Langmuir 28 (2012) 7826.

90. Y. Sun and P. A. Webley, Chemical Engineering Journal 162 (2010) 883.

91. M. Hirscher, M. Becher, M. Haluska, F. von Zeppelin, X. Chen, U. Dettlaff-Weglikowska and S. Roth, Journal of Alloys and Compounds 356 (2003) 433.

92. Y. Chen, D. T. Shaw, X. D. Bai, E. G. Wang, C. Lund, W. M. Lu and D. D. L. Chung, Applied physics letters 78 (2001) 2128.

93. A. D. Lueking, L. Pan, D. L. Narayanan and C. E. Clifford, The Journal of Physical Chemistry B 109 (2005) 12710.

94. C. X. Guo, Y. Wang and C. M. Li, ACS Sustainable Chemistry & Engineering 1 (2013) 14.

95. Z. Y. Zhong, Z. T. Xiong, L. F. Sun, J. Z. Luo, P. Chen, X. Wu, J. Lin and K. L. Tan, The Journal of Physical Chemistry B 106 (2002) 9507.

96. A. D. Lueking, L. Pan, D. L. Narayanan and C. E. Clifford, The Journal of Physical Chemistry B 109 (2005) 12710.

97. S. Orimo, G. Majer, T. Fukunaga, A. Züttel, L. Schlapbach and H. Fujii, Applied Physics Letters 75 (1999) 3093.

98. M. Zieliński, R. Wojcieszak, S. Monteverdi, M. Mercy and M. M. Bettahar, Catalysis Communications 6 (2005) 777.

99. J. S. Im, S. J. Park, T. Kim and Y. S. Lee, International Journal of Hydrogen Energy 34 (2009) 3382.

100. C. Liu, Y. Y. Fan, M. Liu, H. T. Cong, H. M. Cheng and M. S. Dresselhaus, Science 286 (1999) 1127.

101. M. R. Smith, E. W. Bittner, W. Shi, J. K. Johnson and B. C. Bockrath, The Journal of Physical Chemistry B 107 (2003) 3752.

102. M. Hirscher, M. Becher, M. Haluska, U. Dettlaff-Weglikowska, A.Quintel, G. S. Duesberg, Y. M. Choi, P. Downes, M. Hulman, S. Roth and I. Stepanek, Applied Physics A 72 (2001) 129.

103. Y. Ye, C. C. Ahn, C. Witham, B. Fultz, J. Liu, A. G. Rinzler, D. Colbert, K. A. Smith and R. E. Smalley, Applied Physics Letters 74 (1999) 2307.

104. N. Nishimiya, K. Ishigaki, H. Takikawa, M. Ikeda, Y. Hibi, T. Sakakibara, A. Matsumoto and K. Tsutsumi, Journal of Alloys and Compounds 339 (2002) 275.

105. X. B. Wu, P. Chen, J. Lin and K. L. Tan, International Journal of Hydrogen Energy 25 (2000) 261.

106. Y. Chen, D. T. Shaw, X.D. Bai, E. G. Wang, C. Lund, W. M. Lu and D. D. L. Chung, Applied physics letters 78 (2001) 2128.

107. G. G. Tibbets, G. P. Meisner and C. H. Olk, Carbon 39 (2001) 2291.

108. H. Zhu, A. Cao, X. Li, C. Xu, Z. Mao, D. Ruan, J. Liang and D. Wu, Applied Surface Science 178 (2001) 50.

109. N. C. Gallego, L. He, D. Saha, C. I. Contescu and Y. B. Melnichenko, American Chemical Society 133 (2011) 13794.

110. A. Chambers, C. Park, R. T. K. Baker and N. M. Rodriguez, The Journal of Physical Chemistry B 102 (1998) 4253.

111. Y. Y. Fan, B. Liao, M. Liu, Y. L. Wei, M. Q. Lu and H. M. Cheng, Carbon 10 (1999) 1649.

112. M. A. De la Casa-Lillo, F. Lamari-Darkrim, D. Cazorla-Amoros and A. Linares-Solano, The Journal of Physical Chemistry B 106 (2002) 10930.

113. D. Saha and S. Deng, Langmuir 25 (2009) 12550.

114. L. Wang and R. T. Yang, The Journal of Physical Chemistry C 112 (2008) 12486.

115. L. Zubizarreta, J. A. Menéndez, N. Job, J. P. Marco-Lozar, J. P. Pirard, J. J. Pis, , A. Linares-Solano, D. Cazorla-Amorós and A. Arenillas, Carbon 48 (2010) 2722.

116. L. Zubizarreta, J. A. Menéndez, J. J. Pis and A. Arenillas, International Journal of Hydrogen Energy 34 (2009) 3070.

117. Z. L. Hu, M. Aizawa, , Z. M. Wang, N. Yoshizawa and H. Hatori, Langmuir 26 (2010) 6681.

118. L. Zubizarreta, A. Arenillas and J. J. Pis, International Journal of Hydrogen Energy 34 (2009) 4575.

119. F. Jokar, D. D. Nguyen, M. Pourkhalil and V. Pirouzfar, Chemical Engineering Technology 44 (2021) 387.

120. R. Ströbel, J. Garche, P.T. Moseley, L. Jörissen and G. Wolf, Journal of power sources 159 (2006) 781.

121. H. M. Cheng, Q. H. Yang, and C. Liu Carbon 39 (2001) 1447.

122. A. Reyhani, S. Z. Mortazavi, S. Mirershadi, A. Z. Moshfegh, P. Parvin and A. N. Golikand, The Journal of Physical Chemistry C (2011) 6994.

123. Y. Wang, C. X. Guo, X. Wang, C. Guan, H. Yang, K. Wang and C. M. Li, Energy & Environmental Science 4 (2011) 195.

124. Y. Liu, C. M. Brown, D. A. Neumann, D. B. Geohegan, A. A. Puretzky, C. M. Rouleau, H. Hu, D. Styers-Barnett, P. O. Krasnov and B. I. Yakobson, Carbon 50 (2012) 4953.

125. M. Kaur, and K. Pal, International Journal of Hydrogen Energy 41 (2016) 21861.

126. A. Ariharan, B.Viswanathan and V. Nandhakumar,. Graphene 5 (2016) 39.

127. P. Divya and S. Ramaprabhu, Physical Chemistry Chemical Physics 16 (2014) 26725.

128. S. S. Samantaray, V. Sangeetha, S. Abinaya and S. Ramaprabhu, International Journal of Hydrogen Energy 43 (2018) 8018.

129. P. Chen, X. Wu, J. Lin and K. L. Tan, Science 285 (1999) 91.

130. R. T. Yang, Carbon 38 (2000) 623.

131. F. E. Pinkerton, B. G. Wicke, C. H. Olk, G. G. Tibbetts, G. P. Meisner, M. S. Meyer and J. F. Herbst, The Journal of Physical Chemistry B 104 (2000) 9460.

132. A. C. Dillon, T. Gennet, J. L. Alleman, K. M. Jones, P. A. Parilla and M. J. Heben, DOE Hydrogen Program Progress Report (1999).

133. V. Fierro, A. Szczurek, C. Zlotea, J.F. Mareche, M.T. Izquierdo, A. Albiniak, M. Latroche, G. Furdin and A. Celzard, Carbon 48 (2010) 1902.

134. B. P. Vinayan, K. Sethupathi and S. Ramaprabhu, Journal of Nanoscience and Nanotechnology 12 (2012) 6608.

135. A. Reyhani, S. Z. Mortazavi, S. Mirershadi, A. Z. Moshfegh, P. Parvin and A.N. Golikand, The Journal of Physical Chemistry C 115 (2011) 6994.

136. M. Sankaran and B. Viswanathan, Carbon 45 (2007) 1628.

137. C. H. Chen and C. C. Huang, International Journal of Hydrogen Energy 32 (2007) 237.

138. A. Yadav, M. Faisal, A. Subramaniam and N. Verma, International Journal of Hydrogen Energy 42 (2017) 6104.

139. A. Ariharan, B. Viswanathan and V. Nandhakumar, Indian Journal of Chemistry 55 (2016) 649.

140. A. A. Nair, R. Sundara and N. Anitha, International Journal of Hydrogen Energy 40 (2015) 3259.

141. Z. Wang and R. T. Yang, The Journal of Physical Chemistry C 114 (2010) 5956.

Mr. Gopal Sanyal *is a Research Scientist at the Mechanical Metallurgy Division, Bhabha Atomic Research Centre, Trombay, Mumbai 400085, India. He earned a Master of Technology in Metallurgical and Materials Engineering from IIT Kharagpur in 2007. His primary research interest is in the evaluation of the mechanical properties of materials.*

Dr. Brahmananda Chakraborty *is an Associate Professor at the Homi Bhabha National institute, Mumbai and Scientist in High Pressure & Synchrotron Radiation Physics Division of Bhabha Atomic Research Centre, Mumbai. He received his PhD degree in Physics from IIT, Bombay for his research topic on 'Irradiation Effects and Hydrogen Storage on Carbon Nanotubes' under the guidance of Dr. Srikumar Banerjee and Prof. D.S. Misra. Dr Chakraborty did two years (2010–2012) Post-doctoral research at North Carolina State University, USA. His current research interest includes Density Functional Theory (DFT) and Molecular Dynamics (MD) simulations for energy materials, bio-sensors, reactor fuels and structural materials, various 2D materials for energy storage devices and the behavior of materials under high pressure. He received International Association of Advanced Material (IAAM) Scientist Medal in 2017. He has very good experience of teaching while teaching Density Functional Theory at North Carolina State University, USA and Computational Physics and Statistical Physics at BARC Training School. He has more than 80 publications in reputed international journals. Dr. Chakraborty is also a regular reviewer in reputed international journals like Journal of Physical Chemistry, CARBON, Physical Chemistry Chemical Physics, Journal of Applied Physics etc. Dr. Chakraborty has also contributed in Department of Atomic Energy's Nuclear Programme in physics designing of various reactors using Monte Carlo Simulations for neutron transport.*

Study of vertical graphene-nanodiamond hybrid structure grown by thermally activated chemical vapor deposition

Dipti Ranjan Mohapatra
Department of Physics, Vikram Deb (A) College, Jeypore, Koraput, Odisha-764001
E-mail: dipti.mohapatra81@gmail.com

Abstract

The report is based on a non-catalytic direct growth of few layered vertical graphene (FLVG)-nanodiamond hybrid structure using a thermally activated hot filament CVD technique. The cross-sectional microstructural analysis of the film–substrate interface revealed the exact steps involved for the structural transformation of graphene from the planar structure into the two-dimensional vertical structure. The results suggest that the formation of vertical graphene is possible only by the addition of nitrogen gas into the precursor gas-mixture. The possible mechanisms for the onset of vertical growth of FLVG structure in a thermally activated medium are discussed.

Keywords: Graphene, vertical structure, nanodiamond, thermal activation, non-catalytic

1 Introduction

Carbon nanomaterials in its various forms have drawn significant interest in the field of nanoscience and nanotechnology because of their extraordinary mechanical, electrical and optical properties. The C-C sp^3 network of diamond nanostructure is known to be an excellent material for various applications [1-6]. The newly born graphene, a two-dimensional sheet of hexagonally arranged sp^2-bonded carbon form, has exhibited wide range of superior properties as compared to its counterparts, and thus considered to be a potential material for the advanced technology [7-10]. However, the planar structure of graphene with respect to the flat substrates limits its true potential. The effective surface area of planar structured graphene is comparatively smaller than its vertical structure (bottom surface of graphene is inactivated by the presence of substrate). The field emission property of planar graphene is limited by its in-plane shape, whereas vertical graphene is more potential for this purpose. As compared to the nearly in-active basal plane the edge plane of vertically graphene is highly reactive, and thus considered to be an excellent electrode material for electro-catalysis applications [11]. In addition, large surface area of vertical graphene is favorable for the fabrication of various nanostructured materials, biosensors, and electrodes for batteries or capacitors [12-14]. Nonocrystalline diamond films are very promising nanostructured carbon materials owing to their unique physical properties [1-6]. Hence, the diverse properties of graphene and nanodiamond could be combined together in order to open an avenue for the unexplored basic science and emerging technology. Recently, Yu et al. [15] have used nanodiamond – graphene hybrid structure as a filler material for the enhancement of thermal conductivity of Poly (vinylidene fluoride) (PVDF) composites in order to increase the heat dissipation for the electronic devices.

Few layered vertical graphene (FLVG), commonly termed as carbon nanowall (CNW), have been achieved on both catalyzed [16] and non-catalyzed [17] substrates using various plasma-assisted CVD techniques. It has been shown that vertical growth of carbon nanowalls using plasma assisted CVD techniques is due to the aligned electric field caused by the plasma and highly dense carbon-based ionic species [16-24]. However, plasma-assisted CVD synthesized carbon nanomaterials materials are always limited to a small area (restricted by plasma size) and prone to contain large amount of defects due to the ion bombardment from the high density plasma. On the other hand, thermally assisted hot filament CVD (HFCVD) technique offers large area and defect free growth of carbon nanomaterials. Nonetheless, very limited literatures exist on the growth of FLVG/CNW using HFCVD technique [25-27]. Recently, carbon nanotubes [28] and carbon papers [29] have been used as templates to grow carbon nanowall using HFCVD technique. The vertical growth of graphene/carbon nanowall has been achieved either by using plasma assisted discharge technique or specially treated substrates (substrate biasing /metal catalyzed substrate). The catalyst-free vertical growth of FLVG using HFCVD technique is very rare and far from clear understanding. In addition, a non-catalytic direct growth of graphene on a semiconducting or dielectric substrate is extremely challenging and advantageous for the electronic device applications. The mechanism for vertical growth of graphene along a two-dimensional vertical plane, rather than the expected one-dimensional vertical plane (in form of vertical wire/rod structure) is still open and need to be understood.

In this work, we report a simple method for the growth of FLVG and nanodiamond composite using a single-step HFCVD technique without using any metal catalysts/ substrate biasing or any other special instrumental arrangements. The onsets of vertical growth of FLVGs have been analyzed carefully using a cross-sectional HRTEM analysis and their possible growth mechanisms are discussed.

2. Experimental details

The vertical graphene films were synthesized on Si substrate using HFCVD technique. The details of the HFCVD chamber are given in [28]. The reaction chamber was initially evacuated to a pressure 3×10^{-3} Torr, and subsequently a gas mixture of 2% CH_4 and 15% nitrogen in H_2/Ar mixture was introduced to the chamber, while keeping total flow rate of the gas-mixture constant at 100 SCCM (SCCM denotes cubic centimeter per minute at STP). The filament temperature was slowly increased from room temperature to the predetermined growth temperature by varying the alternating current (AC) source. The desired substrate temperature 750 °C was achieved by keeping the filament temperature at 2200°C. The synthesis was carried out at a chamber pressure 7.5 Torr. The substrate temperature was measured by a thermocouple (Pt–Rh) put in contact with the substrate surface, while the filament temperature was measured by an optical pyrometer (Minolta TR 630 A, with the emissivity adjusted to that of the tungsten ~ 0.33 [28]. The microstructural analysis of the grown films were carried out by high resolution scanning electron microscopy (HR-SEM, FEI Nova Nano SEM 200), Raman spectroscopy (Jobin Yvon model T64000, wavelength of the laser: 514.5 nm), high resolution transmission electron microscopy (HR-TEM, FEI Titan, operating voltage: 300 kV), and X-ray photoelectron spectroscopy (XPS, ESCA PHI 5800: using Al Ka source). The sample for TEM analysis was prepared by focused ion beam (FIB, FEI Nova 600) for thinning it, and then mounted on a platinum-coated TEM grid.

3. Results and discussion

Fig. 1 shows the low and high-resolution SEM (HR-SEM) micrographs of the FLVG/CNW samples grown at a substrate temperature of 750°C using CH_4/H_2/Ar/ N_2 mixture. The morphology of the samples exhibits a uniform coating of flake-like nanostructures standing vertically on to the substrate surface with lots of open space in between them. The HRSEM image of the sample grown for 10 minutes (Fig. 1b) shows that some of the flakes are grown relatively faster than the others and have popped out of the film matrix flaunting their sharp edges. As the growth further increased to 30 minutes, the surface morphology of the FLVG film (Fig. 1c and d) shows an increase in the density of flakes at a uniform height. The overall inter connectivity of the individual nanoflakes increases, albeit, they are randomly oriented with respect to each other.

The surface morphology of the current FLVG film shows that the graphene flakes are sheet-like structured, spreading only two-dimensionally (can be envisioned as a portion of the petal-like structure sliced from the middle), whereas in case of a petal/cone-like structured nanoflakes, the edge of the walls are usually connected around all the directions forming a 3D structure. The flakes are laterally compressed by other flakes during their vertical growth and thus curled in lateral direction. This
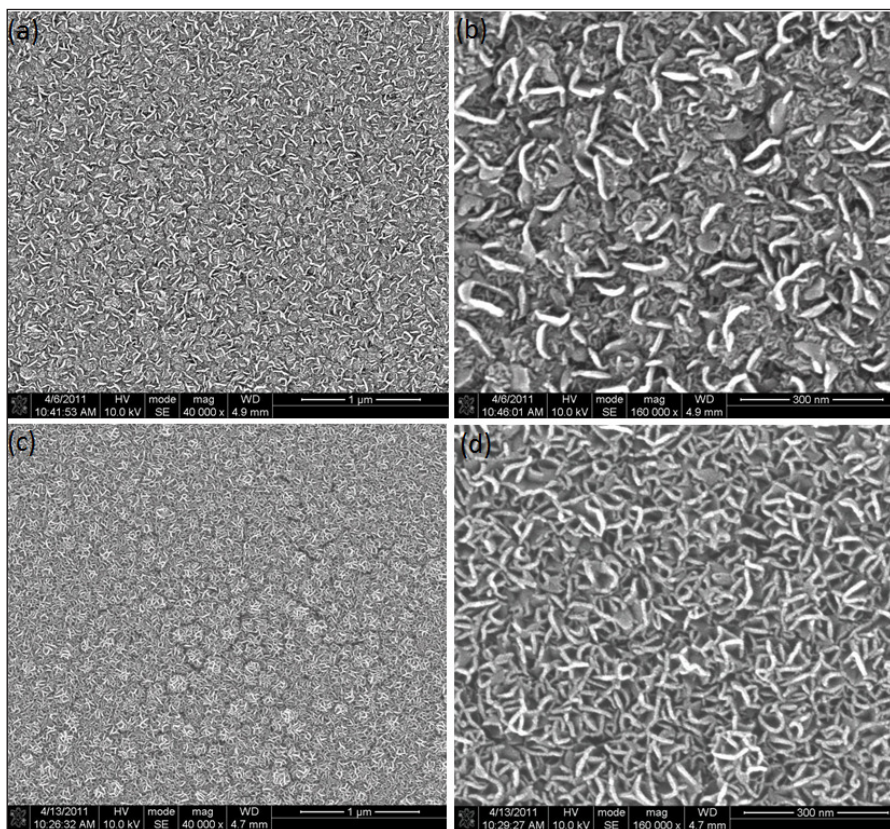

Fig. 1: The surface morphology of the nanostructured film grown for two different times (a) Low and (b) High–resolution SEM images for 10 minute grown film, and (c) Low and (d) High–resolution images of 30 min. grown film.
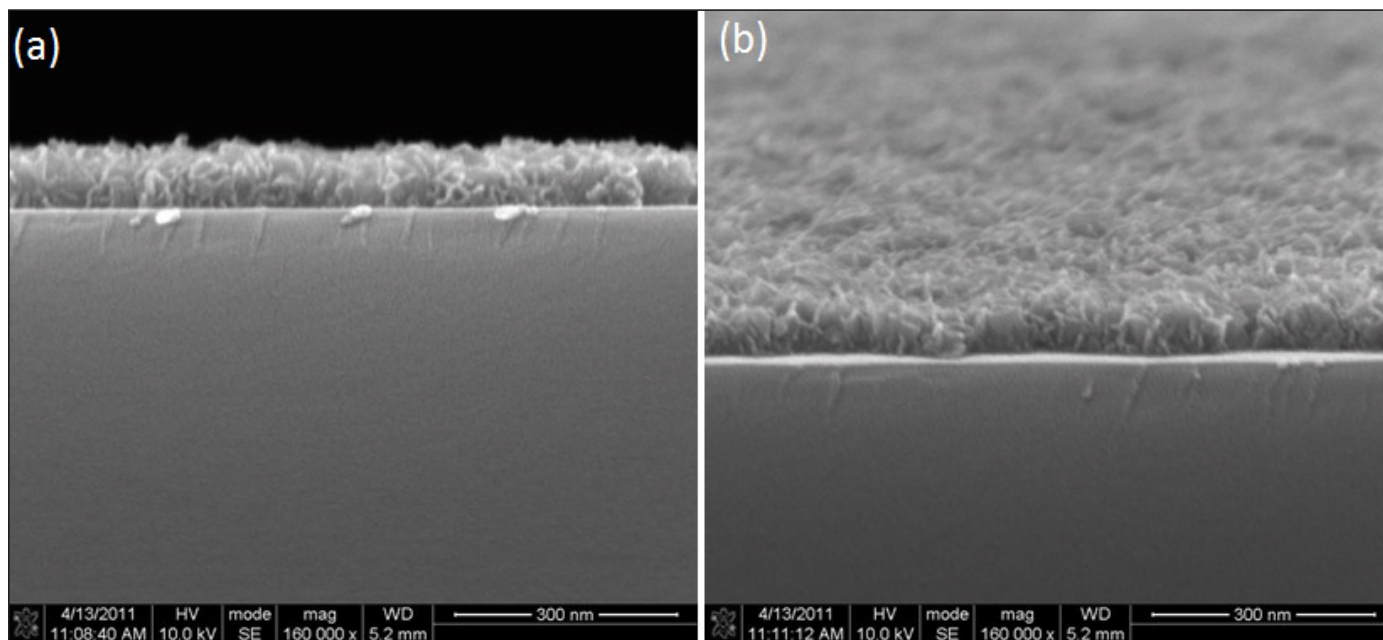
Fig. 2: *The cross-sectional SEM images of the film grown for 30 minute (a) normal and (b) tilted view.*

leads to a large number of side edges and short top edges in the film, which provides an increased effective surface activation. From the cross-sectional SEM images (Figure 2) of the FLVG film (grown for 30 min) the height of the flakes is found to be ~ 77 nm, and the thickness is in the range of ~ 3 –7 nm.

We further probed the onset of FLVG film growth through cross-sectional transmission electron microscope (TEM) imaging of the substrate-film interface as shown in Figure 3. The high-resolution TEM image (HRTEM) image of the film-substrate interface (Figure 3b) reveals that during the initial-stage of the growth, the graphene layers lying parallel to the substrate surface. Subsequently, the outer planes of the horizontal graphene surface preferentially curls-up and progressively turned into the vertical direction followed by the inner planes. Then, the growth transforms into one-dimensional wire-like structure up to a height of ~5–7 nm. Finally, the wire-like carbon structures branched

anisotropically into a two-dimensional form, exhibiting a nanowall-like structure. The spacing between the graphene layers is ~ 0.34 nm. From the HRTEM picture, the regions show a lattice spacing of ~ 0.21 nm, which indicates the presence of nanocrystalline diamond in the film matrix.

Raman spectroscopy and X-ray photoemission spectroscopy (XPS) analysis are employed to study further the details of the crystalline structure of the FLVG film grown for 30 minutes. Figure 4a shows a typical Raman spectrum of the FLVG film. The spectra consist of two prominent peaks at 1340 cm^{-1} and 1580 cm^{-1}, commonly
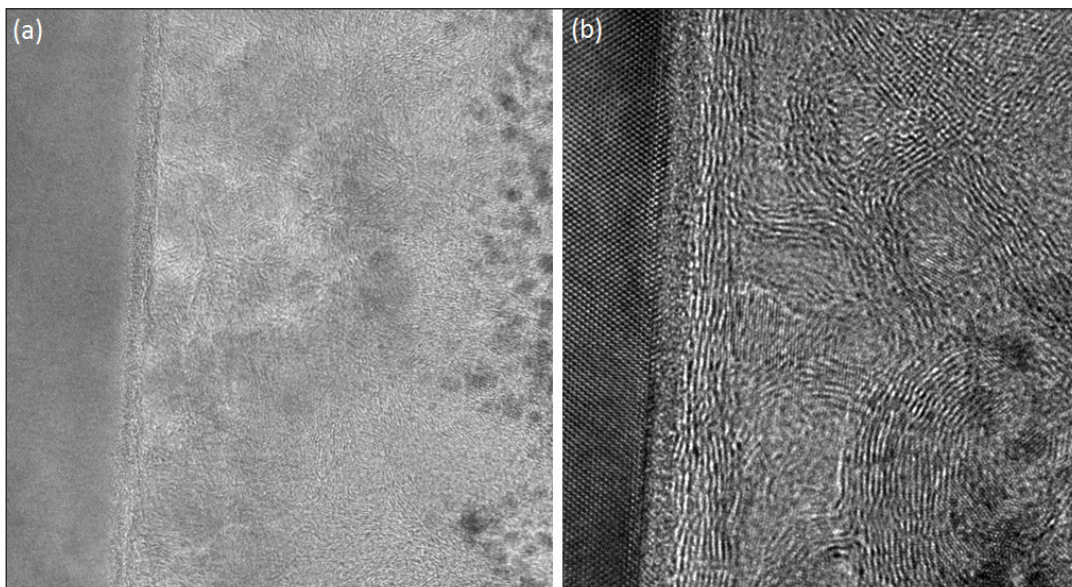

Fig. 3: *(a) TEM and (b) HRTEM images of the FLVG-nanodiamond hybrid film.*
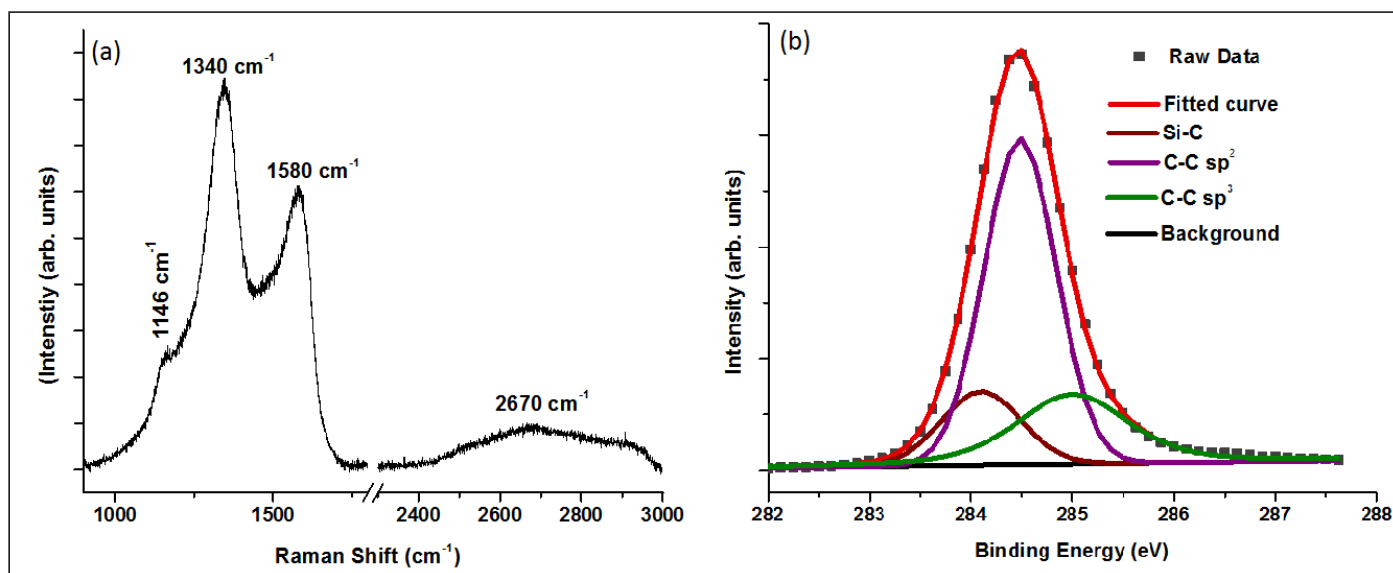
Fig. 4: A typical (a) Raman and (b) XPS spectra of the FLVG-nanodiamond hybrid structure.

known as D- and G-mode, respectively, which are characteristics features of graphitic structures [30]. The G-peak is established as an effect of E_{2g}-phon vibration centered at the graphene Brillioun zone. The D-peak appeared due to the defect-induced double resonance inter-valley scattering of phonons at the K-point of the Brilioun zone. The broad peak at 2670 cm^{-1} is known as 2D-mode of graphene, an overtone of D-mode, which is a defect free mediated two-phonon combination process [30]. The appearance of 2D- and G-mode signifies the presence of sp^{2}crystalline carbon form. The small peak at 1146 cm^{-1} indicates the presence of trans-polyacetylene carbon form, usually observed in the grain boundaries of nanocystalline diamond [31]. It corroborates with the HRTEM results, which again indicates the presence of nanocrystalline diamond in the FLVG film. The high-resolution C1s XPS spectra of the FLVG/nanodiamnd composite film shown in Figure 4b can be deconvoluted into three distinct peaks. The peak at binding energy (BE) of 284.1 eV is closely resembling with the BE of silicon carbide (Si-C) [29] believed to be formed at the substrate- film interface, which resembles with the HRTEM observation (Figure 3b). The peaks at 284.5 eV and 285 eV are corresponds to the C-C sp^2 bonded graphitic and C-C sp^3 bonded diamond nanostructures, respectively [32, 33].

The possible growth mechanism of the FLVG structure can be understood by considering its microstructural evolution as a function of the critical growth parameters. In earlier reports, the mechanism for the catalyst-free vertical growth of various carbon nanostructures are predicted to be either due to the highly directed electric filed caused by the localized plasma or due the self-assembly of the

graphene sheets parallel to the substrates in the form of laterally connected carbon nanosheets or nanowalls [17-26]. However, the present HRTEM observations of the FLVG film (Figure 3b) suggest that at the beginning of the growth, a thin amorphous carbon layer (3 nm) deposited at the substrate surface, followed by the horizontal graphene plane. The graphene planes on top of the amorphous carbon layer lying horizontally parallel to the substrate surface, might have formed either by the coalescence of graphene nanoislands [34] or due to the condensation of carbon cluster along one direction forming continuous parallel graphene layers [25].The subsequent transition of graphene plane from the horizontal plane to vertical plane proposed to be caused by many factors. Yoshimura et al [35] have discussed that the formation of a new crystalline phases at a critical growth time changes the orientation of graphene layers. Soin et al [36] have argued that the release of stress at the grain boundary due to the collapse of carbon islands causes the vertical transition of the graphene plane from its parallel direction. However, in the present study, the HRTEM micrograph analysis (Figure 3b) clearly indicates that the vertical growth succeeded by progressive curving of the graphene plane from the horizontal surface rather than direct nucleation of carbon atoms in perpendicular to the horizontal graphene plane. The upwardly curled carbon edges serve as nucleation sites for the vertical growth, which subsequently attracts more number of carbon atoms from the growth species as compared to the planar ones, possibly due to the temperature gradients. Eventually, the growth transformed in the vertical direction due to the high surface mobility of incoming carbon-bearing species. Malesevic et al [37]
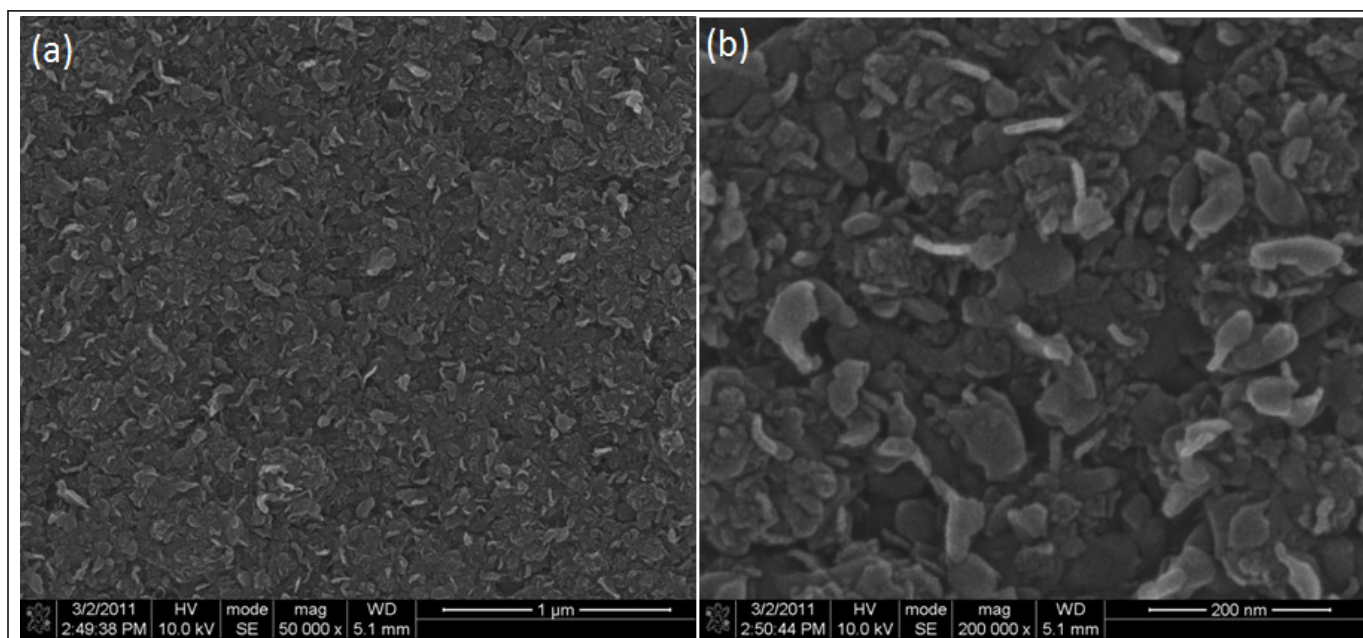
Fig. 5: (a) Low and (b) High resolution SEM images of the carbon nanostructured film grown without nitrogen content in the precursor gas–mixture.

have observed a similar phenomenon, which suggest that the curling edges formed either by the ion bombardment or due to the lattice mismatch between the substrate and graphite planes serve as nucleation sites for the vertical growth.

However, up to now, it explains only the vertical direction of the growth. The vertical growth of graphene in a two-dimensional form, rather than in one-dimensional form (vertical nanowire-like structure) is still puzzling and yet to be understood. It can be rememorized that the HRTEM micrograph (Figure 3) indicated that the two-dimensional vertical growth appeared only after few nanometers of one-dimensional vertical growth from the horizontal graphene planes. This depicts that the two-dimensional growth of graphene plane is not a natural selection/direct nucleation from the horizontal surface. Therefore, we further inspected the growth behavior of the FLVG film by carrying out the growth without adding nitrogen gas in the feed gas mixture of Ar/CH4/H2 (78/2/20 SCCM), keeping all the growth parameters constant.

The SEM micrograph of the film shows that the grown carbon nanostructures are lying parallel to the substrate surface and rarely being vertical, as shown in Figure 5. It illustrates that the nitrogen induced defects might have stimulated the two-dimensional vertical growth. It has been observed that the incorporation of nitrogen atoms into the hexagonal structure of graphene sheets creates pyrrolic- and pyridinic-like pentagonal defects [38-41]. Chan et al [42] have shown that the nitrogen-induced pentagon defects create distortion and curving of the graphene layers, which lead to graphene sheets of high curvatures and cross-linked structures. The curling of carbon planes induced by the pentagon defects is due to the asymmetric behaviour of the free carbon atoms attached to these defects, where the three in-plane sp^2-bonds and a P_z orbital aligned perpendicular to this plane. This asymmetry not only conduce the curved structure, but also provides sites for the damage of the surface and thus the further branching of the nanostructure; a process commonly observed in the synthesis of carbon nanotube [43]. Interestingly, the present experimental observations depict a similar phenomenon. The basal planes of the few layered graphene get distorted and buckled by the nitrogen induced defects, and thus curled upward in order to inhabit the vertical growth. Consequently, the vertical growth transformed into a two-dimensional nanostructure due to the bending of graphene layers in both the directions, and the subsequent nucleation of carbon atoms on top of it adds more number of graphene layers on to it following the existed bending pattern.

The presence of diamond nanoparticles in the matrix of graphene planar structure is due to the presence of low concentration of hydrogen in the plasma. A transition from hydrogen-rich plasma to argon-rich plasma decreases the diamond stability from the macro- to the nano-scale, hence favours growth of diamond nanoparticle [44, 45].

4. Conclusion

In conclusion, I have demonstrated the growth of

few-layered vertical graphene (FLVG) – nanodiamond hybrid structure in a single-step using a non-catalytic thermally activated HFCVD technique. The Raman and HRTEM observation of the hybrid film confirms the presence of nanodiamond structure in the film matrix. The microstructural analysis of the HRTEM results of the substrate-film interface reveals a step-by-step transition of the planar growth to vertical growth and their further branching into the FLVG structure. We have shown that the nitrogen gas inclusion in the precursor gas-mixture of $CH_4/H_2/Ar$ transforms the planar growth of graphene into vertical FLVG structure. The results indicate that the nitrogen-induced defects in the graphene lattice might have stimulated the upward curving of graphene layers form the horizontal surface and their further branching in the two-dimensional vertical plane, which give rise to the FLVG structure. The presence of diamond nanoparticles in these films is due to the Ar-rich gas chemistry in the growth process, which favours nanodiamond growth.

References:

1. C. W. Padgett, O. Shenderova, D. W. Brenner, Nano Letter 6 (2006) 1827.

2. O. Shenderova, D. Brenner, R. S. Ruoff, Nano Letter 3 (2003) 805.

3. V. A. Fonoberov, A. A. Balandin, Nano Letter 6 (2006) 2442.

4. S. Ghosh, I. Calizo, D. Teweldebrhan, E. P. Pokatilov, D. L. Nika, A. A. Balandin, W. Bao, F. Miao, C. N. Lau, Applied Physic Letter 92 (2008) 151911.

5. N. J. Yang, H. Uetsuka, E. Osawa, C. E. Nebel, Angew Chemistry 47 (2008) 5183.

6. N. Shang, P. Papakonstantinou, P. Wang, A. Zakharov, U. Palnitkar, I. –N. Lin, M. Chu, A. Stamboulis, ACS Nano 3 (2009) 1038.

7. K. S. Novoselov, A. K. Geim, S. V. Morozov, D. Jiang, Y. Zhang, S. V. Dubonos, I. V. Grigorieva, A. A. Firsov, Science 306 (2004) 666.

8. A. S. Mayorov, R. V. Gorbachev, S. V. Morozov, L. Britnell, R. Jalil, A. Leonid, P. P. Blake, K. S. Novoselov, K. Watanabe, T. Taniguchi, A. K. Geim, Nano Letter 11 (2011) 2396.

9. X. Du, I. Skachko, F. Duerr, A. Luican, E. Y. Andrei, Nature 462 (2009) 192.

10. A. K. Geim, Science 324 (2009) 1530.

11. N. G. Shang, P. Papakonstantinou, M. McMullan, M. Chu, A. Stamboulis, A. Potenza, S. S. Dhesi, H. Marchett, Advance Functional Materials 18 (2008) 3506.

12. C. C. Chen, C. F. Chen, I. H. Lee, C. L. Lin, Diamond and Related Materials 14 (2005) 1897.

13. Y. Wu, B. Yang, B. Zong, H. Sun, Z. Shen, Y. Feng, Journal of Material Chemistry 14 (2004) 469.

14. E. Luais, M. Boujtia, A. Gohier, A. Tailleur, S. Casimirius, M. A. Djouadi, A. Granier, P. Y. Tessier, Applied Physics Letter 95 (2009) 014104.

15. J. Yu, R. Qian, P. Jiang, Fibers and Polymers 14 (2013) 1317.

16. Y. Wu, B. Yang, G. Han, B. Zong, H. Ni, P. Luo, T. Chong, T. Low, Z. Shen, Advance Functional Materials 12 (2002) 489.

17. K. Shiji, M. Hiramatsu, A. Enomoto, M. Nakamura, H. Amano, M. Hori, Diamond and Related Materials 14 (2005) 831.

18. Y. Wu, P. Qiao, T. Chong, Z. Shen, Advanced Materials 14 (2002) 64.

19. M. Hiramatsu, K. Shiji, H. Amano, M. Hori, Applied Physics Letter 84 (2004) 4708.

20. J. J. Wang, M. Y. Zhu, R. A. Outlaw, X. Zhao, D. M. Manos, B. C. Holloway, V. P. Mammana, Applied Physics Letter 85 (2004) 1265.

21. M. Hiramatsu, M. Hori, Japanese Journal of Applied Physics 45 (2006) 5522.

22. S. Kondo, M. Hori, K. Yamakawa, S. Den, H. Kano, M. Hiramatsu, Journal of Vacuum Science and Technology B 26 (2008) 1294.

23. T. Mori, M. Hiramatsu, K. Yamakawa, K. Takeda, M. Hori, Diamond and Related Materials 17 (2008) 1513.

24. O. Tanaike, N. Kitada, H. Yoshimura, H. Hatori, K. Kojima, M. Tachibana, Solid State Ionics 180 (2009) 381.

25. N. G. Shang, F. C. K. Au, X. M. Meng, C. S. Lee, I. Bello, S. T. Lee, Chemical Physics Letter 358 (2002)187.

26. T. Itoh, Thin Solid Films 519 (2011) 4589.

27. L. Giorgi, T. D. Makris, R. Giorgi, N. Lisi, E. Salernitano, Sensor and Actuator B 126 (2007) 144.

28. S. Sahoo, D. R. Mohapatra, H. –J. Lee, S. M. Jejurikar, I. Kim, S. –C. Lee, J. –K. Park, Y. –J. Baik, W. S. Lee, Carbon 67 (2014) 704.

29. N. Lisi, R. Giorgi, M. Re, T. Dikonimos, L. Giorgi, E. Salernitano, S. Gagliardi, F. Tati, Carbon 49 (2011) 2134.

30. A. C. Ferrari, D. M. Basko, Nature Nanotechnology 8 (2013) 235.

31. L. Y. Zeng, H. Y. Peng, W. B. Wang, Y. Q. Chen, D. Lei, W. T. Qi, J. Liang, J. Zhao, X. Kong, H. Zhang, Journal of Physical Chemistry C 112 (2008) 1401.

32. H. Medina, Y. C. Lin, C. Jin, C. C. Lu, C. H. Yeh, K. P. Huang, K. Suenaga, J. Robertson, P. W. Chiu, Advanced Functional Materials 22 (2012) 2123.

33. F. Y. Xie, W. G. Xie, J. Chen, X. Liu, D. Y. Lu, and W. H. Zhang, Journal of Vacuum Science and Technology B 26 (2008) 102.

34. S. Ghosh, K. Ganesan, S. R. Polaki, T. R. Ravindran, N. G. Krishna, M. Kamruddina, A. K. Tyagi, Journal of Raman Spectroscopy 45 (2014) 642.

35. H. Yoshimura, S. Yamada, A. Yoshimura, I. Hirosawa, K. Kojima, M. Tachibana, Chemical Physics Letter 482 (2009) 125.

36. N. Soin, S. S. Roy, C. Kane, J. A. D. McLaughlin, T. H. Limb, C. J. D. Hetherington, CrystEngComm 13 (2011) 312.

37. A. Malesevic, R. Vitchev, K. Schouteden, A. Volodin, L. Zhang, G. V. Tendeloo, A. Vanhulsel, C. V. Haesendonck, Nanotechnology 19 (2008) 305604.

38. H. Gao, L. Song, W. Guo, L. Huang, D. Yang, F. Wang, Y. Zuo, X. Fan, Z. Liu, W. Gao, R. Vajtai, K. Hackenberg, P. M. Ajayan, Carbon 50 (2012) 4476.

39. D. Wei, Y. Liu, Y. Wang, H. Zhang, L. Huang, G. Yu, Nano Letter 9 (2009) 1752.

40. K. Ghosh, M. Kumar, T. Maruyama, Y. Ando, Carbon 48 (2010) 191.

41. S. Kar, D. R. Mohapatra, E. Feysez, A. K. sood , Phys. Rev. B 90 (2014) 165420.

42. L. H. Chan, K. H. Hong, D. Q. Xiao, W. J. Hsieh, S. H. Lai, H. C. Shih, T. C. Lin, F. S. Shieu, K. J. Chen, H. C. Cheng, Applied Physics Letter 82 (2003) 4334.

43. S. C. Mu, H. L. Tang, S. H. Qian, M. Pan, and R. Z. Yuan, Carbon 44 (2006) 762.

44. V. I. Konov, A. A. Smolin, V. G. Ralchenko, S. M. Pimenov, E. D. Obraztsova, E. N. Loubnin, S. M. Metev, G. Sepold, Diamond Relat. Mater. 4 (1995) 1073.

45. D. M. Gruen, Annu. Rev. Mater. Sci. 29 (1999) 211.

Dr. Dipti Ranjan Mohapatra, *working as Assistant Professor in the Department of Physics, Vikram Deb (Autonomous) College, Jeypore, Koraput, Odisha-764001, since February 2015. He completed his Ph. D. degree in Condensed Matter Physics from IIT Bombay in 2010.Dr. D. R. Mohapatra worked as a postdoctoral fellow under DST Nanomission postdoctoral fellowship at Indian Institute of Science, Bangalore, in the group of Prof. Ajay kumar Sood (July 2011 – February 2015). Also, he was a postdoctoral fellow in the department of electronic material center, Korea Institute of Science and Technology, South Korea (August 2010 – June 2011). Dr. Mohapatra is an expert in synthesizing carbon-based materials namely single crystal diamond, graphene and carbon nanotubes using various CVD techniques. These materials are extensively studied for photo-sensors and transistor applications. He has more than 20 research publications in international peer reviewed journals. He has developed and taught various courses of Physics to postgraduate and undergraduate students. He is also consulting industries for growing single crystal diamond.*

Effect of nitrogen ion implantation on electron field emission property of nanocrystalline diamond films

Umesh Palnitkar, Huan Niu and I-Nan Lin
Department of Physics, Tamkang University, Tamsui 251, Taiwan, R. O. C.
Nuclear Science and Technology Development Center Accelerator Division, National Tsing-Hua University,
Hsinchu, Taiwan 300 R. O. C.
E-mail: upalnitkar@gmail.com

Abstract

Nanocrystalline diamond (NCD) films were grown by microwave plasma assisted chemical vapour deposition with CH_4 and H_2 as precursor with varying CH_4: H_2. These films were implanted with Nitrogen ions at doses of 10^{13} and 10^{15} ions/cm^2 (Energy 100 keV). The structural modification has been investigated using UV Raman spectroscopy, field emission scanning electron microscopy, near edge X-ray absorption fine structure (NEXAFS). A systematic investigation on the films microstructure and their electron field emission (EFE) properties are presented. The structural modification at the subsurface resulted in a significant reduction of electric field required for field emission. It was also found that the EFE property highly depended on the graphite/diamond mixed phase structure. Optimized condition is observed for 3 % CH_4 film implanted with 10^{15} ions/cm^2 where turn on field is observed at 14 V/µm with current density of 1.92 mA/cm^2 (at 40 V/µm).

Keywords: Electron field emission, Nanocrystalline diamond films, Chemical vapour deposition

1. Introduction

Field emission displays (FEDs) have the potential to be low cost, high performance alternative to the currently dominant cathode ray tube and liquid crystal display technologies for flat panel displays. One of the key issues in FEDs has been the development of reliable and efficient cold cathode material for electron field emitters. Earlier field emitter typically employed metals (such as Mo) or semiconductors (such as Si) with nanometer sized sharp tips. These emitters typically require complicated fabrication steps and need high control voltage for emission (100 V) because of high work function associated with these materials.

Diamond and related materials have extensively been studied for their novel mechanical, chemical and electrical properties. Particularly because of low or negative electron affinity (NEA), diamond is optimum candidate for field electron emission materials that has potential applications in the area of flat display and vacuum microelectronic devices. Cold cathode field emission has been demonstrated in chemical vapour deposited diamond films, from which a prototype flat panel display has even been made [1]. However the mechanism of electron emission from chemical vapour deposition (CVD) diamond films remains to be investigated, although several models have been suggested such as surface morphology [2], back metal contact [3], surface diode [4] and defect induced

energy band [5,6]. A paradox is that diamond films with poor quality gives good electron field emission (EFE) properties making the problem more complicated [7].

In the present article we present a systematic study on the synthesis and electron field emission characterization of NCD films grown by microwave plasma CVD using Ar/CH_4 as precursors. Ion implantation technique has been used to induce defects in the NCD films and to create a structural transformation from diamond to graphite to some extent. The electron field emission properties of NCD films are found to be highly dependent on their microstructure.

2. Experiment

NCD films were deposited by microwave plasma enhanced chemical vapor deposition process (2.45 GHz ASTeX MPECVD system). The CH_4 / H_2 gases with flow rate of 45/300 sccm (~55 Torr) were excited by 1500-W microwave power. The diamond nuclei were formed on mirror smooth silicon substrate by applying a negative bias voltage (-135 V) to the substrate with respect to the plasma. The bias current was around 45 mA at the beginning of the application of bias voltage. The bias current value remained at such small value for about few minutes and increased abruptly, indicating the onset of the formation of diamond nuclei, and saturated after a few minutes, implying the full coverage of the diamond nuclei on the substrates. The depositions were carried out at methane concentrations of CH_4 / H_2 ratio of 3/97 and 5/95 in balanced hydrogen atmosphere at a pressure of 55 Torr with a microwave

power of 1500 W for 90 mins to a thickness around 250 nm. The corresponding NCD films were designated as films A and B, respectively.

Ion implantation was performed in HVEE500kV – Implantor at Nuclear Science and Technology Development Center, National Tsing-Hua University, Taiwan. The chamber pressure during implantation was kept at 10^{-6} torr. All the samples were implanted with

Fig. 1: SEM micrographs of nitrogen ion-implanted films grown at (a) 3% and (b) 5% CH_4/H_2.

100 keV nitrogen ions at room temperature. NCD films were implanted with nitrogen ions of 100 keV at doses of 10^{13} and 10^{15} ions/cm². The penetration depth of the ions has been calculated by Stopping and Range of Ions in solids (SRIM 2006) program. It was found to be around 120 nm. This shows that ions are stopping well inside the film as thickness of the film is around 250 nm. The energetic ions while passing through target material, loss energy either by elastic or inelastic collisions. Thus the fast moving ions are expected to create defects and structural damage in the target material [8]. Before and after ion implantation NCD films were characterized by field emission scanning electron microscopy (FESEM, JEOL 6010) and Raman spectroscopy (Renishaw). Electron field emission was measured by a parallel-plate setup. The cathode to anode distance controlled by a micrometer attached to it. The chamber pressure during electron field emission was maintained at 10^{-6} Torr. The current–voltage properties were measured by an electron source unit (Keithley, Model 237). The NEXAFs spectra were performed using the high energy spherical grating monochromator beam line at National Synchrotron Radiation Research Center (NSRRC), Hsinchu, Taiwan.

3. Result and discussion

The scanning electron microscopy (SEM) micrographs (Fig. 1) showed continuous films were deposited and the crystal size increases with methane percentage. It varied from 200 nm to 250 nm as the CH$_4$ increases from 3% to 5%. UV Raman (324 nm) spectra of the as deposited and ion implanted films was studied (Fig. 2). An unambiguous signature of diamond is seen at 1332 cm⁻¹ (D-band) in all films suggesting the film of diamond. The spectra also showed a significant amount of graphitic carbon in the film that is evident by G-band at 1580 cm⁻¹. After Lorentzian peak fitting to Raman spectrum of as deposited NCD films, two more peaks, one around 1140 cm⁻¹ (D$_1$-band) and the
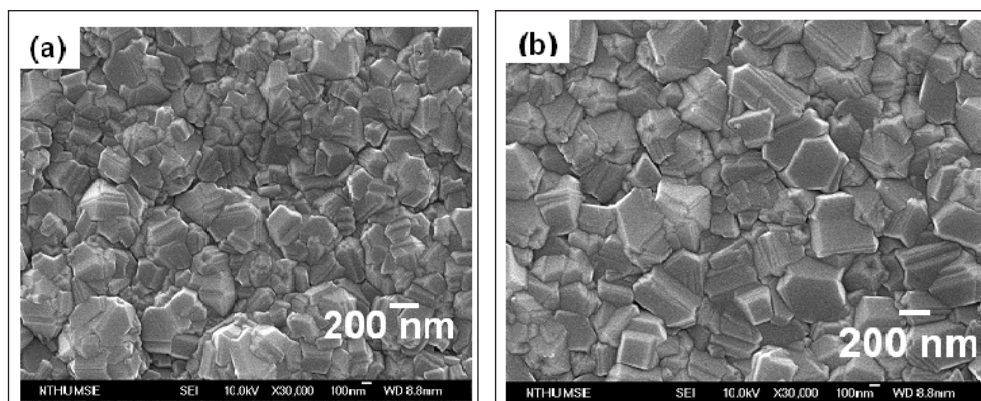
other around 1360 cm⁻¹ (D$_2$-band), were deconvoluted. The D$_1$ and D$_2$-bands are presumably contributed by the presence of nano-sized grains in these diamond films [9]. Both the films A & B showed increase in Full Width Half Maximum (FWHM) due to ion implantation (Figs. 2 (a$_{II}$) and 2 (b$_{II}$)). This suggests that defects were generated in NCD film [10]. Broad D$_2$ band around 1360 cm⁻¹ is more prominent in all films after a dose of 10¹³ ions/cm², indicating the increase in proportion of nano-sized grains due to N ion implantation. Interestingly after 10¹⁵ ions/cm² dose, the diamond signature line becomes weak (Figs. 2(a$_{III}$) and 2 (b$_{III}$)). The broad D$_2$-band shifts towards lower value indicating formation of disorder chains.

While Raman spectra illustrate clearly the modification on defect structure of nanocrystalline diamonds due to N ion implantation process, the quantitative analysis of the defects induced from these spectra is difficult due to the relatively different sensitivity of Raman scattering for sp² and sp³ component. That initiated us to study the near edge X-ray absorption fine structure (NEXAFs) study of as deposited as well as implanted films, since NEXAFs is one of the best tool to quantify the sp² and sp³ component in diamond film. Figure 3 displays the C K-edge NEXAFs spectra of as deposited and implanted films. The spectra were normalized using the incident beam intensity I$_o$ and keeping the area under the spectra in the energy range between 314 and 335 eV fixed. The NEXAFs energy range for diamond generally can be divided into two regions characterized by specific features. One is a spike of C 1s core excitation resonance at approximately 289.2 eV. Another is a relatively broad σ* feature in the energy between 288.6 and 302 eV for the sp³ bonded carbon. The relatively small peak at ~285 eV can be attributed to graphite like π* state of sp² bonded carbon. The peak at 287 –288 eV, between π* and σ* features can be attributed to the C-H bond on the diamond surface.
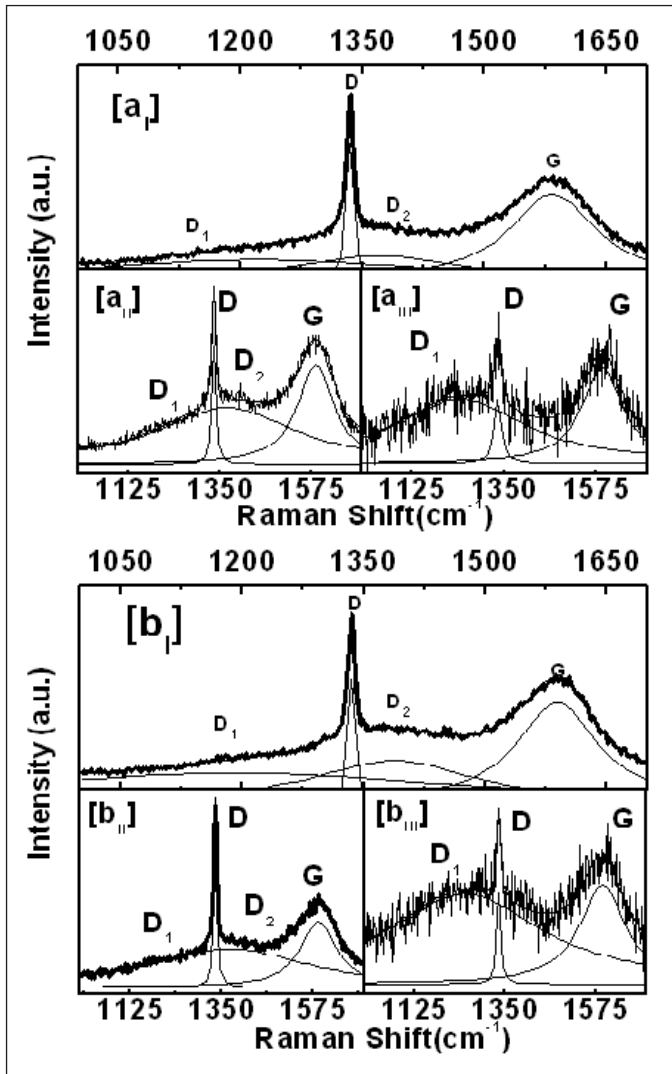
Fig. 2: *UV Raman spectra of diamond films grown at (a) 3 % and (b) 5 % CH$_4$/ H$_2$; where (a$_I$ & b$_I$) are as-grown, (a$_{II}$ & b$_{II}$) are 10^{13} ions/cm^2 nitrogen ion-implanted and (a$_{III}$ & b$_{III}$) are 10^{15} ions/cm^2 nitrogen ion-implanted films.*

From Fig. 3, it can be clearly seen that after ion implantation the spike of C 1s at 289.2 eV initially drops for 10^{13} ions/cm^2 (curves a$_{II}$ and b$_{II}$) and disappears at higher dose of 10^{15} ions/cm^2 (curves a$_{III}$ and b$_{III}$). This decrease is mainly due to local modifications of diamond crystalline structure caused by the formation of point defects, where short range crystalline order was affected. This peak seems to be most sensitive to defects introduced by ion implantation [11]. At the same dose very less effect is observed on the second band gap at 302 eV. This peak gradually increases with increase in ion dose indicating deterioration of diamond band structure. Moreover, the peak around 285 cm^{-1} is found to increase with dose. This indicates conversion of sp^3 phase into sp^2 in NCD film after ion implantation.
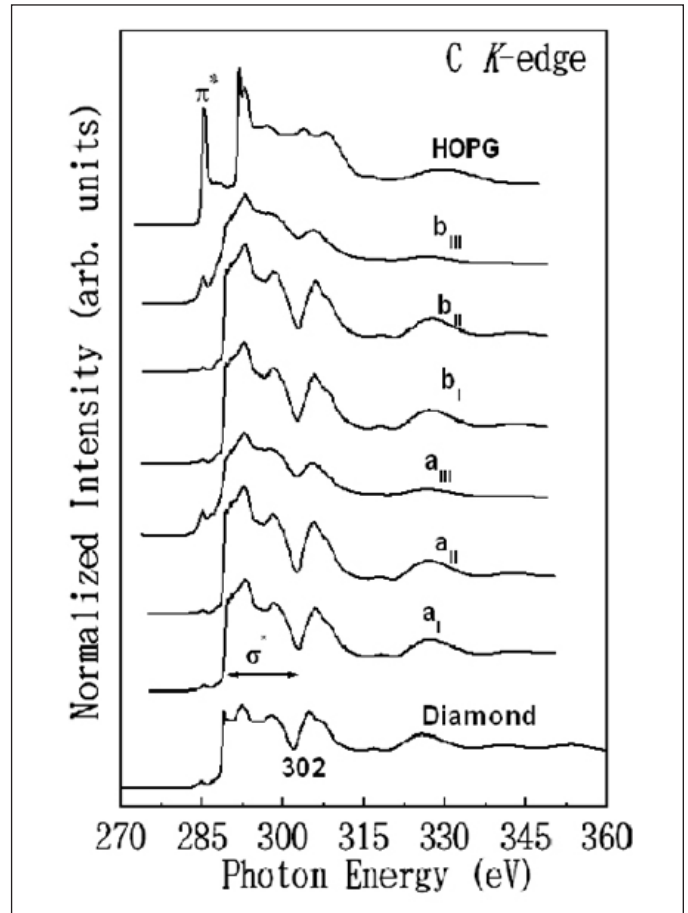

Fig. 3: *Carbon K-edge NAXAF spectra of as deposited and implanted films grown at (a) 3% and (b) 5% CH$_4$/H$_2$; where (a$_I$ & b$_I$) are as-grown, (a$_{II}$ & b$_{II}$) are 10^{13} ions/cm^2 nitrogen ion-implanted and (a$_{III}$ & b$_{III}$) are 10^{15} ions/cm^2 nitrogen ion-implanted films (The NEXAFs for single crystalline diamond and highly oriented pyrolysis graphite, HOPG, were also included to facilitate the comparison).*

In Fig. 4 we have shown the emission current density v/s electric field (J - E) curves for the films A & B grown at different methane concentrations with ion implantation with varying dose. The obtained J-E data was analyzed using Fowler-Nordheim Theory [12]. The detailed calculation provided important parameters like turn-on field, current density (Table 1). It can be clearly seen that the turn-on field (E$_0$) is decreased after N ion-implantation from the as grown turn-on field value for both films. In contrast, the EFE current density (J$_e$) is insignificantly altered due to low dosage (10^{13} ions.cm^2). N ion-implantation but is markedly increased resulted from the high dosage (10^{15} ions.cm^2) N ion-implantation. The EFE current density increase in larger extent for film A (3% CH$_4$), as compared with that for film B (5% CH$_4$).

The damage caused by N ion-implantation plays a dominant role in the field emission enhancement of diamond films. This damage can directly produce number
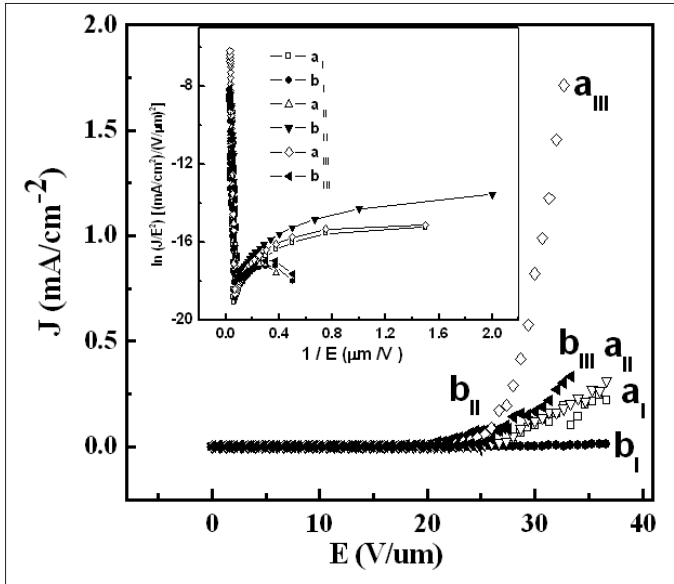
Fig. 4: *The electron field emission current density vs. electric field, J –E Plots for as deposited and implanted films grown at (a) 3% and (b) 5% CH$_4$/ H$_2$; where (a$_I$ & b$_I$) are as-grown, (a$_{II}$ & b$_{II}$) are 10^{13} ions/cm^2 nitrogen ion-implanted and (a$_{III}$ & b$_{III}$) are 10^{15} ions/cm^2 nitrogen ion-implanted films.*

of defects in the surface region that include vacancies, dislocations, stacking faults, and second phase such as graphite and amorphous carbon components. These defects alter the work function and affect the field emission property. In addition, when the number of defects is significant, the electronic states of the defects could form one or more bands within the bulk diamond band gap [13]. Electrons can be excited from the defect bands to the surface states for emission. Thus, we observe reduction in the turn-on field from the value of as grown film. These defects have altered work function of as deposited NCD films. Such an argument is supported by the increase in FWHM of diamond signature line after ion implantation (Fig. 2 and Table 1). That the decrease in turn on field is

Table 1 Field Emission measurement Analysis (*J$_e$: EFE current density measured at 40 V /μm applied field)

Sample		FWHM	$\Delta (I_{sp}{}^2/ I_{sp}{}^3)$	J (mA/ cm^2)	E (V/ μm)
3%	As Grown	13	0.00449	0.151	18
	10^{13}	31	0.0047	0.196	13.33
	10^{15}	-	0.03441	1.926	14
5%	As Grown	19	0.004470	0.0158	16
	10^{13}	21	0.004570	0.1414	13.5
	10^{15}	-	0.03029	0.3312	11.33

attributed to the defects introduced in the surface regions is in accordance with the previous observation [14]. Restated, the defects created by ion implantation seem to be sufficient to create a defect band within the diamond band gap. Electrons can be emitted directly into vacuum from these defect bands or the surface states. This may be the reason for reduction of turn-on field. The effect of N ion-implantation on improving the EFE current density (J$_e$) cannot be explained in the same straight forward mechanism as that on lowering the turn-on field (E$_0$), which will be described shortly.

To more detailed investigate the effect of ion implantation on field emission property for diamond films, the integration of intensities over π*-bond between 281.6 to 286.1 eV (I$_{sp2}$) and σ*-bond between 288.6 to 302.4 eV (I$_{sp3}$) were estimated, where the I$_{sp2}$ and I$_{sp3}$ represents enhanced absorption of X-ray by electron transit from the C 1s core state to un-occupied sp^2 or sp^3 bond, respectively. Typical Guassian fitting to curve a$_I$ is shown in Fig.5. The dotted lines in the figure indicated the Guassian fitting. Here guassian fittings have been used for base line fitting.
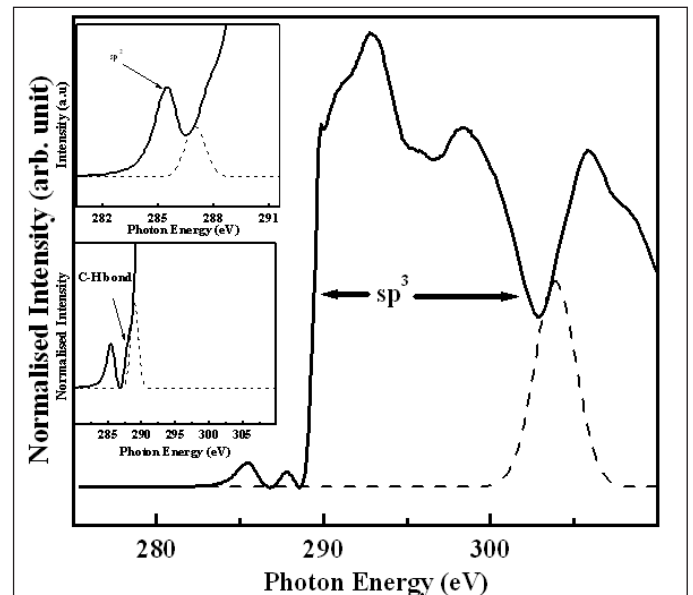

Fig. 5: *Guassian Fitting for calculation of sp^2, C-H bonding and sp^3 (Dotted lines indicates Guassian fitting)*

The inset shows the peak associated with sp^2 bonding and C-H bonding. It is observed that integral intensity of C-H bonding has direct correlation to turn on field of the films. It is observed that the integral intensity is more in case of as deposited film B than as deposited film A. As the integral intensity is proportional to C-H bonds present near the surface, it improves the negative electron affinity of the surface of the film [15]. This in turn reduces the turn on field that is observed in our as deposited films also (Table

1). It was observed that the integral intensity associated with C-H bonding decreases with ion implantation. This may be due to desorption of hydrogen from the surface[16].

It should be noted that I_{sp2}/I_{sp3} ratio for sample A was found to be 0.004490, 0.004769 and 0.03441 for as deposited films, ion dose 10^{13} ions/cm² and to ion dose 10^{15} ions/cm² respectively. Also noted that I_{sp2}/I_{sp3} ratio for sample B was 0.004470, 0.004570 and 0.03029. This indicates that the ratio does not cha nge much for the films for low dose (10^{13} ions/cm²) but increases profoundly for the high dose (10^{15} ions/cm²). The turn-on field (E_0) and emission current density (J_e) and are then plotted against the (η) [η is defined as $\Delta(I_{sp}^2/I_{sp}^3) = (I_{sp}^2/I_{sp}^3)_{Ion\ Implanted} - (I_{sp}^2/I_{sp}^3)_{As\ Deposited}$] in Fig 5. The η is thus a measure of relative change in sp² and sp³ content before and after ion implantation. Fig. 6 shows that when N ion-implanted for low dosage (10^{13} ions/cm²), there is no much change in η, but the turn-on field (E_0) decreases drastically. On the contrary, when N ion-implanted for high dosage (10^{15} ions/cm²), the η value increases in a large extend, but there is not much change in E_0. These observations imply that the reduction in turn-on field is not induced by the presence of sp²-bonded phase. It is mainly caused by the formation of defects and formation of defect bands, as discussed previously.

In contrast, this figure shows that the EFE current density increases pronouncedly with the $\Delta(I_{sp}^2/I_{sp}^3)$ ratio (η). Large J_e-value for the films was observed in films containing larger proportion of sp²-bonded phases (i.e., with larger η-value). For the low-dosage N ion-implanted samples, although there induced large proportion of point defects, the EFE current density is in significantly improved due to the fact that the $\Delta I_{sp}^2/\Delta I_{sp}^3$ ratio (η) is not changed much. Such a result indicates that the presence of point defects does not enhance the transport of electrons from the substrates through the diamond films to the emission sites located at the surface of the films. High conductivity paths are required for improving the EFE current density via enhancing the transport of electrons. Figure 6 implies clearly that larger proportion of sp²-bonded phase leads to higher EFE current density, which is apparently owing to the increase in number density of conduction paths for the electrons. The question is how the increase in sp²-bonded phase results in more abundant electron conduction path.

It should be reminded that the surface of diamonds can be converted into very conducting by forming the hydrogen bonds on the diamond surfaces, which were presumed due to the injection of electrons from the proton to the diamonds [17]. The same mechanism is adopted to account for the increase in EFE current density due to the increase in proportion of sp²-bonded phase. The possible
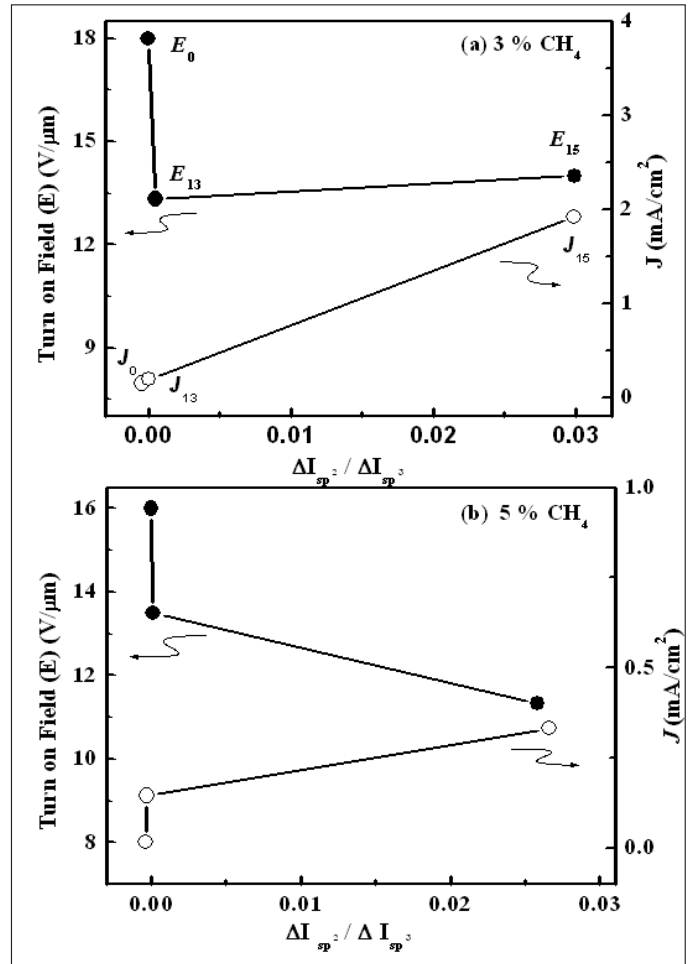

Fig. 6: The electron field emission current density (J_e) and turn-on field (E_0) vs. $\Delta I_{sp}^2/\Delta I_{sp}^3$ ratio for as deposited and implanted films grown at (a) 3% and (b)5 % CH₄/ H₂; where (J_0) are as-grown, (J_{13} & E_{13}) are 10^{13} ions/cm² nitrogen ion-implanted and (J_{15} & E_{15}) are 10^{15} ions/cm² nitrogen ion-implanted films.

mechanism is that the presence of sp²-bonded phase, which is most probably the disordered carbons, forms the diamond/ disordered carbon interfaces. The electrons were injected from the a-C phase into the diamond, rendering the region in the vicinity of interface semiconducting, which serves as electron conduction channels. The EFE current density can thus be increased markedly. Provided that the conduction channels are interconnected such that the electrons can be transport from the underlying Si-substrates to the diamond surface.

The increase in current density is very unlikely due to the nitrogen ion acquiring dopant site. If at all it acquires it, Nitrogen is well known deep level impurity and hence unsuitable for producing n type diamond [18[. The other reason to believe this is fact that the total amount of nitrogen ions concentration varies from around 10^{17} cm⁻² to 10^{19} cm⁻² for implanted dose of 1 x 10^{13} ions/cm⁻²

and 1×10^{15} ions/cm^{-2}, respectively. This concentration is not sufficient to convert it into highly conducting n type diamond film. Also earlier studies have shown following conclusions about ion implantation [19-21]: (i) There exists a critical implantation dose $2 \times 10^{14} – 10^{15}$ ions/cm^{-2} beyond which the damage cannot be healed out by annealing and the damaged layer turns to graphite (ii) Graphitization can be avoided for implantation exceeding the critical dose if the implantation are carried out at into heated (1400 ^{o}C) diamond. From all of the above discussion and looking at our experimental conditions it can be clearly concluded that the nitrogen ion implantation has very unlikely doped the nanocrystalline diamond films to give high current density. Whereas the graphitization created due to ion implantation might have created conducting channels for facilitating electron field emission property of nanocrystalline diamond film. The later may be the dominant phenomenon working in our films.

For the films A grown in 3% CH$_4$, the grains are smaller (~ 200 nm) and the number density of electron conduction channels are abundant enough to form conducting network. The increase in EFE current density due to N ion-implantation is thus prominent. In contrast, for the films B grown in 5% CH$_4$, the grains are larger (~ 250 nm) and the number density of electron conduction channels is insufficient to convert all the diamond films conducting. The improvement on EFE current density is thus only moderate.

4. Conclusion

In summary, the field required for emission from CVD diamond has been improved when diamond films are implanted by nitrogen ions. The impinging ions have created structural modification on the surface of the film. This was quantitatively studied using NEXAFs. It was observed that with ion implantation Δ (I_{sp}^2/ I_{sp}^3) ratio increased. This clearly indicates change in the microstructure of the film near the surface. An enhancement in electron field emission current density has been observed for both the films after implantation of high dose. The improvement has been seen more effectively for sample A. As nitrogen being deep donor, it could barely influence the electron field emission property. A more prominent mechanism could be the conducting channels created due to fast moving ions through the diamond films. A model based on injection of electron from these disordered carbon to diamond has been proposed to explain the increase in the electron field emission property.

References

1. N. Kumar and H. Schmidt, Semicond. Sci. Technol. 71 (1995) 73.
2. Y. H. Chen, C. T. Hu and I. N. Lin, J. Appl. Phys. 84 (1998) 3890.
3. M. W. Geis, J. C. Twichell, N. N. Efremow, K. Krohn and T. M. Lyszczarz, Appl. Phys. Letts 68 (1996) 2294.
4. T. Yamada, H. Ishihara, K. Okano, S. Koizumi and J. Itoh, J. Vac. Sci. Technol. B 15, (1997) 1678.
5. W. Zhu, G. P. Kochanski and S. Jin, Science 282 (1998) 1471.
6. A. Wisitsoraat, W. P. Kang, J. L. Davidson and D. V Kerns, Appl. Phys. Letts 71 (1997) 3394.
7. K. H. Park, S. Lee and K. H. Koh, Diam. Relat. Mater. 9 (2000) 1342.
8. J. F. Morhange, R. Beserman and J. C. Bourgoin. Jpn. J. Appl. Phy. 14 (1975) 544.
9. T. Sharda, T. Soga, T. Jimbo and M. Umeno, J. Nanosci. Nanotec. 1 (2001) 287.
10. B. Miller, R. Kallish, L. C. Feldman, A. Katz, N. Moriya, K. Short and A.E. White, J. Electrochem. Soc. 141 (1994) L41.
11. A.Laikhtman, I. Gouzman and A. Hoffman, Diamond Relat. Mater. 9 (2000) 1026.
12. T. J. Lewis, Phys. Rev. 101 (1956) 1694.
13. W.V.M. Machado, J. Kintop, M. L. De Siqueria and L.G. Ferreirra, Phys. Rev. B 47 (1993) 13219.
14. W. Zhu, G. P. Kochanski, S. Jin, L. Seibles, D. C. Jacobson, M. McCormack and A. E. White, Appl. Phys. Lett 67 (8) (1995) 1157.
15. Z. Shpilman, Sh. Michaelson and R. Kalish, Diamond Relat. Mater. 15 (2006) 846.
16. A. Laikhtman, A. Hoffman, R. Kalish, A. Breskin and R. Chechik, J. Appl. Phys. 88 (2000) 2451.
17. A. Denisenko, A. Aleksov, A. Probil, P. Gluche, W. Ebert, Diamond Relat. Mater. 9 (2000) 1138.
18. Johan. F. Prins, Nucl. Instrum. and Methods in Physics Res A 514 (2003) 69.
19. G. Braunstein, A. Talmi, R. Kalish and T. Bernstein, Radiat. Eff. 48 (1980) 139.
20. G. Braunstein and R. Kalish, Appl. Phys. Lett. 38 (1981) 416.
21. G. Braunstein and R. Kalish, Nucl. Instrum. Methods 182 (1981) 691.

	Dr. Umesh Palnitkar *has been awarded Doctoral Degree in 2003 for his work on microcrystalline diamond films from IIT Bombay. He did post-doctoral fellowship in Tamkang University, Taiwan. Presently, his research interest is studying mechanical properties of ultra-nanocrystalline diamond films.*
	Dr. I-Nan Lin *graduated from the Department of Materials Science, University of California at Berkeley in 1983. He has worked on electron field emission of diamond, diamond-like and carbon nanotube materials for more than 15 years. Presently, his research interest is studying the syntheses and characteristics of ultra-nanocrystalline diamond films.*
	Prof. Huan Niu *is working in Nuclear Science and Technology Development Center, Accelerator Division, National Tsing-Hua University, Hsinchu, Taiwan since 2003. He has been awarded Ph.D. in Atomic Physics from National Tsing Hua University, Taiwan. He is the leader of Center's Accelerator Division. His present interest is in studying magnetic properties of ion implanted nanodiamonds.*

Temperature influenced Electroluminescence in Carbon Nano-Tube Field Effect Transistors

Tapender Singh[1], Padmnabh Rai[1, 2, *]

[1]*Department of Physics & Astronomical Science, Central University of Himachal Pradesh, Dharamshala, Kangra-176206, HP, India*

[2]*School of Physical Sciences, UM-DAE Centre for Excellence in Basic Sciences, Mumbai-400098, India*

E-mail: padmnabh.rai@cbs.ac.in

Abstract

Electroluminescent properties of (17,0) carbon nanotube (CNT) field effect transistor (FET) is studied by using the non-equilibrium Green's function method (NEGF). It is observed that temperature has significant impact on the light emission properties of CNT. Depending on the different applied temperature range and thickness of oxide layer used the device light emission characteristics can be tuned. Increased number of electron hole pair's recombination event result in decrease of the drain current at higher temperature range.

Keywords: Carbon nanotubes, Surface Plasmons, Field effect transistors, Electroluminescence, Radiative recombination rate, Non-equilibrium Green's function method.

1. Introduction

The unique opto-electronic characteristics of carbon nanotubes (CNT) provides an alternative (over the existing silicon based-technology) it to be used in the different optoelectronic devices such as in photodetector, light emitting diode and in laser devices [1-3]. Due to the possibility of fabricating the low-power consumable, low cost and light weighting devices CNT can be used in the future device applied application [4]. Moreover, its direct band-gap nature and quasi 1-D structure made it a suitable material in the different fields due to its promising electrical, optical and thermal properties [1,5]. CNTFET has also been demonstrated for an electrical source for launching of surface Plasmons (SPPs) in plasmonic circuitry [6,7].

Due to the better carrier transport characteristics of CNT MOSFET as compared to Si-MOSFET, it can be used as light emitting devices [8, 9]. The field effect transistors (FET) based light emitters are most promising CNT based light emitting devices [10, 11]. Further, FET can be classified in two different classes: planar FET [9, 12] and coaxial gated FET [13]. The coaxial gated structure is considered here due to the better gate control over the CNT channel [14]. The simultaneous injection of the charge carriers (e^-/h^+) from the source and drain are responsible for the appearance of light emission characteristics [11, 15, 16]. Thus, the electroluminescence (EL) characteristics are achieved through the simultaneous injection of e^--h^+ pairs (ambipolar transport) [16].

The MOSFET like CNT-FET structure is considered in this study due to its improved performance as compared to the schottky barrier (SB)-FET: MOSFET having high-on current, higher on-off current ratio and scalability that make it suitable for the high-performance applications [17, 18]. As SB plays a crucial role in the operation of SB-FET [16, 19], it is the p-n junction which is important in MOSFET [20, 21]. The formation of the p-n junction is the main requirement to achieve the light emission characteristics in ohmic contacted FET type structures [20]. EL can also be obtained through the unipolar transport by the impact excitation mechanism [22]. Finally, radiative recombination rate (RRR) is calculated to study the light emission behaviours of CNT-FET.

2. Theory and simulation

The uncoupled 1D mode space approach is used to represent the CNT channel as a Hamiltonian (H) matrix [23]. Mode space approach is used for the simulation purpose due to its reduced computational cost as compared to the real space approach [23, 24]. Then the self-consistent iteration procedure is used to solve the Schrodinger-Poisson's equation to determine the electrostatic potential and carrier concentration on CNT channel region.
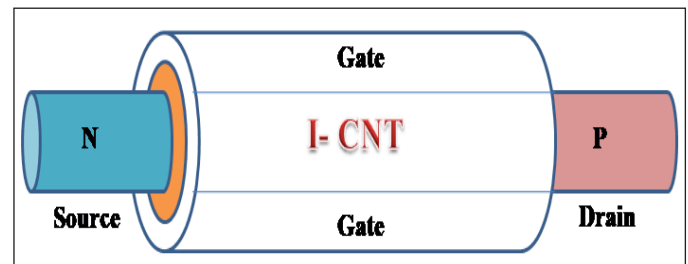

Fig. 1: *Schematic of coaxial gated CNTFET device structure with doped source and drain extension.*

Simulated CNTFET structure of coaxial gated device structure is shown in the Fig. 1 below.

Source is doped N-type and is the origin of electron carrier density (N_d) whereas drain contained P-type dopant with hole carrier density, N_d=1×10⁹m⁻¹, t_{ox}=3nm (thickness of oxide layer), k=16 (dielectric constant), T=300K, $L_{S/D}$=30nm (source/drain length) and L_{ch}=18nm (channel length) is used.

We have used the non-equilibrium Green's function method (NEGF) method to solve the Schrodinger equation. Electron and hole functions are used to find out the charge carrier's density on CNT channel [25]. The Green function is calculated by using the following equation [25].

$$G(E) = [(E + i0^+)I - H - \Sigma_1 - \Sigma_2 - \Sigma_{ineraction}]^{-1} \quad (1)$$

where, I is the identity matrix, H is the tight binding Hamiltonian CNT, E is the energy of quantum states, $i0^+$ is the small amount of the perturbation added, Σ_1, Σ_2 are the self-energy coupling matrices of source and drain (S/D) and $\Sigma_{int\,eraction}$ defines the interaction self-energy matrices. Self-energy matrixes are used to consider the effect of contact (S/D) on channel.

Carrier's interaction is considered through the carrier scattering mechanism [25-27]. Self-energy matrix interaction procedure is then used for treatment of the carriers' recombination [11]. Since current lower down due to presence of scattering event and carrier recombination has almost same effect on the current [11, 27]. To study the non-coherent transport we have considered the electron-phonon scattering as interaction mechanism.

In/out scattering function for non-coherent transport are [25, 27]:

$$\Sigma^{in}(E) = D_0 [(N_\omega + 1)G^n(E + \hbar\omega) + N_\omega G^n(E - \hbar\omega)] \quad (2)$$

$$\Sigma^{out}(E) = D_0 [(N_\omega + 1)G^p(E - \hbar\omega) + N_\omega G^p(E + \hbar\omega)] \quad (3)$$

where, D_0 is electron-phonon coupling constant, $\hbar\omega$ is the phonon energy and N_ω is number of phonon mode, can be determined by using the Bose-Einstein distributions. Electrons and holes carrier densities are defined as

$$n(z_i) = \sum_{q,s} \frac{1}{\Delta z} \int_{-\infty}^{+\infty} \frac{dE}{2\pi} G_q^n(E, q) \quad (4)$$

$$p(z_i) = \sum_{q,s} \frac{1}{\Delta z} \int_{-\infty}^{+\infty} \frac{dE}{2\pi} G_q^p(E, q) \quad (5)$$

where, Δz is the grid spacing and the summation is carried out over sub-band and spin indexes, respectively. The net current is calculated by using the following expression [23, 26, 28].

$$I = \frac{4e}{h} \int dE \, T(E)[f(E - E_S) - f(E - E_D)] \quad (6)$$

where, $T(E)$ is the transmission coefficient i.e., $T(E) = (\Gamma G \Gamma G^+)$ and f is the Fermi-Dirac distribution function. Radiative recombination rate [11, 16, 29] is calculated as follows:

$$R = \beta(np - n_i^2) \quad (7)$$

3. Result and discussion

Depending on carriers (e⁻/h⁺) energy they can occupy the certain number of energy states [30]. The local density of states (LDOS) spectrum for the different temperature range is shown in the Fig. 2 below and respective current diagram is also plotted.

The bright spikes in Fig. 2(a) represent the energy density spike where total numbers of the charge carriers are distributed. It is observed that there is some fluctuation in the density spikes at low temperature region they are not very clear for both electron and hole. As the temperature is increased from 100K to 300K it is seen that density spikes grows stronger causing to increase the current. This can be explained as follows: total carriers distribution can be defined by the fermi-dirac distribution function [30]

$$f_{S/D} = \left[\frac{\mu_{S/D} - V_{S/D}}{k_B T} \right] \quad (8)$$

At low temperature scale the (f_s-f_d) region is very small and hence few numbers of densities of states are covered inside the channel region. But at higher temperature more number of density of states are covered by the (f_s-f_d) region causing both electron and hole current to increased [31]. It is observed that both electron and hole current is very small at 100K in Fig.2 (b), with temperature enhancement more density of states are covered by (f_s-f_d) window and hence due to more carrier's excitation (the availability of large number of states) there is drastic increase in the current in Fig. 2(f). Hence increase in current is noticed with increase in temperature.

Since temperature has vital importance and it has the significant impact on the transport properties of CNT [32]. Depending on the applied biases and temperature Fermi-distribution function f_s and f_d can be changed and hence transport properties can be tuned [31,32]. Since gate has vital importance in functioning of the FET devices and is separated by the oxide layer of particular thickness [33]. Based on the different thickness of oxide used the gate control (on CNT channel) can be altered, carrier injection rate be changed and in this way carrier transport properties can be changed [33]. Hence effect of the temperature
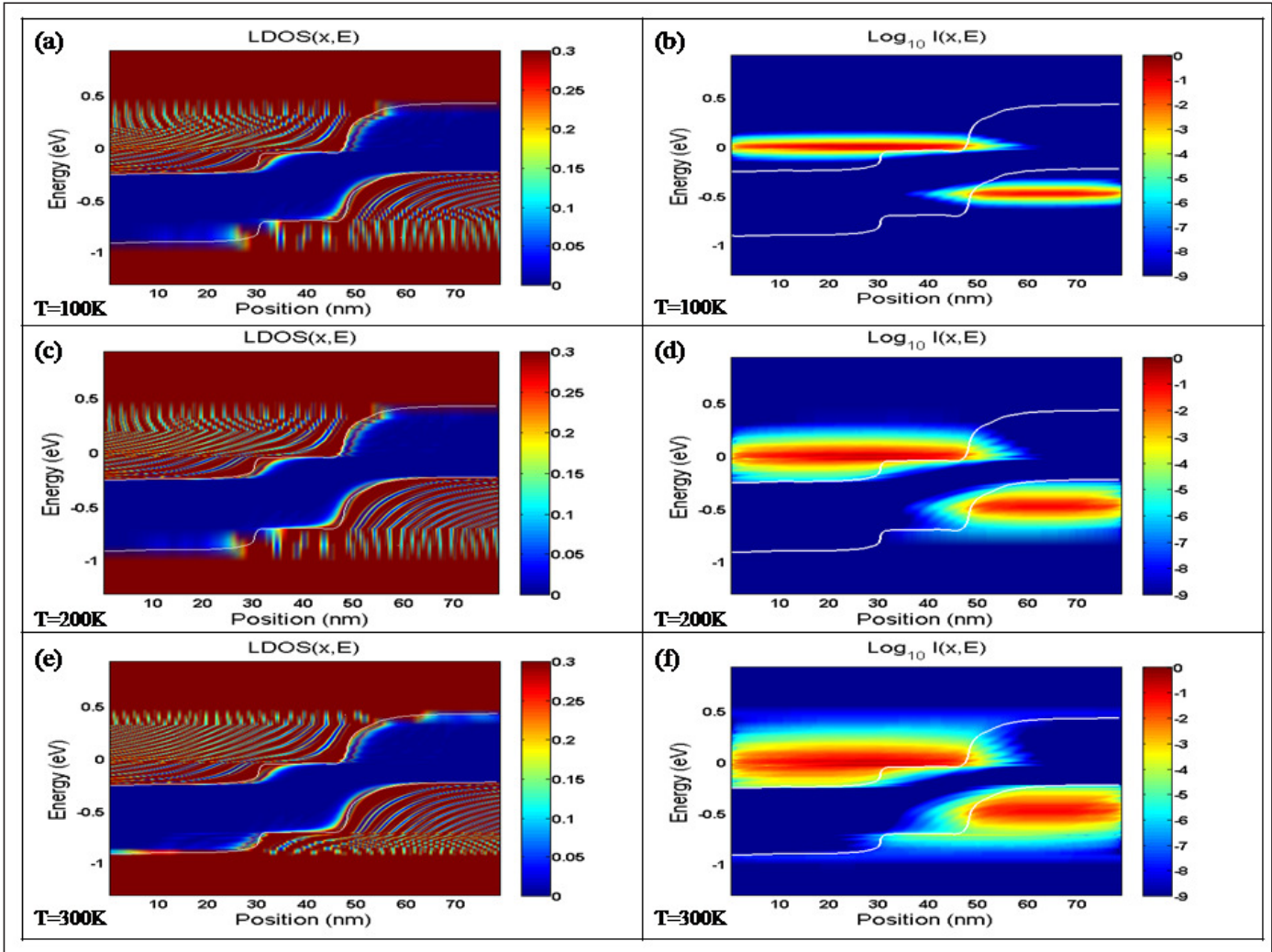
Fig. 2: *Plot of LDOS spectrum for (17,0) CNTFET for (a) T=100K, (c) T=200K, (e) T=300K and respective Energy position resolved current diagram is (b) T=100K (d) T=200K and (c) T=300K at V_{GS}=0.475V and V_{DS}=0.475V.*

and different oxide thickness variation on the radiative recombination rate (RRR) and electroluminescence (EL) intensity is studied and is presented in the Fig.3 below.

The RRR get enhanced with increase in the temperature in the Fig. 3(a). The involvement of a greater number of the density of states at higher temperature range made available large number of the electron-hole pairs inside the channel region, and recombination of increased number of carriers cause the RRR to increase with increase in temperature. Hence an enhancement in RRR is noticed with increase in temperature in Fig. 3(a) and it is observed that there is exponential increase in RRR with increase in temperature (inset of Fig. 3(a)). Respective EL intensity profile is shown in the Fig. 3(b). The EL intensity grows stronger with strengthening of temperature and exponential increase in EL intensity is noticed with temperature enhancement (inset of Fig. 3(b)).

It is found out that RRR get enhanced with decrease in the thickness of dielectric material used in Fig. 3(c). This is due to increased carrier's injection rate (inside the channel region) which cause more electron-hole pairs to accumulate inside the channel and hence increased number of carriers recombination cause RRR to enhance with decrease of the oxide thickness. It is observed that there is exponential fall in RRR with thickness enhancement of oxide layer used (inset Fig. 3(c)). It is noticed that there is exponential fall in the EL intensity with increasing the oxide layer thickness (inset Fig.3 (d)). Since the gate distance increased with increasing the oxide thickness which results in the degradation of gate control on channel and hence carrier's injection rate is affected, hence decrease in EL intensity is noticed with increased thickness of the oxide layer. Effect of the temperature variation on drain current of the simulated device structure is shown in the Fig. 4 below.
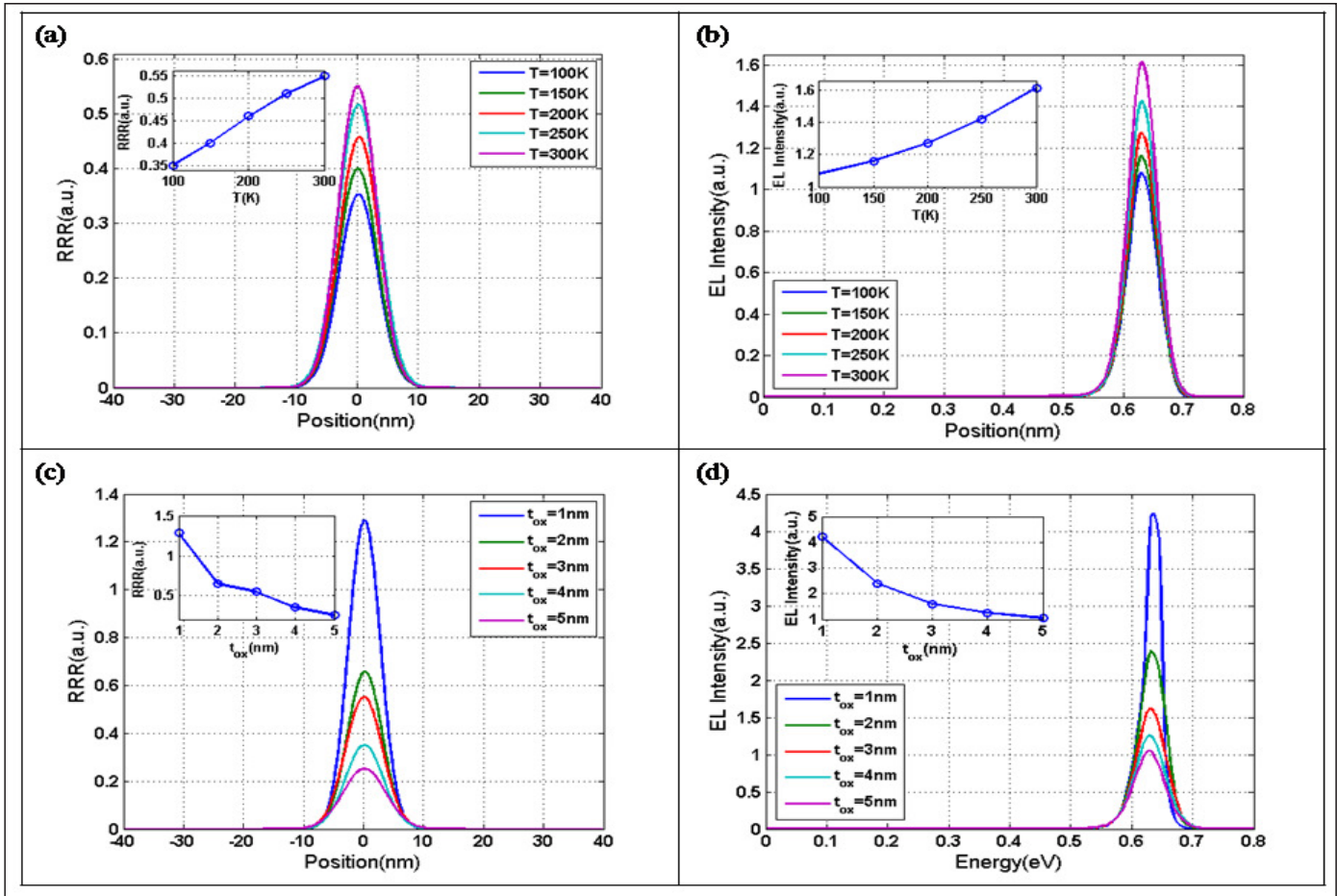
Fig. 3: *Plot of (a) Radiative recombination rate versus position (inset RRR versus T), (b) Electroluminescence intesity versus energy (inset EL Intensity versus T) for the different value of B, (c) Radiative recombination rate versus position (inset RRR versus t_{ox}) and (d) Electroluminescence intesity vs energy (inset EL Intensity versus t_{ox}) for (17,0) CNT at V_{GS}=0.475V, V_{DS}=0.475V.*
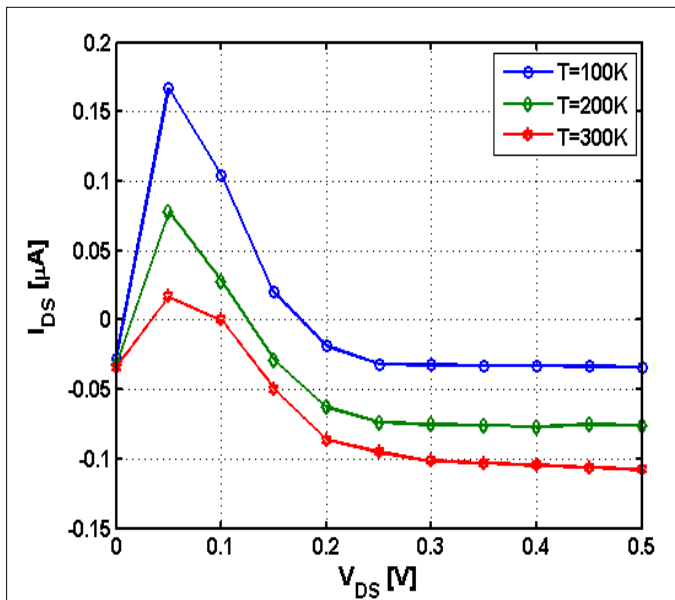

Fig. 4: *Plot of output-characteristics for (17,0) CNTFET at V_{GS}=0.475V for different temperature range.*

It is noticed that there is decrease in the drain current with increase in the temperature. This is because of increased number of carrier recombination inside the channel with increase in temperature. Due to increased participation of more number of densities of states more electron hole pairs get injected in the channel and hence increased recombination of more electron-hole pair's results in decrease of drain current at higher temperature.

4. Conclusion

We have studied the light emission properties of MOSFET-like coaxial gated CNTFET structure. The NEGF method is used to simulate the device characteristics of (17,0) CNT. It was found out that temperature has vital significance in functioning of the device and thickness of oxide layer used is equally important as well. Improvement in RRR and EL intensity is noticed at higher temperature region whereas downfall in RRR and EL intensity is found with reduction of oxide layer thickness. Due to increased recombination of carriers large number of carriers gets

annihilated and hence downfall in drain current is found at higher temperature.

References

1. P. Avouris, M. Freitag, V. Perebeinos, Nat. Photonics 2 (2008) 341.

2. S. Wang, Q. Zeng, L. Yang, Z. Zhang, Z. Wang, T. Pei, L. Ding, X. Liang, M. Gao, Y. Li, L. M. Peng, Nano lett. 11 (2010) 23.

3. A. Martinez, K. Fuse, B. Xu, S. Yamashita, Optics Express 18 (2010) 23054.

4. T. Hertel, Nat. Photonics 4 (2010) 77.

5. J. Hone, M. Whitney, C. Piskoti, A. Zettl, Phys. Rev. B 59 (1999) R2514.

6. P. Rai, N. Hartmann, J. Berthelot, J. Arocas, G.C. Francs, A. Hartschuh, A. Bouhelierv, Phys. Rev. let. 111 (2013) 026804.

7. J. Berthelot, G. Bachelier, M. Song, P. Rai, G. C. Francs, A. Dereux, A. Bouhelier, Optics Express 20 (2012) 10498.

8. L.M. Peng, Z. Zhang, S. Wang, X. Liang, AIP Advances 2 (2012) 15547.

9. S. K. Sinha, S. Chaudhury, J. of Semicond. 35 (2014) 114002.

10. J. A. Misewich, R. Martel, P. Avouris, J. C. Tsang, S. Heinze, J. Tersoff, J. of Science 300 (2003) 783.

11. M. R. Aziziyan, V. Ahmadi, N. Moghadam, Appl. Phys. Lett. 100 (2012) 05111.

12. J. Svensson, E.E.B. Campbell, J. of Appl. Phys. 110 (2011) 16.

13. S. O. Koswatta, M. Lundstrom, D. E. Nikonov, Nano letters 7 (2007) 1160.

14. J. Guo, M. Lundstrom, S. Datta, Appl. Phys. Lett. 80 (2002) 3192.

15. M. Freitag, J. Chen, J. Tersoff, J. C. Tsang, Q. Fu, J. Liu, P. Avouris, Phys. Rev. Lett. 93 (2004) 076803.

16. D. L. McGuire, D. L. Pulfrey, Nanotechn. 17 (2006) 5805.

17. A. Javey, J. Guo, D. B. Farmer, Q. Wang, D. Wang, R. G. Gordon, M. Lundstrom, H. Dai, Nano Letters 4 (2004) 447.

18. P. A.G. Sankar, K. Udhayakumar, J. of Semicond. 35 (2014) 075001.

19. J. Svensson, A. A. Sourab, Y. Tarakanov, D. S. Lee, S. J. Park, S. J. Baek, Y. W. Park, E. E.B. Campbell, Nanotechn. 20 (2009) 175204.

20. T. Mueller, M. Kinoshita, M. Steiner, V. Perebeinos, A. A. Bol, D. B. Farmer, P. Avouris, Nat. Nanotechn. 5 (2010) 27.

21. S. G. Shirazi, S. Mirzakuchaki, Appl. Phys. Lett. 99 (2011) 263104.

22. J. Chen, V. Perebeinos, M. Freitag, J. Tsang, Q. Fu, J. Liu, P. Avouris, Science 310 (2005) 1171.

23. J. Guo, S. Datta, M. Lundstrom, M. P. Anantram, Int. J. Multiscale Comput. Eng. 2 (2004) 257.

24. R. Venugopal, Z. Ren, S. Datta, M. S. Lundstrom, J. of Appl. Phys. 92 (2002) 3730.

25. M. P. Anantram, M. Lundstrom, D. E. Nikonov, Proceedings of the IEEE 96 (2008) 1511.

26. S. Datta, Superlattices and microstructures 28 (2000) 253.

27. S. O. Koswatta, M. Lundstrom, D. E. Nikonov, Nano Lett. 7 (2007) 1160.

28. I. Hassaninia, M.H. Sheikhi, Z. Kordrostami, Solid-State Electron. 52 (2008) 980.

29. J. Guo, M. A. Alam, Appl. Phy. Lett. 86 (2005) 023105.

30. S. M. Sze, K. K. Ng. Physics of semiconductor devices. John wiley & sons, 2006.

31. S. G. Shirazi, G. Karimi, S. Mirzakuchaki, ECS J. of Solid-State Science Techn.5 (2016) M44.

32. S.A. Imam, N. Kalam, S. Abdhulla, Nanoscience and Nanotechn. 4 (2014) 52.

33. S. K. Sinha, S. Chaudhury, IEEE Trans.on Nanotechn. 12 (2013) 958.

Dr. Tapender Singh *received B.Sc. degree in Science from Himachal Pradesh University, Shimla, India, in 2012. M.Sc. degree in condensed matter Physics from Central University of Himachal Pradesh, Dharamshala, India, in 2014. He has completed his Ph.D. degree from Central University of Himachal Pradesh, Dharamshala, India, in July 2020 and his research interests includes nano-scale device simulations.*

Dr. Padmnabh Rai *is a Reader (F) in School of Physical Sciences at UM-DAE Centre for Excellence in Basic Sciences, Mmbai-400098 since March 2018. He received his M. Tech. and Ph. D. degree in Condensed Matter Physics from IIT Delhi in 2004 and IIT Bombay in 2009, respectively. Dr. Rai has served as an Assistant Professor (UGC) in Department Physics and Astronomical Sciences at Central University of Himachal Pradesh (HP) during July 2014 to March 2018. He has worked as postdoctoral fellow at National University Singapore, Singapore (December 2013 – May 2014), University of Bourgogne, France (October 2010 – September 2013) and Sunkyunkwan University, South Korea (October 2009 – August 2010). He was Research and Development manager in Diamond Division of Nozomi Technotron Pvt. Ltd., Singapore (January 2009 – August 2009). Dr. Rai is experienced in synthesizing carbon based materials (single crystal diamond, carbon nanotube and graphene). Carbon-based materials are being explored for photonics and plasmonics applications. Dr. Rai is also involved in teaching physics courses at graduate and undergraduate level. He has consulted industries to develop laboratory for growing single crystal diamond for gem and scientific applications. He has more than 35 research publications in international peer reviewed journals and books and 02 patents.*

SOCIETY FOR MATERIALS CHEMISTRY (SMC)
(Reg. No. – Maharashtra, Mumbai/1229/2008/GBBSD)
c/o Chemistry Division
Bhabha Atomic Research Centre, Mumbai 400 085

APPLICATION FOR MEMBERSHIP

Please enroll me as a Life member of the *Society for Materials Chemistry (SMC)*. My particulars are as follows:

Name : _____

Educational Qualifications : _____

Field of Specialization : _____

_____

Official Address : _____

_____

Telephone No. (Off) : _____

Residential Address : _____

_____

Telephone No. (Res.) : _____

Address for Correspondence : Home/Office (Please tick one of the options)

E-mail Address : _____

Subscription Details
Mode of Payment : Cheque/DD/Cash
(Cheque/DD should be drawn in favor of *"Society for Materials Chemistry"* for Rs. 1000/- payable at Mumbai. For out-station non-*multi-city* cheques, please include Rs 50/- as additional charge for bank clearance.

Number :
Dated :
Drawn on Bank & Branch :
Amount :
Place:
Date: Signature

Registration Number: _____   (To be allotted by SMC office)

In this issue